A MULTISCALE ANALYSIS OF HEAT TRANSFER IN POROUS MEDIA

A Dissertation
Presented to
The Academic Faculty

By

Hamid Reza Ghazizadeh Karani

In Partial Fulfillment
of the Requirements for the Degree
Doctor of Philosophy in the
School of Earth & Atmospheric Sciences

Georgia Institute of Technology

December 2017

A MULTISCALE ANALYSIS OF HEAT TRANSFER IN POROUS MEDIA

Approved by:

Dr. Christian Huber, Advisor
Department of Earth, Environmental and Planetary Sciences
Brown University

Dr. Joe Dufek
School of Earth & Atmospheric Sciences
Georgia Institute of Technology

Dr. Sven Simon
School of Earth & Atmospheric Sciences
Georgia Institute of Technology

Dr. Ken Ferrier
School of Earth & Atmospheric Sciences
Georgia Institute of Technology

Dr. Richard L. Magin
Department of Bioengineering
University of Illinois at Chicago

Date Approved: October 27, 2017

When yesterday is vanished in the past,

And morrow lingers in the future vast,

To neither give a thought but prize the hour,

For that is all you have and time flies fast...

Omar Khayyam (1048-1131)

To my family and the loving memory of my father

TABLE OF CONTENTS

LIST OF TABLES

LIST OF FIGURES

SUMMARY

The modeling of thermal convection in porous media is a challenging task due to the inherent structural and thermophysical heterogeneities that permeate over several scales. In the present thesis, I address several issues relevant to buoyancy-driven thermal convection in porous media. The central question we address is how to develop a macroscopic model of heat transfer in porous media that incorporates the pore-scale physics in a consistent manner. Our approach is based on establishing a multi-scale framework built on knowledge accrued by theoretical, numerical and experimental methods.

In Chapter 2, we develop a pore-scale computational tool based on a lattice Boltzmann (LB) model. This computational tool enables us to tackle thermal convection from a pore-scale perspective and to provide benchmarks for the development of an appropriate continuum-scale models. In Chapter 3, we use our LB model and conduct high-resolution direct numerical simulation at the pore scale. The objective is to evaluate the underlying assumptions of upscaled thermal models and to assess the role of thermophysical heterogeneties on heat transfer. We benefit from the insights gained from our pore-scale results and propose a new upscaled energy model for thermal convection in Chapter 4. The proposed model is based on a fractional-order advective term, which models the influence of thermal heterogeneities in a flexible and consistent way. In Chapter 5, we used a combination of theoretical and experimental approaches to calculate a new metric, basin stability, for quantifying the respective relative stability of coexisting convection modes in porous media. We show that transition between convective modes predicted by the basin stability analysis agrees well with the experiments from our IR thermography visualization setup.

CHAPTER 1

INTRODUCTION AND BACKGROUND

Thermal convection in porous media is central to a large variety of geophysical and industrial systems [1]. Heat from deep within the Earth drives underground thermal convection that is crucial for the extraction of geothermal energy [2, 3], while convective currents in both the continental and the oceanic lithosphere play a major role in the heat budget of the Earth. The nature of large scale free convective flows of ground water and carbon dioxide within the Earth's crust is important for understanding the release of heat and carbon dioxide into the hydrosphere and atmosphere [3]. Thus, the understanding of such convective flow processes has become closely tied to better constraining the response of soils and groundwater systems to climate change. From a mathematical viewpoint, convection is a complex nonlinear process that provides a rich set of dynamical regimes for the study of chaotic and turbulent dynamics, bifurcations, and emergent patterns [4], which strongly influence the associated rate of heat transfer in and out of these porous media [5].

In recent years, there has been particular interest in better understanding the effect of thermal convection on the long-term development and sustainability of geothermal systems [3], which has been widely proposed as one of the most promising green and renewable energy resources [6]. Geothermal systems utilize a working fluid to transport and harvest the thermal energy from the temperature difference between the Earth's hot subsurface layers and the cooler surface, caused by Earth's geotherm (temperature profile in the Earth). While conventional geothermal systems utilize water/brine as the working fluid (hence called hydrothermal systems), several studies in recent years proposed the idea of using supercritical CO_2 as a promising alternative [7, 8]. Compared with water-based geothermal systems, CO_2 offers several advantages. First, the use of CO_2 as the working fluid in geothermal reservoirs provides an efficient way for CO_2 geological storage, one of the important el-

ements of greenhouse gas reduction strategies [7, 8, 9, 10]. And second, it addresses the limitations of water availibility for long-term operation of water-based geothermal systems [10, 11]. In particular, several studies on CO_2-plume geothermal systems have indicated that, the large thermal expansivity and substantial change in the density of supercritical CO_2 under typical geothermal reservoir and surface conditions, result in buoyancy-driven convective currents for the natural extraction of geothermal energy [8, 12].

While current mathematical modeling of geothermal systems is based on the concepts of fluid flow and heat transfer within porous media [2, 6], there are several experimental studies showing the failure of the available models in providing accurate thermal predictions for the strength of the convective currents [2, 13, 14]. The reported discrepencies between the predictions of experimental data and thermal models are mainly for fluid-solid matrix combinations with a considerable difference in thermophysical properties [2, 13]. In the context of geothermal systems, this latter point becomes important if we take into account the difference in thermal conductivities of supercritical CO_2 ($k_{scCO_2} \approx 0.048$ W/m.K) and water ($k_w \approx 0.70$ W/m.K) with those from typical sedimentary rocks ($k_{rock} \approx$ 2.1 W/m.K), resulting in solid-to-fluid thermal conductivity ratios of $k_{scCO_2}/k_{rock} \approx 43$ and $k_w/k_{rock} \approx 3$ in typical reservoir conditions. Therefore, a comprehensive understanding of the convective heat transfer characteristics of supercritical CO_2 or water in the complex subsurface structures is crucial for building a reliable and accurate numerical model of geothermal systems, with the ultimate aim of assessing the potential convective heat flux available at the surface and predicting the structure of subsurface temperature and flow profiles for geothermal design objectives [6].

In this thesis, we study thermal convection in a porous medium subjected to an adverse temperature gradient schematically shown in Fig. 1.1. This problem, which is the analog of Rayleigh-Bénard (RB) convection for a fluid-saturated porous layer, has been first investigated by Horton and Rogers [15] and Lapwood [16], hereafter called Horton-Rogers-Lapwood (HRL) convection. Due to the natural occurence of an adverse temperature gra-
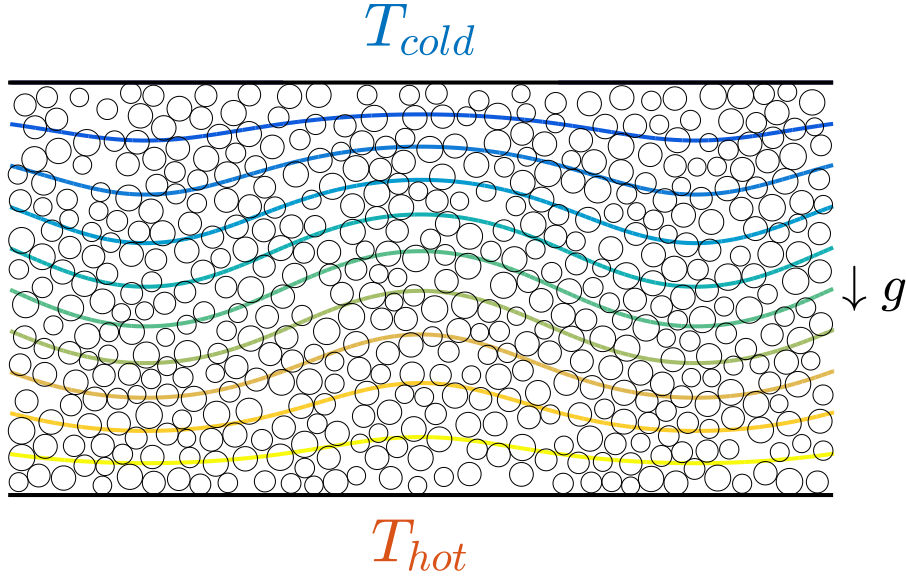
Figure 1.1: Schematic of the Horton-Rogers-Lapwood problem, showing a solid matrix (circular disks) saturated with fluid, which is experiencing a thermal convection due to the vertical temperature gradient (shown in colored lines).

dient in the geotherm, HRL has been studied extensively in the context of geophysical applications [2, 3, 1], as a tractable benchmark problem for understanding the underlying physics that drive the thermal convective currents in subsurface media. The temperature difference (ΔT) across the fluid-saturated porous layer gives rise to density differences, as regions of fluid near the bottom (top) boundary are warmed (cooled) and hence expand (contract). The density differences in turn result in a net buoyancy force, which acts to re-organize the lighter fluid at the top boundary (and heavier fluid at the bottom) to minimize potential energy. For small ΔT, the fluid remains motionless; heat is transferred across the fluid through conduction, with a linear temperature profile across the fluid layer. Therefore, the strength and dynamics of HRL convection strongly depends on the interplay between the driving buoyancy force and the inhibiting dissipative effects of diffusion and viscosity in the fluid-satured porous layer. The competition of these governing forces is character-ized by a dimensionless parameter called Rayleigh number Ra. Beyond a certain critical Ra value, the previously stationary layer becomes unstable and convection initiates.

In Section 1.1, we introduce the inherent multi-scale nature of thermal convection in porous media. We distinguish pore-scale *vs.* continuum-scale modeling approaches, with an emphasis on closure relationships required by upscaling. In Section 1.2, we give a brief overview of the mathematical components of thermal convection in porous media. In Section 1.3, we outline the motivation and research objectives of the present thesis and in Section 1.4, we lay out the structure of the thesis.

1.1 Multi-scale nature of HRL convection

The modeling of HRL convection in natural systems is a challenging task due to the inherent structural heterogeneities that permeate over several spatial and temporal scales, schematically shown in Fig. 1.2. Moreover, the complex interfaces between solid and fluid phases (of different thermophysical properties) render a porous medium into a thermophysically heterogeneous system [17, 18, 19]. From a computational perspective, it is extremely challenging to model these multi-scale systems in an adequate way accounting for the spatially varying and scale-dependent character of thermal processes.

To address these issues, one can express the essential physical behavior that is present at the fine scale in an *averaged sense* at the macroscopic scale without the need to model all details at the pore-scale [20, 21]. In this so-called *upscaling* approach, one recovers the upscaled governing equations through a mathematical homogenization procedure, such as volume-averaging [20, 22] (schematically shown in Fig. 1.3). The resulting upscaled equations solve for average values $< . >$ of flow and heat transfer in a new continuum ($< . >$ refers to spatial average over a representative elementry volume (REV) [22]). The convenience of dealing with the averaged physical quantities in an upscaled equation comes at the cost of the emergence of unknown closure terms, which require constitutive models. Since the interfacial interactions at the pore scale are responsible for the observable macroscopic thermal behaviors, it is clear that the successful modeling of an upscaled heat transfer model lies on the systematic transfer of information over the hierarchy of temporal

and spatial scales and incorporating these interfacial interactions in the closure modeling of the unknown quantities. Without a good insight into such interfacial coupling, sound macroscopic energy models cannot be developed.

1.2 Mathematical formulation

In what follows, we introduce the continuum-scale governing equations of the flow and temperature fields for HRL convection and we then provide the details of the mathematical formulation of the pore-scale analysis of HRL problem.

1.2.1 Continuum-scale Approach

Fluid flow model

Throughout the present thesis, we assume that the continuum-scale flow field in porous media follows Darcy's law for an incompressible fluid, which relates the driving pressure and buoyancy forces to the viscous drag imparted by the medium on the pore scale [1]:

$$\nabla \cdot \mathbf{q} = \mathbf{0}, \tag{1.1}$$

$$\frac{\mu}{K}\mathbf{q} = -\nabla P + \rho\mathbf{g}, \tag{1.2}$$

where ρ is the fluid density, K is the permeability of the porous medium, P is the pressure, μ is the dynamic viscosity of the fluid and $\mathbf{q}$ is the Darcy velocity (average velocity over both the solid matrix and the pore space in a representative volume). $\rho\mathbf{g}$ is the body force (buoyancy term) driving the fluid motion in HRL convection. Throughout this thesis, we assume that the fluid density satisfy the Boussinesq approximation [1], i.e. density is assumed to be constant except in the buoyancy term, where it becomes:
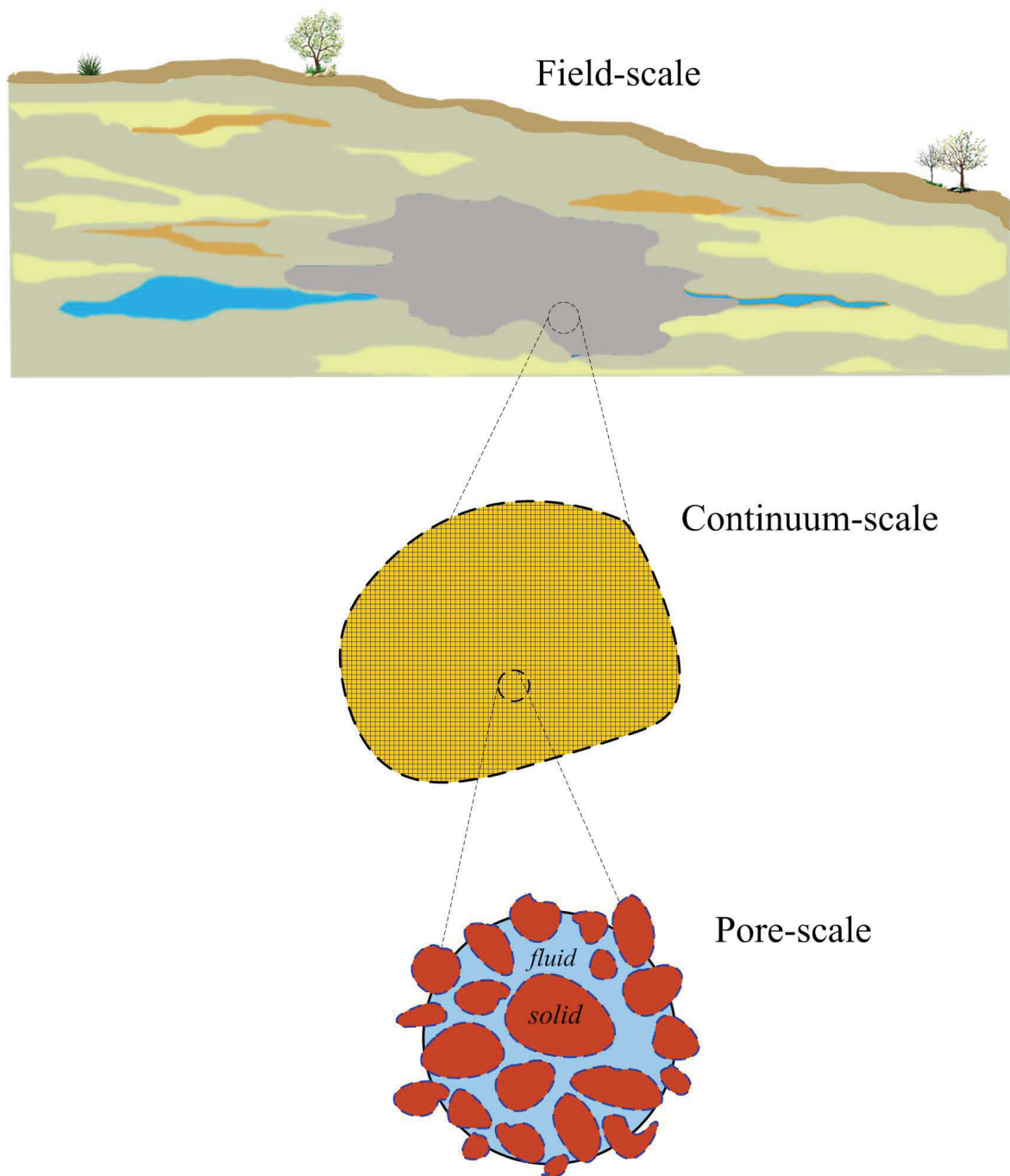
Figure 1.2: Illustration of the hierarchy of scales for natural porous media
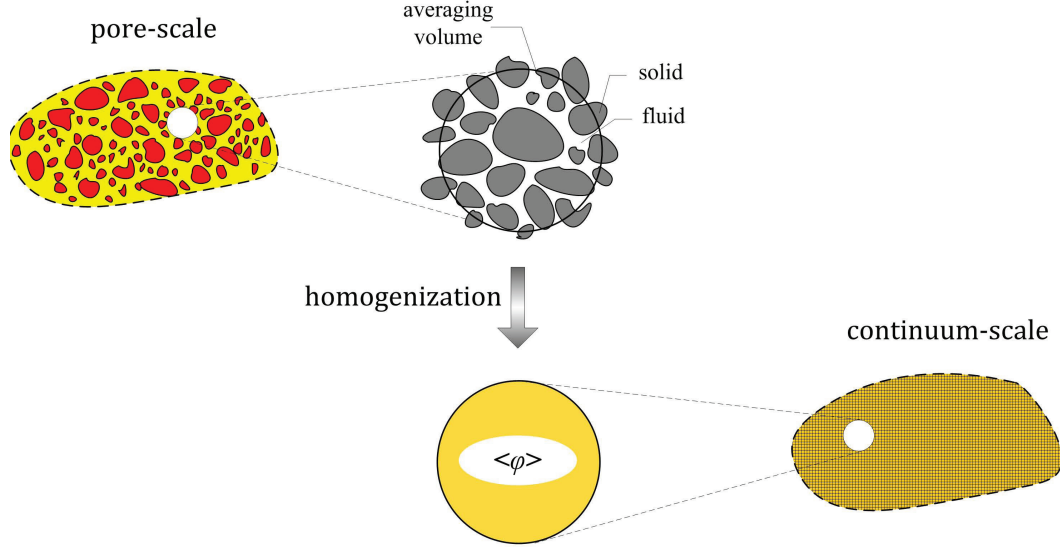
Figure 1.3: Continuum-approach *vs.* pore-scale approach for modeling transport phenomena in porous media. The homogenization or spatial averaging is performed over a representative elementary volume (REV) chosen from the pore-scale domain. The resulting spatially averaged values of a physical quantity $< \phi >$ represents the corresponding values in a new continuum-scale domain.

$$\rho = \rho_0(1 - \beta(T - T_{ref})), \tag{1.3}$$

where ρ_0 is the density at the reference temperature T_{ref}, and β is the thermal expansion coefficient of the fluid.

By using Darcy's law, we assume that the medium is fully saturated by the fluid, and inertia is assumed to be negligible compared to viscous drag. While there are multiple variations of Darcy's law [1], the results of the pore-scale calculations in Chapter 3 confirm the validity of our assumption for the cases investigated in the thesis.

Energy models

The upscaled models of heat transfer in porous media offer a convenient way for calculating the average tempreature field in the domain. However, the drawback is in the emergence of unknown terms in the course of homogenization, which again requires closure. Since heat transfer occurs in at least two phases in a porous medium, we can adopt two different scenarios in applying the homogenization procedure over an averaging volume. First, we can assume that the phase-averaged temperature of fluid and solid phases are locally equal in the corresponding averaging volume. In other words, both phases are experiencing local thermal equilibrium (LTE) condition (schematically shown in Fig. 1.4). Therefore, the upscaled energy formulation leads to a single equation holding for both phases and it takes the following form:

$$(\rho c)_m \frac{\partial T}{\partial t} + (\rho c)_f \mathbf{q} \cdot \nabla T + \nabla \cdot ((\rho c)_f T' q') = k_m \nabla^2 T, \tag{1.4}$$

where T is the local temperature averaged over both phases, c is the specific heat and ρ is the density. The subscripts m and f refer to the properties of the solid/fluid mixture and the fluid, respectively. T' and q' refer to the fluctuations in the temperature and velocity fields, compared to the average values [23].

There are situations where LTE assumptions do not hold, such as in a medium where the fluid and solid thermophysical properties are very different and where fluid experiences high local velocities [24, 19, 25]. Thermal non-equilibrium between solid and fluid phases stems from a delay in the interaction between the fluid and solid phases [25]. Under local thermal non-equilibrium (LTNE) conditions, two separate equations for the average temperatures of each phase are required (schematically shown in Fig. 1.5). The simplest equations that are now used routinely under LTNE assumption are [25, 1]:
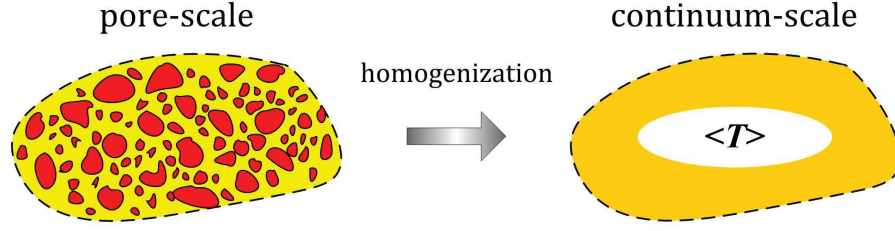
Figure 1.4: Schematic of the continuum energy model under LTE assumption.

$$\varphi(\rho c)_f \frac{\partial T_f}{\partial t} + (\rho c)_f \mathbf{q} \cdot \nabla T_f + \nabla \cdot ((\rho c)_f T' q') = \varphi k_f \nabla^2 T_f + h(T_s - T_f), \qquad (1.5)$$

$$(1 - \varphi)(\rho c)_s \frac{\partial T_s}{\partial t} = (1 - \varphi)k_s \nabla^2 T_s - h(T_s - T_f). \qquad (1.6)$$

Since solid and fluid phases are exchanging heat through interfaces, the two averaged energy equations are coupled through the inter-phase heat transfer coefficient *h*, which is responsible for capturing the non-equilibrium heat transfer between the different phases. Here, φ is the porosity of the medium and subscripts *s* and *f* refer to properties of the solid and fluid phase properties, respectively.

In Eqs. 1.4 and 1.5, the $\nabla \cdot ((\rho c)_f T' q')$ is referred to as the thermal dispersion term, and it accounts for the contribution of the fluctuations in the temperature and velocity fields on the total thermal convection [23]. The thermal dispersion term is a byproduct of upscaling and, as such, it is based on average-scale temperature and velocity fields, i.e. T and $\mathbf{q}$ [23].

continuum-scale

pore-scale

homogenization

$<T_s>$

$<T_f>$
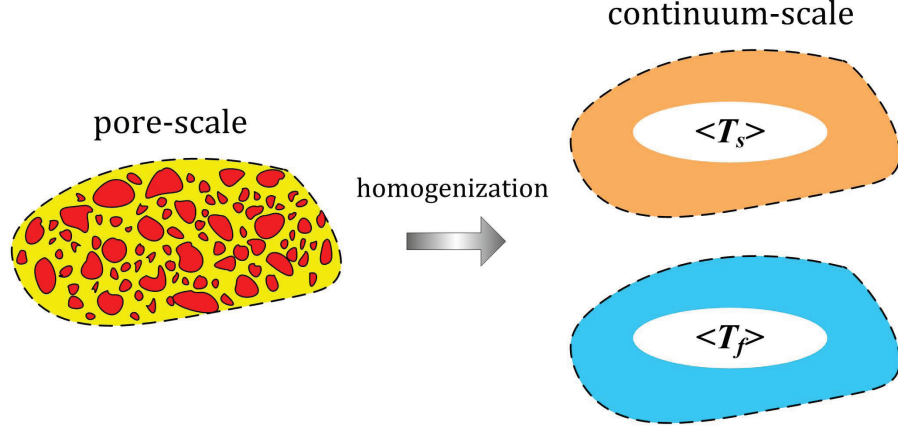
Figure 1.5: Schematic of the continuum energy model under LTNE assumption.

1.2.2   Pore-scale Approach

In pore-scale simulations, we solve the momentum and energy equations in both solid and fluid phases comprising the porous domain (refer to the schematic pore-scale domains in Fig. 1.3). While being more computationally intensive compared to the upscaled models, the pore-scale analysis does not require the use of closure models. Therefore, the simulation results of the pore-scale analysis can serve as an accurate solution for verifying and evaluating the performance of any continuum-scale models.

For the fluid phase, we numerically solve the Navier-Stokes and the energy equations for the flow and temperature fields, respectively:

$$\nabla \cdot \boldsymbol{u} = 0, \tag{1.7}$$

$$\frac{\partial \mathbf{u}}{\partial t} + (\mathbf{u} \cdot \nabla)\mathbf{u} = -\frac{1}{\rho}\nabla P + \nu \nabla^2 \mathbf{u} + \mathbf{g}\beta(T - T_{ref}), \tag{1.8}$$

10

$$(\rho c)_f \frac{\partial T}{\partial t} + \nabla \cdot ((\rho c)_f \mathbf{u} T) = \nabla \cdot (k_f \nabla T), \tag{1.9}$$

where $\mathbf{u}$ is the pore-scale velocity field, P is the pressure, T is the temperature, ν is the kinematic viscosity of the fluid, β is the thermal expansion coefficient, $\mathbf{g}$ is the gravitational acceleration, k refers to thermal conductivity, c is the specific heat and ρ the density of the fluid phase (subscript f). For the solid phase, the energy equation reduces to:

$$(\rho c)_s \frac{\partial T}{\partial t} = \nabla \cdot (k_s \nabla T), \tag{1.10}$$

where the subscript s refers to the properties of the solid phase. Across a fluid-solid interface I, the no-slip boundary condition holds and the continuity of temperature and normal heat flux yield [24]:

$$\mathbf{u} = 0, \quad \text{no-slip at all solid walls}, \tag{1.11}$$

$$T^{I,+} = T^{I,-},$$
$$\mathbf{n} \cdot (k\nabla T + \rho c \mathbf{u} T)^{I,+} = \mathbf{n} \cdot (k\nabla T + \rho c \mathbf{u} T)^{I,-}, \tag{1.12}$$

where $\mathbf{n}$ is normal to the interface and $+$ and $-$ denote the different sides of the interface.

In order to compare the pore-scale results with the continuum-scale predictions, we compute the Darcy-Rayleigh number Ra^* and average Nusselt number Nu^* which are defined as:

$$Ra^* = \frac{g\beta(T_H - T_C)KH}{\alpha_m \nu_f} = Ra_f \cdot Da \cdot \frac{k_f}{k_m},$$

$$Ra_f = \frac{g\beta(T_H - T_C)H^3}{\alpha_f \nu_f}, \quad Da = \frac{K}{H^2},$$

$$Nu^* = 1 + \frac{1}{A}\frac{\int_A u_y \cdot T \, dA}{\alpha_m \Delta T/H}, \tag{1.13}$$

$$\alpha_m = \frac{k_m}{(\rho c)_f},$$

where Ra_f is the conventional Rayleigh number based on the fluid properties. In Ra^*, K is the permeability of the porous medium, α_m is the thermal diffusivity based on stagnant thermal conductivity of the solid matrix and hosted fluid k_m, and H is the characteristic length of the porous domain. $\Delta T = T_H - T_C$ is the temperature difference between the hot and cold horizontal surfaces and *Da* is the Darcy number of the porous medium. In Nu^*, A is the horizontal cross sectional area of the domain and u_y is the vertical component of the velocity field.

1.3 Motivation and research objectives

The conventional approach for studying HRL convection is based on using the upscaled (volume-averaged) formulation of fluid flow and energy equations. While the HRL convection has been studied extensively in the literature [1], there are several theoretical and experimental studies showing that the available upscaled models are not able to provide a consistent prediction for the thermal behavior of HRL convection [26, 2, 27, 13, 28, 14, 29]. Also, understanding the role of the solid matrix on the dynamics of thermal convection and the associated enhancement of the heat transport (represented by the dimensionless Nusselt number *Nu*) still requires reassessing the available upscaled models [28, 14].

The reported departures between the theoretical predictions and experimental observations mainly involve three different features of HRL convection. Figure 1.6 schematically
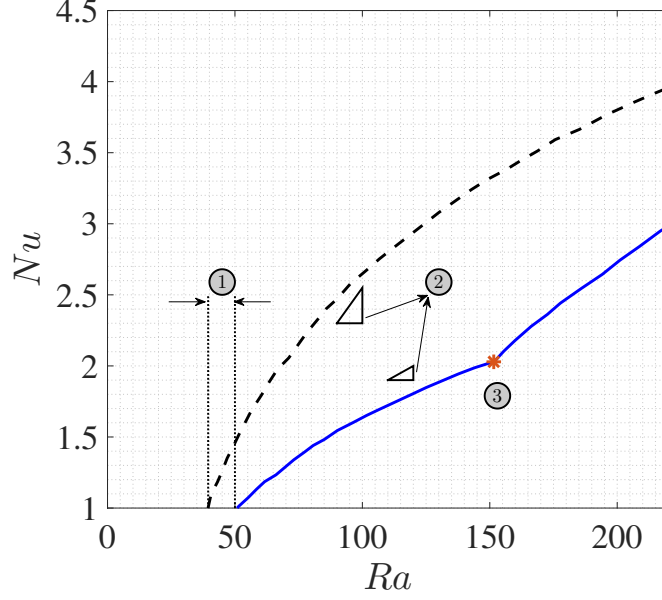
Figure 1.6: Schematic showing three main features of the inconsistency between upscaled models (dashed line) and experimental data (solid line). The first inconsistency is associated with the shift in the onset of convection. The second inconsistency is related to the change in the $Nu - Ra$ scaling (slope of the curve). The third inconsistency is related to the presence of a kink in the $Nu - Ra$ curve at some values of the Rayleigh number.

depicts these three aspects in a typical heat transfer curve of HRL convection. The figure shows the variation of the average amount of heat transfer, represented by the dimensionless Nusselt number Nu, against the thermal loading across the porous layer, represented by the dimensionless Rayleigh number Ra. $Nu = 1$ represents conditions where the heat is transferred only by conduction, which occur at low temperature differences between the bottom hot and top cold surface of the porous layer. Beyond the critical value Ra_{cr}, convection initiates, and accordingly the Nusselt number becomes greater than 1.

The features in Fig. 1.6 are summarized as below:

1. Shift in the onset of convection, i.e. the critical value of the Rayleigh number at which convection initiates. Several studies have reported that the critical Rayleigh number observed experimentally does not agree [13, 14] with the value predicted by linear stability analysis of the available continuum-scale models.

2. Change in the $Nu - Ra$ scaling or the slope of the heat transfer curve. The experimen-

13

tal data in [2, 13] show that for certain combinations of pore fluid and solid matrix properties, the measured Nusselt number can be lower than the value predicted by the continuum scale models.

3. At some values of Rayleigh number, kinks in the slope of the $Nu - Ra$ have been experimentally observed [26, 27, 13]. While several explanations have been provided to explain this feature [30, 31, 29], it still lacks a proper understanding.

To date, there exists no comprehensive explanation for the three features summarized in Fig. 1.6. The research presented in this thesis has been motivated by a desire to provide a clear picture of the thermal behavior of HRL convection, with an ultimate goal of providing new explanations for the reported inconsistencies discussed above. In the present thesis, we postulate that the failure of the available upscaled formulations in providing consistent predictions of HRL convection originates from the lack of a clear understanding of the underlying physical interactions at the pore-scale and how they manifest at the macroscopic scale.

1.4   Thesis layout

In the present thesis, we devise a multi-scale framework for studying HRL convection, which benefits from the insight gained from a pore-scale analysis in developing a consistent upscaled formulation for thermal convection in porous media. The structure of the thesis is:

- In Chapter 2, we develop a pore-scale computational tool based on a lattice Boltzmann (LB) model. This computational tool enables us to tackle HRL convection from a pore-scale perspective. The approach is based on reformulating the lattice Boltzmann equation for solving the conservative form of the energy equation. This leads to the appearance of a source term, which introduces the jump conditions at the interface (Eqs. 1.12) between two phases or components with different thermal

14

properties. The simple implementation of the source term approach avoids any correction of distribution functions neighboring the interface in the LB procedure and provides an algorithm that is independent from the topology of the interface. Moreover, our approach is independent of the choice of lattice discretization and can be easily applied to different advection-diffusion LB solvers. We test the model against several benchmark problems including steady-state convection-diffusion within two fluid layers with parallel and normal interfaces with respect to the flow direction, unsteady conduction in a three-layer stratified domain, and steady conduction in a two-layer annulus. The LBM results are in excellent agreement with analytical solution. Error analysis shows that the proposed LB model is first-order accurate in space, but an extension to a second-order scheme is straightforward. The results confirm the reliability of our model in simulating complex coupled fluid and thermal dynamics in complex geometries.

- In Chapter 3, we perform a pore-scale analysis of HRL convection. The objective of this pore-scale analysis is to provide insights on the source of inconsistencies (1) and (2) in Fig. 1.6. We conduct high-resolution direct numerical simulation at the pore scale in a two-dimensional regular porous structure by means of our thermal lattice-Boltzmann model. We perform a combination of linear stability analysis of continuum-scale heat transfer models, and pore-scale and continuum-scale simulations to study the role of thermal conductivity contrasts among phases on HRL convection. The detailed temperature fields from the pore-scale analysis enable us to directly quantify the amount of thermal disequilibrium between solid and fluid phases in HRL convection. While previous studies relate inconsistencies (1) and (2) between experiments and theory shown in Fig. 1.6 to a possible lack of thermal equilibrium between the average solid and fluid temperatures [13], our pore-scale results invalidate this argument. We show instead that these inconsistencies result from a new thermal dispersion phenomena in HRL convection, which is caused by

the thermophysical heterogeneities in the porous domain. This thermal dispersion phenomena has not been identified before and can not be captured by the available thermal dispersion models. We argue for the need to revisit the closure modeling of the thermal dispersion term ($\nabla \cdot ((\rho c)_f T' q')$ in Eqs. 1.4-1.6) in the available upscaled models.

- In Chapter 4, we develop a new upscaled model for HRL convection which consistently models the observed features #(1) and #(2) in Fig. 1.6. We extend the classical upscaled models of heat transfer in porous media by including a fractional-order advective-dispersive term to account for the role of thermophysical heterogeneities in shifting the thermal instability point. The proposed fractional-order model overcomes limitations of the common closure approaches for the thermal dispersion term by replacing the diffusive assumption with a fractional-order model. Through a linear stability analysis and Galerkin procedure, we derive an analytical formula for the critical Rayleigh number as a function of the fractional model parameters. The resulting critical Rayleigh number reduces to the classical value in the absence of thermophysical heterogeneities when solid and fluid phases have similar thermal conductivities. Numerical simulations of the coupled flow equation with the fractional-order energy model near the primary bifurcation point confirm our analytical results. Moreover, data from pore-scale simulations are used to examine the potential of the proposed fractional-order model in predicting the amount of heat transfer across the porous enclosure. The linear stability and numerical results show that, unlike the classical upscaled models, the fractional-order model captures the shift in the onset of convection in porous media and provides correct scalings for the average heat transfer in a thermophysically heterogeneous medium.

- Chapter 5 attemps to provide a new insight into the nature of the kink in the available experimental data (feature #(3) in Fig. 1.6). While previous studies relate this

change in $Nu - Ra$ scaling to a thermal dispersion process [30, 31], we conduct experiments and show that the observed kink in the $Nu - Ra$ curve is due to a transitional behavior of stable convective patterns in HRL convection; a dynamical feature of HRL convection that has not been previously taken into account in the classical bifurcation analysis of HRL problem. Our experimental setup is based on an IR-thermography pattern visualization, which enables us to identify the transition point from the single- to double-cell pattern in a two-dimensional porous medium. We theoretically complement our experimental observations by introducing a new concept in the dynamical behavior of HRL convection, namely *basin stability*. This new metric enables us to assess the relative stability of different convective modes. We develop a basin stability diagram for HRL convection, which not only provides the domains of coexistence of different modes, but it also shows that the likelihood of finding convective patterns depends strongly on the Rayleigh number. The experimentally observed transition point from single- to double-cell mode agrees well with the stochastically preferred mode inferred from the basin stability diagram.

CHAPTER 2

LATTICE BOLTZMANN MODEL FOR CONJUGATE HEAT TRANSFER

In this chapter, we develop a pore-scale computational tool that enables us to tackle HRL convection from a pore-scale perspective. The inherent thermophysically heterogeneous nature of a porous medium requires a new computational model, which can handle the interfacial interactions between the solid and fluid phases correctly. For this purpose, we develop a new thermal lattice Boltzmann (LB) model for studying heat transfer in heterogeneous media. The material contained in this chapter has been published in *Physical Review E*, under the title 'Lattice Boltzmann formulation for conjugate heat transfer in heterogeneous media' [32].

2.1 Introduction

Heat transfer in multicomponent or multiphase systems has numerous applications in scientific and engineering problems [17, 33, 1]. Accurate microscale modeling in complex multicomponent or multiphase media is necessary to constrain heat transfer at the discrete scale and ultimately develop improved upscaling schemes [34]. In the past few years, the lattice Boltzmann method (LBM) has proven to be a promising numerical tool for studying diverse physical problems. The major advantage of LBM resides in its simple formulation and implementation of boundary conditions, which makes it ideally suited to study complex flows and multiphase or multicomponent systems [35, 36, 37]. These important numerical features encouraged researchers to apply LBM to modeling heat transfer processes. As we outlined in Section 1.2.2, when dealing with heat transfer in heterogeneous media, one needs to consider continuity conditions at the interface between two phases or components, which are often referred to as conjugate conditions. Applying conjugate boundary conditions is not trivial in heterogeneous systems with multiple interfaces. The

situation becomes more complicated when the interfaces change or evolve over time in response to chemical reactions, phase change, or the relative motion of a phase with respect to the other.

Studying conjugate heat transfer is rather new with LBM. An excellent review of the existing approaches for treating conjugate heat transfer using LBM is provided in [38]. Originally LBM studies were limited to steady-state conjugate heat transfer problems [39, 40]. Under steady conditions, only the thermal conductivity k plays a role in the steady-state solution for the temperature distribution. Since only the steady-state solutions were sought, the heat capacitance C (the product of the density ρ and heat capacity c) of the two materials is not relevant and one can, for simplicity, assume C to be identical in all components. Therefore, the ratio of thermal conductivities becomes equal to the ratio of thermal diffusivity $\alpha = k/\rho c$ and steady-state solutions can easily be retrieved from standard LBM advection-diffusion models [41]. It is, however, important to note that under transient conditions a general conjugate heat transfer solution involves two independent and possible heterogeneous scalar fields, the thermal conductivity and heat capacitance. For that reason, the validity of heat diffusion models that do not account for spatial variations of the heat capacitance are limited to steady-state solutions. This point will be explained in more detail in the next section.

To overcome this limitation, recent studies based on LBM implemented conjugate boundary conditions by correcting distribution functions crossing interfaces between two media with different thermal properties [42, 43, 44]. This approach works well for both steady and transient conditions. However, it is limited to simple interfaces. Very recently, [38] extended their previous work on boundary conditions for thermal LBM [45] to conjugate boundary conditions. Their approach is a general treatment of jump conditions at the interface, which works both for planar and curved interfaces under transient and steady conditions. They also showed that the approach is second-order accurate in space.

Common to all of the previous approaches that solve both transient and steady-state

19

problems is the correction of the incoming distribution function at interface nodes to satisfy the conjugate conditions. This procedure is necessary for straight [42, 43, 44] as well as curved interfaces [38]. The proposed methods then require the identification of interface points and the angle between the lattice velocity components and the normal to the interface. In multiphase or multicomponent systems with complex (time-dependent) interfaces, this becomes computationally demanding.

In this chapter, we introduce an alternative LBM formulation which solves the conservative form of the energy equation and does not require tracking and correcting for the presence of interfaces. Solving the conservation form of the energy equation instead of an advection-diffusion equation offers valuable advantages. It conserves conductive and advective flux simultaneously. Moreover, because the conjugate heat transfer solution procedure is independent of the interface topology, the model we propose remains efficient even for natural systems with complex and moving interfaces. Section 2.2 gives a brief introduction to LBM for typical advection-diffusion problems. In Section 2.3, we recover the conservation form of the energy equation from the advection-diffusion equation. We proceed with a description of the LBM formulation for conjugate heat transfer and discuss different approximations for the source term. In Section 2.4, we present several numerical tests that allow us to examine the efficiency of our model under steady-state and transient heat transfer conditions using both simple and complex interfaces. Section 2.5 provides a detailed analysis of the proposed model and discusses possible generalizations of the method for future studies.

2.2 LBM for advection-diffusion equation

In the present paper, we use the following single-relaxation time (BGK) lattice Boltzmann equation for an advection-diffusion problem [46]:

$$f_i(\mathbf{x} + \mathbf{e}_i \delta t, t + \delta t) - f_i(\mathbf{x}, t) = -\frac{1}{\tau} \left[f_i(\mathbf{x}, t) - f_i^{eq}(\mathbf{x}, t) \right] + \delta t \cdot \mathbf{F}_i, \qquad (2.1)$$

where f_i is the distribution function in direction i, x is the spatial coordinate, t is time, τ is the dimensionless relaxation time, δt is the time step in lattice units, $\mathbf{e}_i$ is the microscopic velocity in the lattice direction i, and $\mathbf{F}$ is the vector that accounts for external forces and sources. In the present study, we use the following linear local equilibrium distribution function [47, 48, 49]:

$$f_i^{eq}(\mathbf{x}, t) = \omega_i \phi(\mathbf{x}, t) \left[1 + \frac{\mathbf{e}_i \cdot \mathbf{u}}{c_s^2} \right], \qquad (2.2)$$

where $\mathbf{u}$ is the advection velocity vector, ω_i are the lattice weights, and c_s is the dimensionless speed of sound of the lattice. It should be mentioned that the source term formulation presented in the next section is not limited to this specific linear equilibrium advection-diffusion model. It can be similarly implemented in any other advection-diffusion LB models using two relaxation times (TRTs), multiple relaxation times (MRTs), and using quadratic equilibrium functions (see, for example, [50, 51] and the references cited therein). However, for the problems covered in the present study, the authors found the BGK model with linear equilibrium model sufficient.

By using a Chapman-Enskog expansion, this lattice Boltzmann model retrieves the following advection-diffusion equation:

$$\frac{\partial \phi}{\partial t} + \nabla \cdot (\phi \mathbf{u}) = \nabla \cdot (\alpha \nabla \phi) + \mathbf{S}. \qquad (2.3)$$

where ϕ is the macroscopic scalar field and is defined as

$$\phi(\mathbf{x}, t) = \sum_i f_i. \tag{2.4}$$

$\mathbf{u}$ represents the velocity field variables, α is the diffusivity coefficient, and $\mathbf{S}$ is a source term. The link between the evolution of the distribution functions in Eq. 2.1 and the macroscopic advection-diffusion in Eq. 2.3 is established through the following relation between diffusivity α and relaxation time τ:

$$\alpha = c_s{}^2 \left(\tau - \frac{1}{2} \right) \partial t. \tag{2.5}$$

Equation 2.3 is generally referred to as the conservation form (divergence form) of the advection-diffusion equation for the scalar variable ϕ. In other words, the advective-diffusive flux $\mathbf{J} = -\alpha \nabla \phi + \phi \mathbf{u}$ is conserved in the equation. As mentioned in Sec. I, the objective of the present paper is to present a LBM formulation for solving the conservation form of the energy equation which takes the following form:

$$\rho c \frac{\partial T}{\partial t} + \nabla \cdot (\rho c \mathbf{u} T) = \nabla \cdot (k \nabla T) + \mathbf{S}, \tag{2.6}$$

where k, ρ, and c are, respectively, the thermal conductivity, density, and specific heat.

In general, for a heterogeneous medium, additional boundary conditions should be applied at the interface between the phases or components to ensure continuity of temperature and normal heat flux in the following form:

$$T^{I,+} = T^{I,-}, \tag{2.7}$$

$$\mathbf{n} \cdot (k\nabla T + \rho c\mathbf{u}T)^{I,+} = \mathbf{n} \cdot (k\nabla T + \rho c\mathbf{u}T)^{I,-}, \qquad (2.8)$$

where *I* represents the interface, *n* is normal to the interface, and + and - denote parameters on either sides of the interface. As shown by Eq. 2.8, the conserved total flux consists of two parts: (1) the conductive and (2) the advective or transport heat flux. However, since the solid phase is generally considered at rest in most cases, the heat flux at the interfaces is considered purely conductive. But when considering heat transfer between a moving discrete solid particle immerged in a fluid or in fluid-fluid systems such as two immiscible fluids, the total heat flux must be conserved at the interface. This general condition limits the applicability of previously reported conjugate heat transfer models to solid-fluid systems since they all conserve conductive heat flux rather than total heat flux at the interface.

2.3 LBM for conservation form of energy equation

In this section, we explain the details for deriving the conservative form of the heat transfer equation 2.6 from the conservative form of the advection-diffusion equation 2.3.

2.3.1 Conjugate treatment

First, consider the problem of pure one-dimensional (1D) heat conduction in a two-layered stratified system shown in Fig. 1, where two materials with different thermophysical properties are in perfect thermal contact. The medium shown in Fig. 2.1 is initially set at a uniform temperature $T_0 = 0$. At time $t > 0$, the upper boundary is elevated to $T_h > T_0$, while the lower boundary is kept at $T_c = T_0$, and vertical walls are adiabatic. We contrast two different equations for solving the heat conduction problem in this benchmark test. The first equation is the conservative form of the heat conduction equation [Eq. 2.9], and second is the conservative form of the diffusion equation [Eq. 2.10]:

23
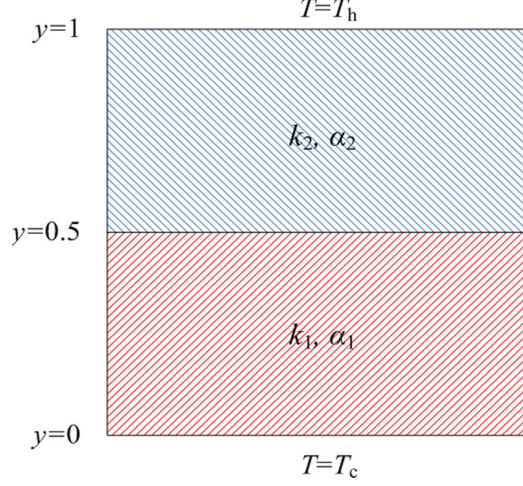
Figure 2.1: Schematic of two-layer stratified medium.

$$\frac{\partial T}{\partial t} = \frac{1}{\rho c}\frac{\partial}{\partial x}\left(k\frac{\partial T}{\partial x}\right),\tag{2.9}$$

$$\frac{\partial T}{\partial t} = \frac{\partial}{\partial x}\left(\alpha\frac{\partial T}{\partial x}\right).\tag{2.10}$$

It can be easily shown that, without applying any interface boundary condition, the finite-difference solution of the first conservative equations [Eq. 2.9] will match the analytical solution provided that some care is used to construct the computational mesh. In other words, as long as we are discretizing the *conservative* form of the energy equation and the interface geometry is straight, we retrieve the correct solution (temperature distribution) without applying any conjugate boundary conditions at the interface of a composite medium. On the other hand, the conservative diffusive form 2.10 can only deal with contrasts in thermal diffusivity. The temperature distribution that results from solving Eq. 2.10 is solely controlled by the contrast in thermal diffusivity. In other words, the diffusion equation does not provide a correct solution to conjugate heat transfer if the ratio of thermal conductivities does not match the ratio of thermal diffusivities. This is the direct

24
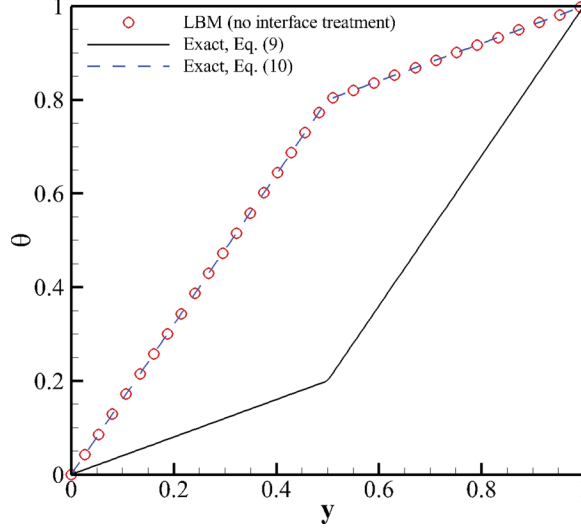
Figure 2.2: Comparison of LBM solution with analytical solutions for two-layered stratified medium.

consequence of conserving flux based on diffusivity α and not conductivity k in the second conservative formulation.

As an illustration, we use the advection-diffusion LBM model [Eq. 2.1] for solving heat conduction in a two-layer medium (Fig. 2.1) without using conjugate boundary conditions at the interface. The LBM results are compared with two analytical steady-state solutions based on conservative heat conduction and conservative diffusion equations in Fig. 2.2 ($k_1/k_2 = 4$ and $\alpha_1/\alpha_2 = 0.25$). The figure shows the profile of the dimensionless temperature $\theta = (T - T_c)/(T_h - T_c)$, and we see that the standard advection-diffusion LBM model solves the conservative form of the diffusion equation, i.e., Eq. 2.10. Therefore, even heat conduction in a simple composite medium with a straight interface geometry requires a specific treatment for the conjugate conditions at the interface.

In order to solve the conservative form of the energy equation 2.6, we first recast it from the advection-diffusion equation 2.3 by adding a source or sink term:

$$\frac{\partial}{\partial x_j}(Tu_j) = \frac{\partial}{\partial x_j}\left(\frac{\rho cTu_j}{\rho c}\right) = \frac{1}{\rho c}\frac{\partial}{\partial x_j}(\rho cTu_j) + \frac{\partial}{\partial x_j}\left(\frac{1}{\rho c}\right)(\rho cTu_j),$$
$$\frac{\partial}{\partial x_j}\left(\alpha\frac{\partial T}{\partial x_j}\right) = \frac{\partial}{\partial x_j}\left(\frac{k}{\rho c}\frac{\partial T}{\partial x_j}\right) = \frac{1}{\rho c}\frac{\partial}{\partial x_j}\left(k\frac{\partial T}{\partial x_j}\right) + \frac{\partial}{\partial x_j}\left(\frac{1}{\rho c}\right)\left(k\frac{\partial T}{\partial x_j}\right). \tag{2.11}$$

By inserting these two terms in Eq. 2.3, we recover the terms for conservation of energy equation 2.6. Rearranging the terms finally yields:

$$\frac{\partial T}{\partial t} + \frac{\partial}{\partial x_j}(Tu_j) = \frac{\partial}{\partial x_j}\left(\alpha\frac{\partial T}{\partial x_j}\right) + \underbrace{\frac{\partial}{\partial x_j}\left(\frac{1}{\rho c}\right)\left(-k\frac{\partial T}{\partial x_j} + \rho cu_j T\right)}_{S_{conj}} + \mathbf{S}, \tag{2.12}$$

where $\alpha = k/\rho c$ is the thermal diffusivity of each phase. As it can be seen from Eq. 2.12, the conservative form of the energy equation is equivalent to solving the conservative form of the advection-diffusion equation with a source term. Therefore, we can use advection-diffusion LBM models and introduce spatial variations in thermophysical properties that arise at the components interfaces as a forcing term. The direct consequence of this interface treatment is that in geometries with a straight (or staircased) interface, it will provide a correct temperature distribution based of heat flux automatically without any further interface treatment and correction of incoming distribution functions for transient and steady conditions.

2.3.2   *Source term treatment*

The source term in Eq. 2.12 consists of the product of the gradient of $1/\rho c$ with the total heat flux $q_i = -k\partial T/\partial x_i + \rho cu_i T$. One of the important features of LBM is that the flux vector can be calculated locally [43, 51]:

$$q_j = (\rho c)\left[\left(1 - \frac{1}{2\tau}\right)\sum_j (f_j - f_j^{eq})e_j + u_j T\right]. \tag{2.13}$$

The remaining term to be calculated in the source term is the gradient of $1/\rho c$. For this purpose, we first assume that the interface is located halfway between two adjacent lattice nodes. Then, we use the one-sided finite-difference approximation for calculating this term at each lattice point *k*, according to:

$$(\rho c)_{avg} = \frac{(\rho c)_k + (\rho c)_{k+1}}{2},$$

$$\frac{\partial}{\partial x_j}\left(\frac{1}{\rho c}\right)_k = \frac{\frac{1}{(\rho c)_k} - \frac{1}{(\rho c)_{avg}}}{\frac{\Delta x_j}{2}}.$$

(2.14)

ρc_{avg} is the average value of heat capacitance at the center point between lattice nodes *k* and *k +1* and x_j is the lattice grid spacing. According to Eq. 2.14, away from interfaces, ρc_{avg} will be constant and the source or sink term vanishes. The only place where it has a finite value is at lattice points adjacent to an interface, where the heat capacitance is heterogeneous. Therefore, the final source term used for treating the conjugate conditions at the interface becomes:

$$S_{conj} = \frac{\partial}{\partial x_j}\left(\frac{1}{\rho c}\right) \cdot q_j.$$

(2.15)

Here, we will use the following relation for adding the source term S_{conj} in advection-diffusion lattice Boltzmann formulation:

$$\mathbf{F}_i = \omega_i S_{conj}.$$

(2.16)

S_{conj} can be calculated for the whole computational domain. Its value will be zero everywhere except at the interface where it experiences a jump in heat capacitance. It should be mentioned that approximating a source term in LBM using a finite-difference method has been recently used successfully in several studies [52, 53, 54, 55].

In previous interface treatments for conjugate heat transfer, the distribution functions coming from the interface require a correction either during the collision or streaming process. The primary advantage of treating conjugate conditions as a source term is that it avoids any specific treatment that depends on the interface topology. This advantage becomes significant when dealing with physical domains with a large interface surface area between phases or components. Another context where the approach presented here provides a definite advantage is when one considers heat transfer in media with evolving microstructures in which the boundaries and interfaces change over time (melting or precipitation [56, 47]). In these cases, the present LBM formulation relies on a flag variable for each phase that is generally retrieved from the flow field simulation, but does not require additional constraints. The algorithm presented here is independent from the choice of lattice in LBM. Interface treatment based on the correction of distributions that cross the interface needs to be modified when applied to different lattices such as $D2Q5$, $D2Q9$, or their three-dimensional (3D) counterparts. Neither the calculation of heat flux in Eq. 2.13, nor the finite-difference approximation in Eq. 2.14 changes for different lattice arrangements. As we demonstrate in the next section, the present approach can be directly applied for straight interface geometries.

2.4 Numerical tests

In this section, six test cases are investigated. The first test is a steady-state convection-diffusion study in a horizontal channel in which a uniform velocity field is set parallel to the interface between two fluid layers. The second case study is steady-state convection-diffusion in a channel where the uniform velocity field is set normal to the interface between two fluid layers. In the third case study, we investigate transient and steady-state heat conduction in a three-layered stratified medium. We then examine the performance of the model on curved boundaries in a steady-state heat conduction problem in concentric disks. In all cases, the LBM solution is compared to analytical solutions. The next
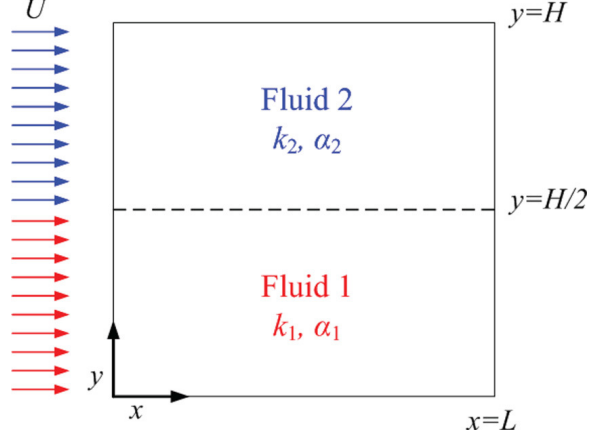
Figure 2.3: Schematic of 2D convective channel with horizontal interface.

case consists of heat conduction in a heterogeneous medium with random microstructures. The final application of the model considers natural heat convection in a square enclosure with discrete solid obstacles characterized by thermal properties that differ from the fluid. Since the present source term treatment has been formulated for a composite or multiphase medium with different thermophysical properties, different values for the ratios of thermal conductivities and thermal diffusivities will be used in all test cases.

2.4.1   Steady-state convection-diffusion in a channel with horizontal interface

We consider heat transfer in a horizontal channel where two fluids with different thermo-physical properties are flowing with a constant uniform velocity U along the x direction. A schematic of the setup is shown in Fig. 2.3 where the interface is represented by a dashed line.

Vertical boundaries are subjected to periodic conditions. Horizontal walls have fixed sinusoidal temperatures (Dirichlet boundary conditions):

$$T(x, y = 0) = T(x, y = H) = \cos(\omega x), \quad \omega = 2\pi/L. \tag{2.17}$$

The analytical solution to the steady-state temperature distribution under these conditions is provided in Li et al. [38].
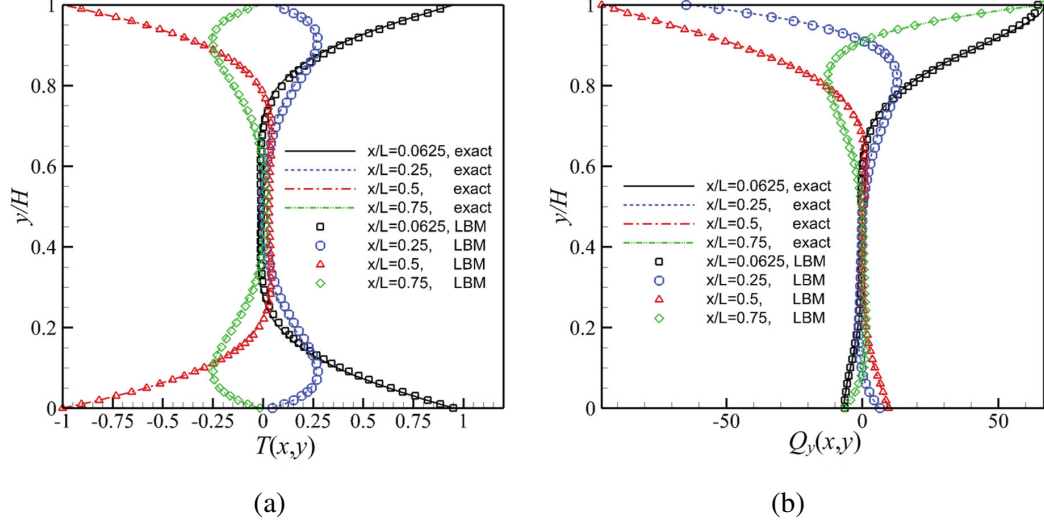
Figure 2.4: Comparison of LBM with the analytical solution: (a) temperature, (b) vertical heat flux, for $H = L = 1$, $L/x = 60$, $k_2/k_1 = 10$, $\alpha_2/\alpha_1 = 1.0$, and $\tau_1 = \tau_2 = 0.75$.

Figure 2.4 shows comparisons of the LBM solution with the analytical solution at different positions along x for $k_2/k_1 = 10$, $\alpha_2/\alpha_1 = 1.0$, and Peclet number $\mathrm{P}e = UH/\alpha_1 = 20$. Both temperature fields and heat flux $q_y = k\partial T/\partial y$ are in good agreement with the analytical solution.

The experimental order of convergence (EOC) of the present approach has been determined based on the L_2-norm error E_{L_2} of the temperature field and is displayed in Fig. 2.5. The present approach possesses a first-order EOC, which is due to the first-order finite-difference approximation of the heat capacitance gradient in the source term.

2.4.2 Steady-state convection-diffusion in a channel with vertical interface

In the previous problem, since the velocity field was parallel to the interface, the part of the conjugate source term related to advective heat flux was null. That explains why a strategy that only conserves the conductive heat flux at the interface can be successful. The purpose of the present case study is to test the model for a more general condition where both advective and conductive heat flux must be conserved at the interface. For this purpose, we consider the convective channel shown in Fig. 2.6 in which two different fluids, separated
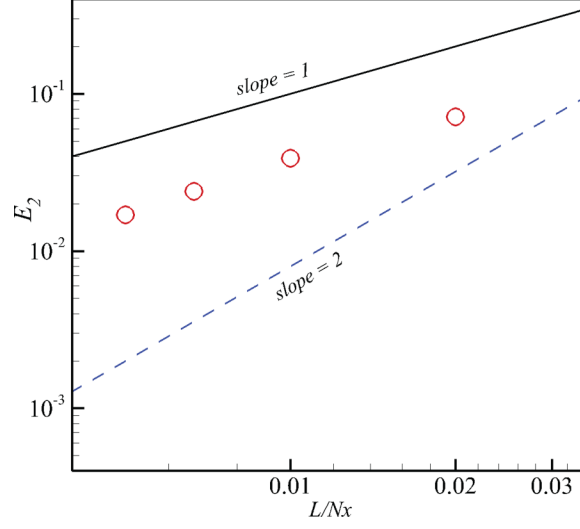
Figure 2.5: EOC based on L_2-norm error for convection diffusion in a horizontal channel.

by a vertical interface at $x = L/2$, flow with uniform velocity U along x. The vertical walls at $x = 0$ and $x = L$ are maintained at constant temperature $T_1 = 0$ and $T_2 = 1$, respectively.

Symmetry boundary conditions are applied to the horizontal walls at $y = 0$ and $y = H$. The analytical solution for the temperature then becomes:

$$T(x) = -\frac{\lambda_1}{U}\alpha_1 + \lambda_2 e^{U\alpha_1 x}, \quad 0 \leq x \leq x_{int}, \tag{2.18}$$

$$T(x) = -\frac{\lambda_3}{U}\alpha_2 + \lambda_4 e^{U\alpha_1 x_{int}} e^{U\alpha_2(x-x_{int})}, \quad x_{int} \leq x \leq L, \tag{2.19}$$

where

31
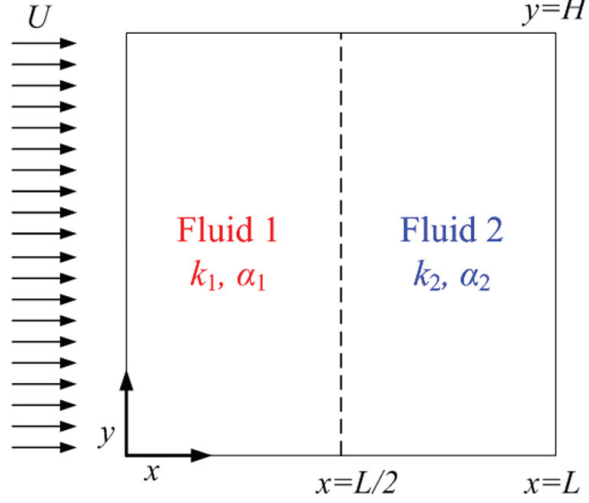
Figure 2.6: Schematic of convective channel with with uniform velocity normal to the vertical interface between both components.

$$\lambda_1 = \frac{-T_1 e^{-x_{int}/\gamma_1} + T_2/e^{-(L-x_{int})/\gamma_2}}{\gamma_1(1 - e^{-x_{int}/\gamma_1}) + \gamma_2(1/e^{-(L-x_{int})/\gamma_2} - 1)(k_1/k_2)},$$

$$\lambda_2 = T_1 - \gamma_1\lambda_1,$$

$$\lambda_3 = (k_1/k_2)\,\lambda_1,$$

$$\lambda_4 = \frac{T_2 - \gamma_2\lambda_3}{e^{-x_{int}/\gamma_1}e^{-(L-x_{int})/\gamma_2}},$$ (2.20)

$$\gamma_1 = -\frac{\alpha_1}{U},$$

$$\gamma_2 = -\frac{\alpha_2}{U}.$$

Figure 2.7 shows the comparison of the analytical temperature distribution with the LBM solution for the case of $k_1/k_2 = 5$, $\alpha_1/\alpha_2 = 0.05$, and $U = 1$. We observe that our model solution, which considers both advective and conductive flux in the source term formulation, predicts the correct temperature profile, while conserving only the conductive flux leads to a poor fit to the analytical solution and, especially, no kink at the interface.
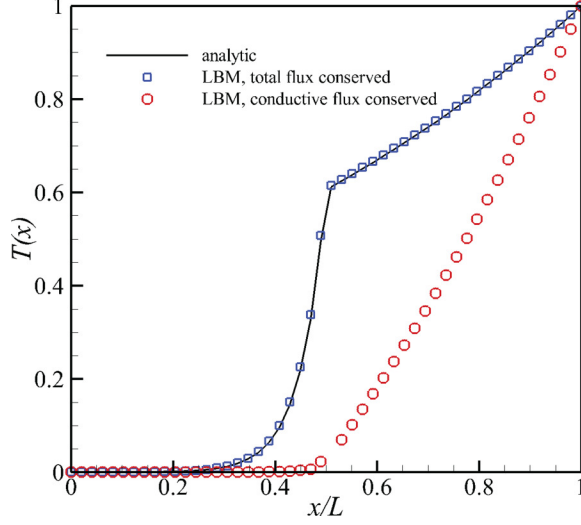
Figure 2.7: Comparison of LBM solutions with the analytical solution for $H = L = 1$, $L/x = 50$, $k_1/k_2 = 5$, $\alpha_1/\alpha_2 = 0.05$, $\tau_1 = 0.55$, and $\tau_2 = 1.5$.

2.4.3 Transient conduction in three-layered stratified medium

The purpose of this case study is to test our model's ability to deal with transient conjugate heat transfer. We investigate the transient heat conduction in the three-layer composite medium shown in Fig. 2.8. The thermophysical parameters used in the calculations are $k_{1,3} = 1.0$, $k_2 = 0.1$, $\alpha_{1,3} = 1.0$, and $\alpha_2 = 3.0$. The whole medium is initially set at a uniform temperature $T_0 = 0$. At time $t > 0$, the lower boundary temperature is elevated to $T_h > T_0$ while the upper boundary is kept at T_0 and the boundary condition on the vertical walls is adiabatic.

In Fig. 2.9, we show a succession of profiles for the dimensionless temperature $\theta = (T - T_0)/(T_h - T_c)$ that captures the transient evolution of the heat transfer in the domain. The comparison of our numerical results with the analytical solution from Sun and Wichman [57] confirms that the model simulates accurately both transient and steady-state heat transfer problems. The EOC for these calculations is determined from Fig. 2.10.

33
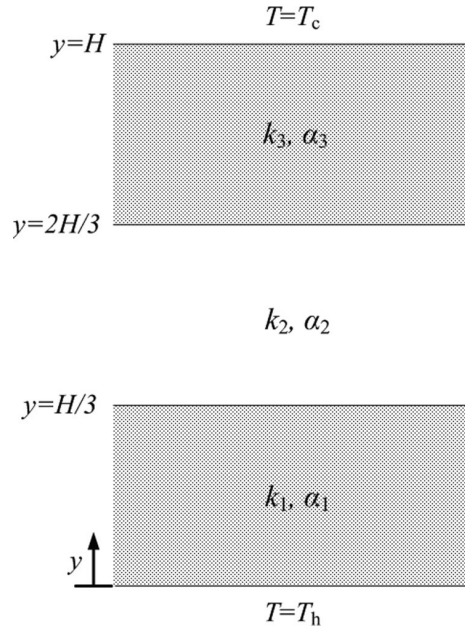
Figure 2.8: Three-layer stratified medium.
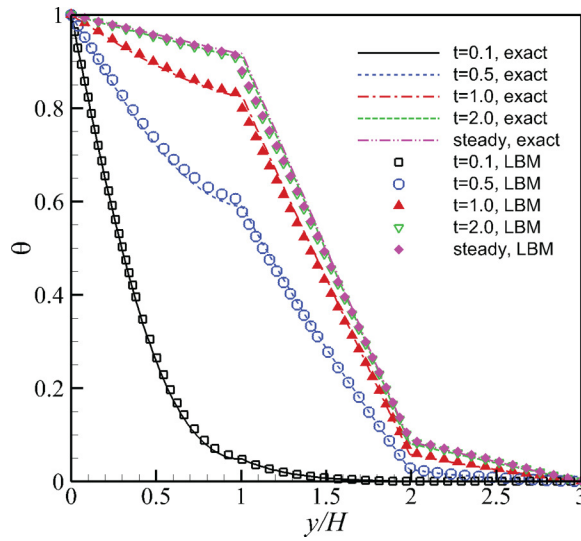
Figure 2.9: Analytical $vs.$ LBM solution for transient heat conduction in a three-layer stratified medium.
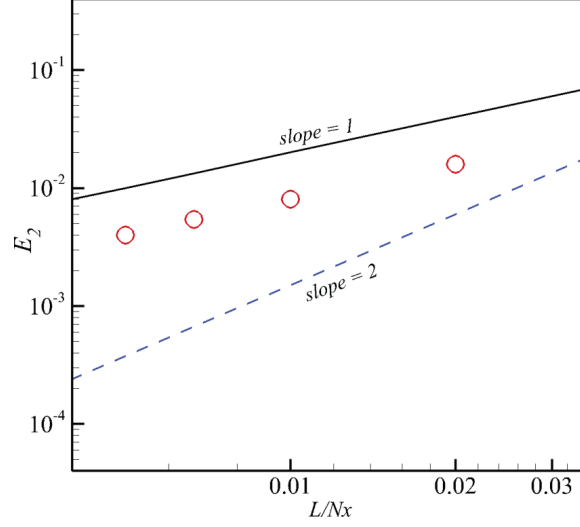
Figure 2.10: EOC based on L_2-norm error for conduction in a three-layer stratified medium.

2.4.4 Steady-state conduction in two-layer annulus

The two previous tests considered straight interfaces; the present case is designed to test our model against curved boundaries. Consider two concentric circular disks with different thermophysical properties as illustrated in Fig. 11. The outer boundary is subjected to the following Dirichlet condition:

$$T(r = R_2, \varphi) = \cos(n\varphi), \qquad (2.21)$$

where *n* is an integer number. For imposing Dirichlet boundary conditions 2.21 on the outer boundary, we employ the boundary treatment presented in Li et al. [45]. Because our source model does not yet include spatial interpolation to deal with curved and off-lattice interfaces, our aim here is to test the accuracy and behavior of the source sink term in conditions where the interface is no longer coplanar with the lattice. In other words, we approximate the curved interface with a staircase geometry. This first-order approximation is consistent with the order of the discretization for the heat capacitance in the source term. We note, however, that the source model we propose for interface conjugate heat transfer is general and can be refined to higher-order approximation if necessary.
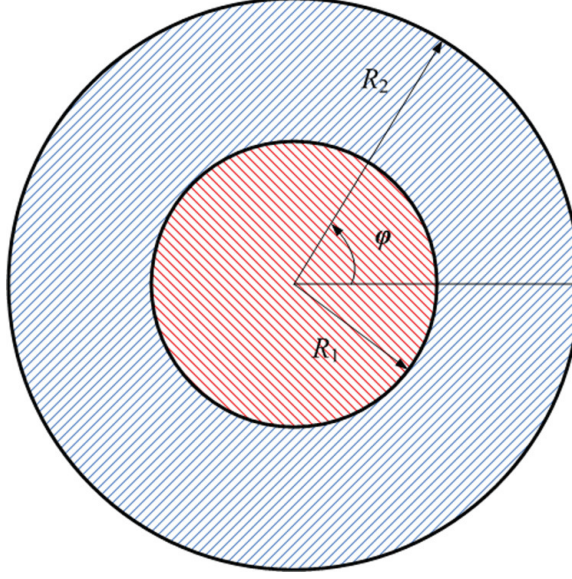
Figure 2.11: Schematic of a two-layer annulus.

The results from our LBM calculations, at steady state, are shown in Fig. 2.12 along with analytical solution from Li et al. [38]. The comparison is based on the following values for the parameters: $n = 2$; $R_2/R_1 = 2$, $k_1 = k_2 = 1$, $\alpha_1 = 0.2$, $\alpha_2 = 1.0$, $R_2/\Delta x = 150$, and $\tau_1 = 0.6$ and $\tau_2 = 1$. Results show that the radial distribution of temperature and heat flux along $\varphi_1 = 0$ and $\varphi_2 = \pi/2$ match the analytical solutions. For reference, we also show the solution with no interface treatment (S_conj = 0). As expected, for S_conj = 0, the LBM solution converges to the analytical solution based on the thermal diffusivity ratio [Eq. 2.10].

Our source term approach to conjugate heat transfer predicts a correct temperature and heat flux distribution for curved boundaries. The solution procedure does not require the correction of distribution functions at or near the interface and the calculations are independent of the domains geometry. This property makes this algorithm ideally suited to handle large calculations in complex natural heterogeneous media. We provide an example with a random microstructure in the next section.
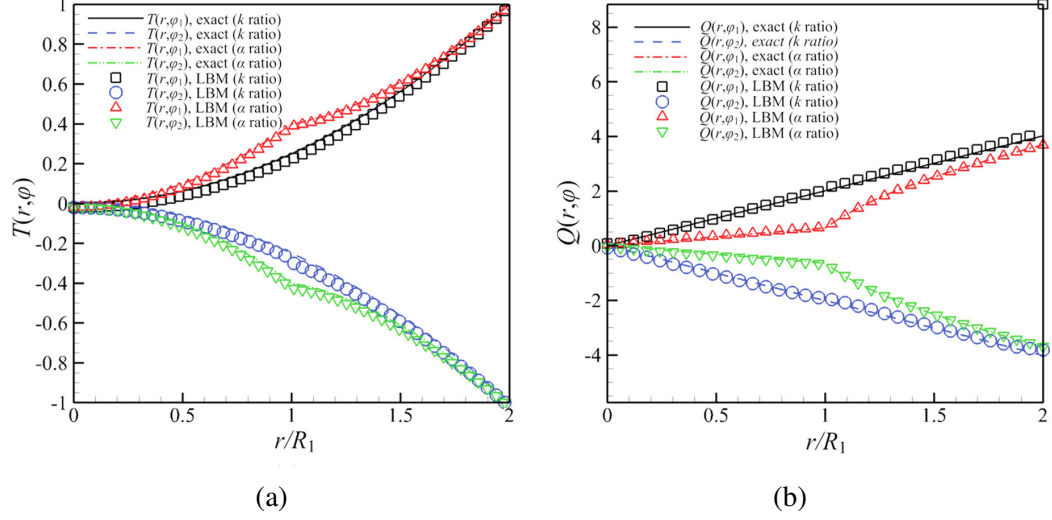
Figure 2.12: Radial distribution of (a) temperature, (b) heat flux in in the two-layer annulus domain.

2.4.5 Heat conduction in a heterogeneous media with random microstructures

Consider the two-component medium (inclusion and continuum phases) with random microstructures shown in Fig. 2.13. The microstructure has been generated by a simulated annealing stochastic optimization technique [58, 59]. The volume fraction of the inclusion phase is equal to 0.4. The choice of thermophysical properties for the inclusion and continuum phases are such that $k_{inc}/k_{cont} = 1.0$, and $\alpha_{inc}/\alpha_{cont} = 0.1$. The medium is initially set at temperature $T_i = 0$. At $t > 0$, the lower boundary is elevated to $T_h = 1.0$ while the upper boundary is kept at T_i. The vertical walls are set as no flux boundaries. Since thermal conductivities are the same for both phases, at steady state, the temperature solution should be a homogeneous temperature gradient from the lower to top boundary. For illustrative purposes, we show the temperature contours at steady state in Fig. 2.14 for two cases: with or without interface treatment (S_conj = 0). We observe that the source term correction for heterogeneous heat capacitance allows our model to better fit the linear temperature profile expected as the system approaches steady state.

For a better comparison, temperature profiles perpendicular to the heat flux are shown for different vertical positions in Fig. 2.15-(a), along with theoretical profiles shown as
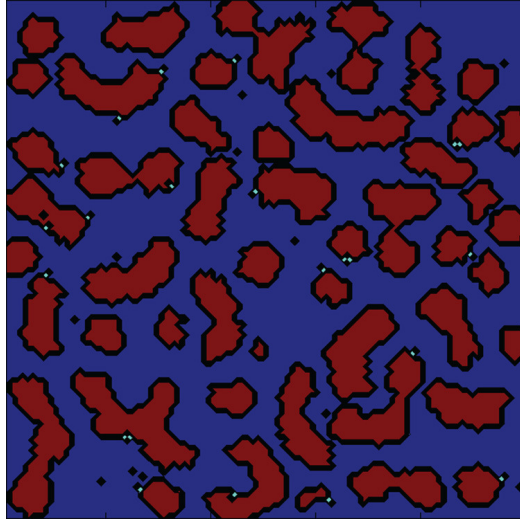
Figure 2.13: Constructed random heterogeneous medium (computational domain size: 100×100 grid points).

(a)   (b)
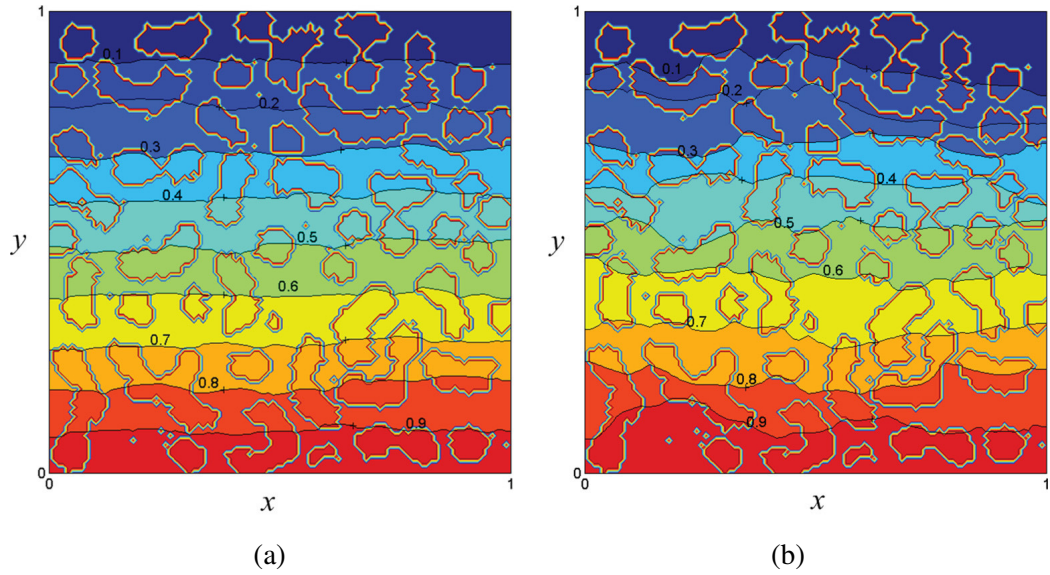
Figure 2.14: Temperature contour (a) by using S_conj, (b) without using S_conj.
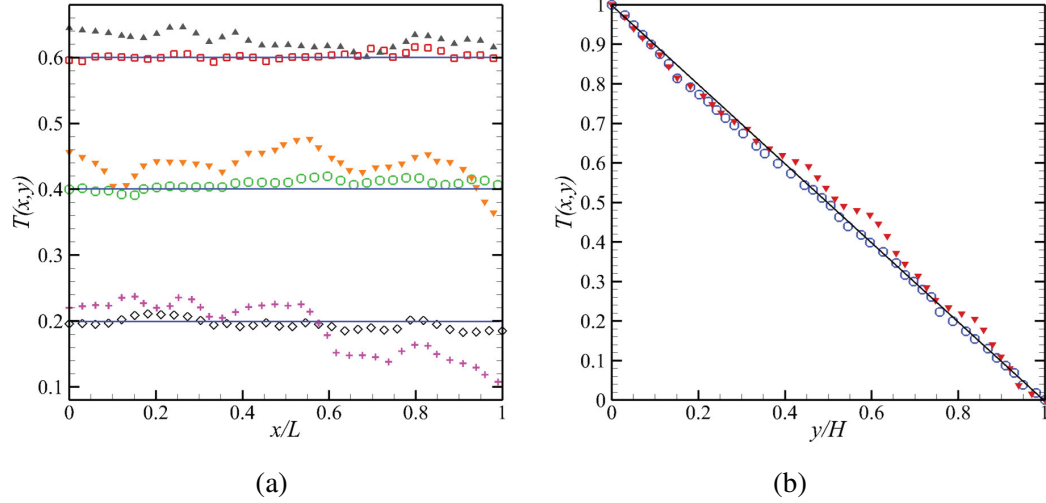
Figure 2.15: Temperature profile at (a) different vertical positions (from top to bottom: $y = 0.4,\ 0.6,\ 0.8$) with S_conj ($\square, \circ, \blacklozenge$) and without S_conj ($\blacktriangle, \blacktriangledown, +$); (b) horizontal position ($x = 0.5$) with S_conj ($\circ$), and without S_conj ($\blacktriangledown$).

solid lines. The profiles show that the proposed interface treatment predicts the correct temperature profile. Since thermal diffusivities of the two phases are different, the LBM solution with S_conj = 0 is far from a uniform profile along each horizontal transect. Figure 2.15-(b) shows the temperature profile along a vertical transect at $x = 0.5$. The small discrepancies of our results with the source term correction with the linear profile are due to the spatial resolution.

2.4.6 *Application: Natural convection in porous enclosure*

In order to show the potential of the present LBM model to simulate advective heat transfer in heterogeneous media, we consider the problem of natural convection in a square enclosure containing solid obstacles with different thermal properties. This problem leads to the coupling of the momentum and energy equations through the buoyancy term and requires simultaneous solution of momentum and the energy equations. The details on modeling natural convection using LBM can be found, for example, in Mohamad and Kuzmin [60]. Here, we use the bounce-back scheme for no-slip flow conditions and complement it with our model for conjugate interface conditions between solid and fluid phases. For
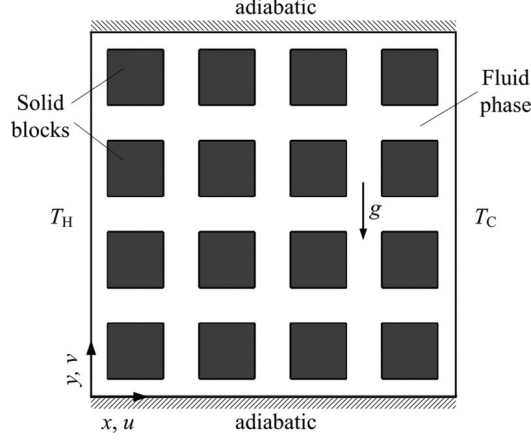
Figure 2.16: Schematic of porous enclosure.

this purpose, we consider the physical system shown in Fig. 16. The porous enclosure is heated from the left side (constant hot and cold temperatures on left and right walls, respectively), while horizontal walls are kept insulated. The porous medium shown in this configuration has numerous scientific and technological applications and has been studied extensively [1]. The numerical simulations are performed for a Rayleigh number equal to $Ra = g\beta H^3(T_H - T_C)/\nu\alpha_f = 10^5$, where g and β are gravitational acceleration and thermal expansion coefficient of the fluid, respectively. H is the height of the square enclosure. ν and α_f are the kinematic viscosity and thermal diffusivity of the fluid phase. For the purpose of validation, the Nusselt number computed at the hot wall is compared with values computed with numerical simulation using the finite-volume method reported in Merrikh and Lage [61], Raji et al. [62]. The Nusselt number is defined as:

$$\text{Nu} = \int_0^H \frac{\partial\theta}{\partial x}dy, \tag{2.22}$$

where $\theta = (T - T_C)/(T_H - T_C)$. For the buoyancy force in the hydrodynamic lattice Boltzmann model, we selected Scheme I in Mohamad and Kuzmin [60]. The results of our calculations are summarized in Table 2.1. The comparison of the averaged Nusselt number of our LBM model with those calculated from the finite-volume models of Merrikh and
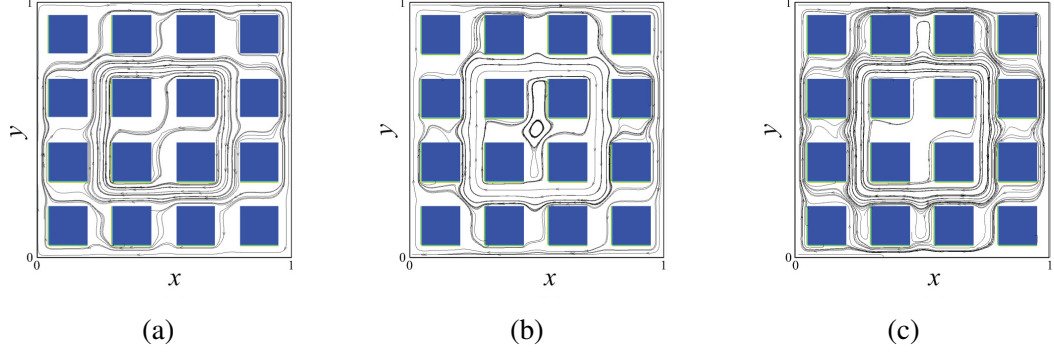
Figure 2.17: Streamlines for $Ra = 10^5$: (a) $k_s/k_f = 0.1$; (b) $k_s/k_f = 10$; (c) $k_s/k_f = 100$.
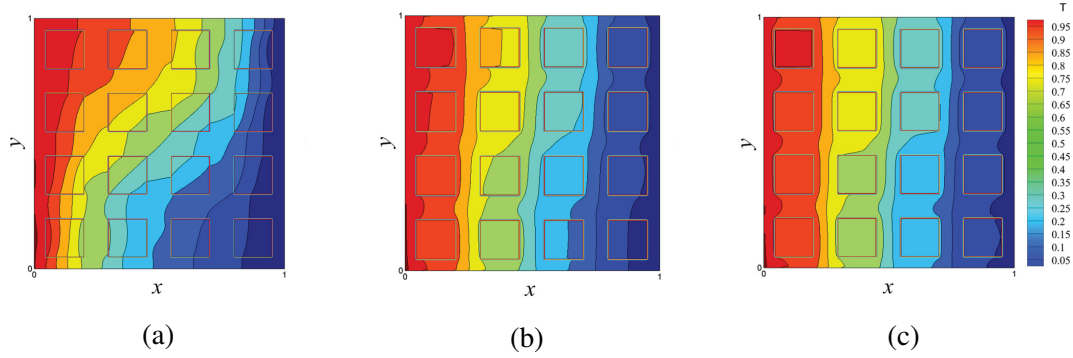
Figure 2.18: Isotherms for $Ra = 10^5$: (a) $k_s/k_f = 0.1$; (b) $k_s/k_f = 10$; (c) $k_s/k_f = 100$.

Lage [61], Raji et al. [62] shows that our algorithm is successful for simulating natural convection in complex geometries over a wide range of thermophysical properties between phases. This has been further verified with the results listed in Table 2.2 where we present the average Nu for the case of $k_s/k_f = 100$ and different heat capacitance ratios. We observe that a wide contrast in thermophysical properties of solid and fluid phases, which can be achieved in real materials, can be modeled accurately with the present source term formulation. The streamlines and isotherms for the cases mentioned in Table 2.1 have been shown in Figs. 2.17 and 2.18, respectively.

2.5 Discussion

LBM has proven to be an efficient computational tool for studying fluid flow in complex geometries due to the efficiency of the bounce-back boundary condition. However, from

Table 2.1: comparison of averaged Nusselt number, $Ra = 10^5$, $Pr = \nu/\alpha_f = 1$, $\alpha_s/\alpha_f = 1$.

k_s/k_f	[61]	[62]	Present LBM model
0.1	0.813	0.785	0.7969
1	1.233	1.193	1.185
10	2.030	2.066	2.031
100	2.313	2.394	2.4506

Table 2.2: Comparison of averaged Nusselt number, $Ra = 10^5$, $Pr = \nu/\alpha_f = 1$, $k_s/k_f = 100$.

$(\rho c)_s/(\rho c)_f$	100	500	1000
Nu	2.4506	2.4405	2.4421

a heat transfer standpoint, satisfying conjugate or jump boundary conditions is more complicated and generally relies on orientation-dependent internal boundary conditions. The central objective of the present study was to revisit the original conservation form of the differential equation that LBM solves in general convection-diffusion problems. Discretizing the conservation form of the *energy* equation automatically eliminates the need for applying the continuity of normal heat flux and temperature for straight interfaces. However, since LBM works with the conservation form of the advectiondiffusion equation rather than the energy equation, we need to apply jump conditions even for straight interfaces. This is due to the fact that flux conservation is based on the diffusivity α instead of the thermal conductivity *k* in the original LBM formulation. We propose a model where the conservation of energy is retrieved from the advection-diffusion equation with a source term. In essence, our algorithm replaces internal boundary conditions at interfaces with a source term that does not require any treatment specific to the interface geometry and orientation. The source term involves the gradient of the heat capacitance; we observe that the choice of finite difference approximation for that gradient controls the order of the overall scheme

(LBM is inherently second order in the absence of boundary conditions). The proposed model can easily accommodate higher-order discretizations as well as the introduction of curved boundaries (e.g., with the immersed boundary method), although these refinements are left for future studies. The results presented in previous sections highlight the following features:

1. EOC of the present interface treatment has been shown to be first order because of the finite-difference approximation in Eq. 2.14. Using higher-order computational stencils in Eq. 2.14 will increase the order of accuracy of the method.

2. The replacement of internal boundary conditions with a source term avoids calculating the local normal to the interface, and correcting distribution functions at adjacent grid nodes. This significantly reduces the computational demand of the algorithm. As we show with the random heterogeneous microstructure calculations, our model leads to an efficient and yet simple approach for studying heat transfer in complex geometries. The present model works well as long as curved boundaries can be approximated with staircase geometries. This in turn requires higher spatial resolution for capturing sharp curves. A hybrid implementation of the present formulation of LBM for the conservative energy equation with recently developed techniques on local grid refinements [63, 64, 65] and curve boundary treatment [45, 66] seems to be very promising for heat transfer problems in complex geometries.

3. The benefit of a model for heat transfer that is independent of the topology of the different components becomes significant in problems with evolving microstructure where interface boundaries change over time due to melting or solidification, for example. The present LBM model only uses the information from the main flow field and interface-tracking or front-tracking solver and adds no more computational steps by itself. Therefore, the present source term treatment can be implemented in any available hydrodynamic and advection-diffusion LBM models for evolving and

moving boundary problems.

4. The present source term formulation is not restricted to two-phase or two-component media. For the case of multiphase or multicomponent problems, the source term treatment can be used without any further modification.

5. The source term formulation for the jump condition in thermal properties is independent of lattice arrangements. It can be applied similarly to any lattice arrangements in 2D or 3D using any LBM models for advection diffusion with a proper evaluation of the heat flux in Eq. 2.13. The conjugate heat transfer approach presented here can also be naturally extended to multiple-relaxation thermal lattice Boltzmann models [67, 68, 69].

2.6 Conclusions

Based on reformulating the conservation form of the energy equation, we present a lattice Boltzmann model for heat transfer in heterogeneous material. The jump conditions appear as a source term in LBM formulations. The replacement of a specific interface treatment with a source term in the collision step offers several advantages. The advantages come from the fact that the proposed LBM formulation directly solves the conservation form of the energy equation. The reliablity of the model has been validated with several heat transfer problems under both steady-state and transient conditions.

CHAPTER 3

PORE-SCALE ANALYSIS OF HRL CONVECTION

In the previous chapter, we developed a numerical model based on the lattice Boltzmann method to solve for conjugate heat transfer within porous media subjected to thermal flows. This model solves the conservation equations at the pore-scale and therefore does not require the closure terms associated with homogenization procedures. We are therefore now in a position to contrast the performance of continuum-scale thermal flow models for natural convection in porous media with the outputs of the lattice Boltzmann pore-scale model and discuss the validity and limitations of the two most common formulations for the continuum-scale energy conservation equation. The content of this chapter is published in *Physical Review E*, under the title 'Role of thermal disequilibrium on natural convection in porous media: Insights from pore-scale study' [70].

3.1 Introduction

Modeling Horton-Rogers-Lapwood (HRL) convection is generally based on using average-scale formulations for the momentum and energy equations. Darcy and extended Darcy models such as Dupuit-Darcy (sometimes known as Forchheimer's model) and Brinkman-Darcy are the most commonly used models to simulate fluid flow through a porous medium [1]. The formulation of the average-scale energy equation depends on the assumption of local thermal equilibrium among the different phases [1]. Assuming a local thermal equilibrium (LTE) allows us to recast the statement of energy conservation into a single temperature equation, while the absence of local thermal equilibrium requires coupled energy equations - one for each phase (LTNE). The degree of disequilibrium between phases during natural thermal convection has therefore a significant effect on heat transfer and convective patterns.

In this chapter, we consider a fluid-saturated porous medium subjected to a vertical temperature gradient. This problem, which is analogous to Rayleigh-Bénard convection was first studied by Horton and Rogers [15] and Lapwood [16] (hereafter called HRL convection). They performed a linear stability analysis and identified the condition under which convective patterns emerge. The transition is generally parameterized by a modified critical Rayleigh number that is predicted to be $Ra_{cr} = 4\pi^2$ for a horizontally infinite porous domain, and for 2-dimensional square box. This critical value is valid as long as the momentum equation follows Darcy's law and the phases are locally in thermal equilibrium (LTE).

Several experimental studies reported values of heat transfer (Nusselt number) and critical Rayleigh number that deviate from the theoretical predictions made for HRL convection with the Darcy-LTE model e.g. [2, 71, 13]. These experiments also suggest that the contrast in thermal conductivity between the solid and liquid phases exacerbates the discrepancy. We focus on constraining the role of the solid-to-fluid thermal conductivity ratio to test which model is better suited for the energy conservation in the context of HRL convection in porous media. The knowledge of the *pore-scale* temperature distribution in both fluid and solid phases is necessary to assess the existence or absence of local thermal equilibrium between phases. For this purpose, we conduct direct numerical simulation (DNS) at the pore-scale level over a 2D porous structure consisting of regular arrangements of solid blocks. The advantage of these pore-scale calculations is that they allow us to consider a range of solid-to-fluid thermal conductivity ratios and also it does not rely on a homogenization model for the energy equation (LTE versus LTNE, for example) where the pore-scale information is filtered out. The DNS calculations are thus designed to test the validity of continuum-scale models under different conditions. The numerical model is based on the lattice Boltzmann method (LBM) that has been presented in Chapter 2.

We first analyze the performance of LTNE models to assess the role of local thermal disequilibrium on heat transfer around and beyond the critical Rayleigh number Ra_{cr}. We

perform a linear stability analysis to calculate the critical Rayleigh number, as well as the convective mode at the onset of convection for a range of inter-phase heat transfer coefficient values. We then conduct DNS simulations over a range of Rayleigh numbers for various solid-to-fluid thermal conductivity ratios to find: (1) the degree of local thermal disequilibrium under steady conditions, (2) the prevailing convective mode near the onset of convection, (3) the critical Rayleigh number where convection starts, and (4) the relationship between heat transfer (Nusselt number *Nu*) and thermal forcing as represented by *Nu-Ra* curves.

The organization of the chapter is as follows: In section 3.2, we present the mathematical formulation of the pore-scale and continuum-scale models for HRL convection. Section 3.3 presents the thermal performance of LTNE models. Section 3.4 provides the results of pore-scale DNS calculations for HRL convection and the comparison of the results with the corresponding LTE and LTNE models. Finally, we discuss possible causes for the mismatch between continuum and pore-scale models in section 3.5.

3.2 Mathematical Formulation

3.2.1 Pore-scale

We consider the 2-dimensional porous media shown in Figure 3.1 as our pore-scale physical domains. The 2-dimensional porous enclosure has the aspect ratio of one, $\Gamma =$ height (*H*)/width (*W*)=1. The domain consists of 10×10, 15×15 and 20×20 regular and identical unit cells containing square solid blocks of dimension d such that H/d ranges from 14.1 to 28.2. In Figure 3.1, the solid blocks are represented by the gray pixels, while the white pixels between the blocks represent the fluid pahse. The porosity of the medium is $\varphi = 0.5$ for all pore-scale domains. The choice of 20 layers in our study is solely based on the compromise between the computational cost (due to the computationally intensive simulations for detailed pore-scale analyses) and retrieving a statistically relevant set of results to interpret at the continuum scale. Since we intentionally designed our domain to be a *priori*
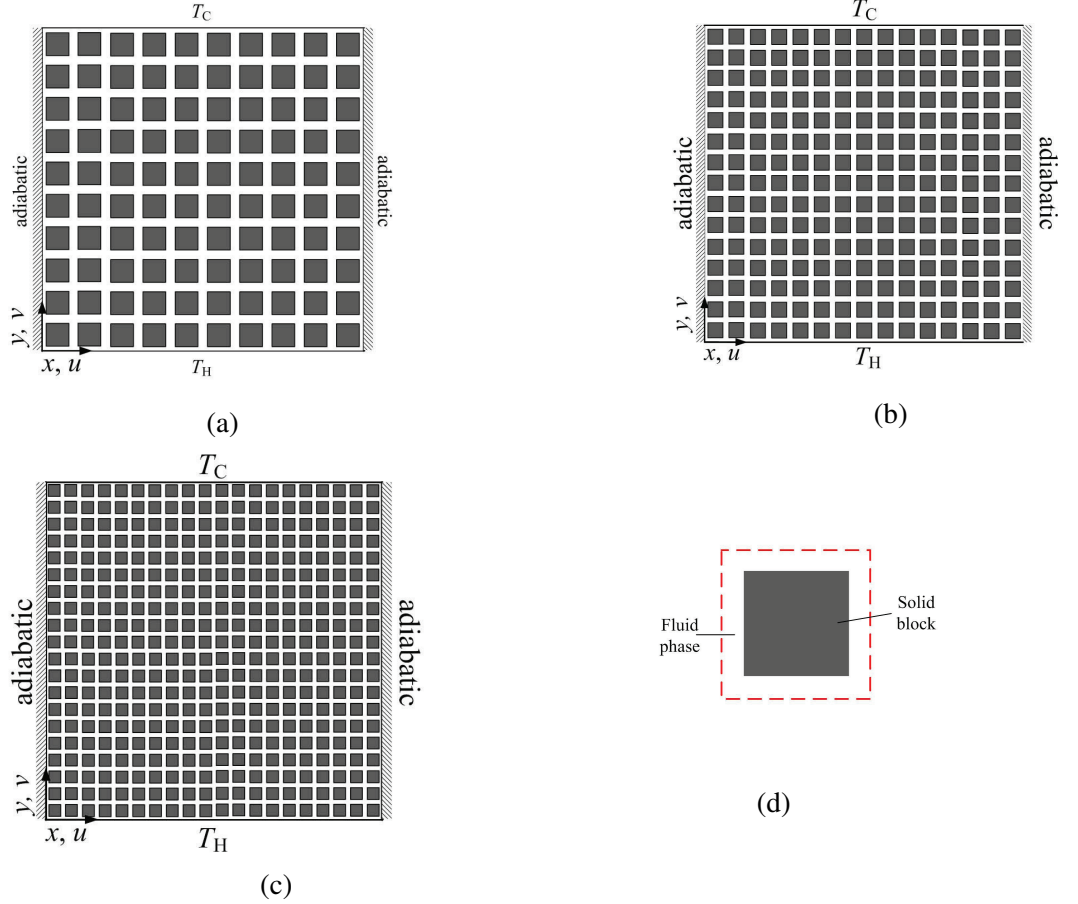
Figure 3.1: Physical domains in the pore-scale study: (a) 10×10 unit cells, (b) 15×15 unit cells, (c) 20×20 unit cells, (d) unit cell (dashed line showing the periodicity)

periodic, it becomes natural to select the unit cell to be the representative volume element (RVE) and also the averaging volume [22] and it thus eliminates the uncertainty in defining the representative averaging volume. The same procedure has been used extensively in similar studies, see for example in [24, 19, 72, 73, 22]. We show later in Section 3.5 that the pore-scale simulations successfully recover the important physical features of the HRL convection and the results are independent of the coarsness of the solid blocks.

The pore-scale analysis of HRL convection is based on the direct numerical simulation of conservation equations for both constituents for the 2-dimensional porous media shown in figure 3.1. For the fluid phase, the Navier-Stokes and energy equations are (using the Boussinesq approximation):

$$\nabla \cdot \boldsymbol{u} = 0, \tag{3.1}$$

$$\frac{\partial \mathbf{u}}{\partial t} + (\mathbf{u} \cdot \nabla)\mathbf{u} = -\frac{1}{\rho}\nabla P + \nu\nabla^2\mathbf{u} + \mathbf{g}\beta(T - T_{ref}), \tag{3.2}$$

$$(\rho c)_f \frac{\partial T}{\partial t} + \nabla \cdot ((\rho c)_f \mathbf{u}T) = \nabla \cdot (k_f \nabla T), \tag{3.3}$$

where $\mathbf{u}$ is the pore-scale velocity field, P is the pressure, T is the temperature, ν is the kinematic viscosity of the fluid, β is the thermal expansion coefficient, $\mathbf{g}$ is the gravitational acceleration, k refers to thermal conductivity, c is the specific heat and ρ the density of the fluid phase (subscript f). For the solid phase, the energy equation reduces to:

$$(\rho c)_s \frac{\partial T}{\partial t} = \nabla \cdot (k_s \nabla T), \tag{3.4}$$

where the subscript s refers to the properties of the solid phase. Across a fluid-solid interface I, the continuity of temperature and normal heat flux yields:

$$T^{I,+} = T^{I,-} \tag{3.5}$$

$$\mathbf{n} \cdot (k\nabla T + \rho c\mathbf{u}T)^{I,+} = \mathbf{n} \cdot (k\nabla T + \rho c\mathbf{u}T)^{I,-},$$

where $\mathbf{n}$ is normal to the interface and $+$ and $-$ denote the different sides of the interface. The hydrodynamic and thermal boundary conditions are those for HRL convection and are set with:

$$(u, v) = 0, \quad T = T_H, \quad \text{for} \quad y = 0, \quad \text{for all} \quad x, \tag{3.6}$$

$$(u, v) = 0, \quad T = T_C, \quad \text{for} \quad y = H, \quad \text{for all} \quad x, \tag{3.7}$$

$$(u, v) = 0, \quad \frac{\partial T}{\partial x} = 0, \quad \text{for} \quad x = 0, 1, \quad \text{for all} \quad y. \tag{3.8}$$

These governing equations are solved with the lattice Boltzmann method (LBM) [74, 35, 36]. However, since the fluid-saturated porous matrix at the pore-scale level comprises a thermally heterogeneous system due to different thermophysical properties between solid and fluid, we resort to a thermal LBM model designed to satisfy the conjugate interface boundary conditions described by (3.5). In recent years, several thermal LBM models have been developed for solving the conjugate heat transfer problems [38, 75, 76, 77, 78, 79, 80, 81, 82], the present calculations follow the procedure described in Chapter 2 for the thermal energy equation. We used a single-relaxation time D2Q9 lattice Boltzmann model for both the velocity and temperature distribution functions. There are several approaches for applying the no-slip boundary condition [83, 84]. In the present study, Zou-He's bounce-back scheme of the nonequilibrium part of the particle distribution functions [84] is used to implement no-slip conditions at solid boundaries, and the thermal counter-slip method is applied to enforce both Dirichlet and Neumann boundary conditions for the energy equation [85, 86]. In the pore-scale simulations, we used 60×60 grid points resolution over each unit cell. The lattice Boltzmann parameters were selected such that the Mach number is sufficiently small to stay within the incompressibility limit.

The regular configuration of repeated unit cells provides us with a straightforward test for the LTE and LTNE assumptions. We can compute local phase averages $\langle T_i \rangle^i$ over each

unit cell with:

$$\langle T_f \rangle^f = \frac{1}{V_f} \int_V T_f \, dV = \frac{1}{\phi V} \int_V T_f \, dV,$$

$$\langle T_s \rangle^s = \frac{1}{V_s} \int_V T_s \, dV = \frac{1}{(1 - \phi)V} \int_V T_s \, dV. \tag{3.9}$$

In order to compare the pore-scale results with the continuum-scale predictions, we need to compute the Darcy-Rayleigh number *Ra** and average Nusselt number *Nu** which are defined as:

$$Ra^* = \frac{g\beta(T_H - T_C)KH}{\alpha_m \nu_f} = Ra_f \cdot Da \cdot \frac{k_f}{k_m},$$

$$Ra_f = \frac{g\beta(T_H - T_C)H^3}{\alpha_f \nu_f}, \quad Da = \frac{K}{H^2},$$

$$Nu^* = 1 + \frac{1}{A} \frac{\int_A u_y \cdot T \, dA}{\alpha_m \Delta T / H}, \tag{3.10}$$

$$\alpha_m = \frac{k_m}{(\rho c)_f}.$$

Ra_f is the conventional Rayleigh number based on the fluid properties. In *Ra**, *K* is the permeability of the porous medium and α_m is the thermal diffusivity based on stagnant thermal conductivity of the solid matrix and hosted fluid k_m. *Da* is the Darcy number of the porous medium. We use our LBM model to compute the permeability and average properties of the heterogeneous media from the pore-scale calculations.

3.2.2 Continuum-scale

Assuming local thermal equilibrium, HRL convection at the continuum scale is described by:

$$\nabla \cdot \mathbf{q} = \mathbf{0}, \tag{3.11}$$

$$\frac{\mu}{K}\mathbf{q} = -\nabla P + \rho\mathbf{g}, \tag{3.12}$$

$$(\rho c)_m \frac{\partial T}{\partial t} + (\rho c)_f \mathbf{q} \cdot \nabla T = k_m \nabla^2 T, \tag{3.13}$$

where T is the local temperature averaged over both phases, c is the specific heat and ρ is the density. K is the permeability of the porous medium, P is the pressure, μ is the dynamic viscosity of the fluid and $\mathbf{q}$ is the seepage velocity (Darcy flux). The subscripts m and f refer to the properties of the solid/fluid mixture and the fluid, respectively. Equations 3.12 and 3.13 are coupled through the Boussinesq approximation (i.e. Eq. 1.3). It should be mentioned that k_m is not only a function of the thermal conductivity of each phase but it depends strongly on the structure of the porous medium. This structural control has been studied extensively both theoretically and experimentally and it is found that k_m cannot be defined simply as the volumetric arithematic or harmonic mean of the fluid and solid thermal conductivities [34, 87].

We can relax the local thermal equilibrium assumption by developing a model where the energy conservation for each phase is considered separately and coupled through an inter-phase heat exchange term [1]. This allows the two phases to experience different temperatures locally, which may appear more consistent with convection in porous media where the fluid and solid thermo-physical properties are different and the advection of heat may be highly spatially heterogeneous [1]. There are multiple derivations for the two-temperature models and the reader is referred to Rees and Pop [25] for an overview of the recent developments with LTNE approaches. In the present study, we consider two com-

mon models, which will be referred to as LTNE-1 and LTNE-2. The difference between the two models stems from the way they were developed. The LTNE-1 model, which is the simplest two-temperature model, is based on the following set of equations [1, 25]:

$$\varphi(\rho c)_f \frac{\partial T_f}{\partial t} + (\rho c)_f \mathbf{q} \cdot \nabla T_f = \varphi k_f \nabla^2 T_f + h(T_s - T_f), \tag{3.14}$$

$$(1 - \varphi)(\rho c)_s \frac{\partial T_s}{\partial t} = (1 - \varphi) k_s \nabla^2 T_s - h(T_s - T_f), \tag{3.15}$$

where h is the inter-phase heat transfer coefficient responsible for the non-equilibrium heat transfer between the different phases and φ is the porosity of the medium. The subscript s and f refer to solid and fluid phase properties, respectively. Summing Eqs. 3.14 and 3.15 and assuming thermal equilibrium, reduces the model to the single temperature (LTE) model with an effective mixture thermal conductivity $k_m = \varphi k_f + (1 - \varphi)k_s$ which is a volumetric average and not a true stagnant conductivity. This is one of the inconsistencies of the LTNE-1 model in the LTE limit. On the other hand, if we apply volume-averaging over the microscale energy equation, extra coupling terms between solid and fluid phases appear which are ignored in this (LTNE-1) formulation. Even for the case of pure heat diffusion, it has been shown that these extra coupling terms cannot be omitted from the general energy equation [24]. Keeping this in mind, Nakayama et al. [88] used the volume-averaging process and extended the previous works for heat conduction [24, 89] to convection-conduction heat transfer and derived the following LTNE-2 equations:

$$\varphi(\rho c)_f \frac{\partial T_f}{\partial t} + (\rho c)_f \mathbf{q} \cdot \nabla T_f = \nabla \cdot [(\varphi k_f + k_f G + k_{dis}) \nabla T_f] \\ + (-k_s G) \nabla^2 T_s + h(T_s - T_f), \tag{3.16}$$

$$(1 - \varphi)(\rho c)_s \frac{\partial T_s}{\partial t} = \nabla \cdot [((1 - \varphi)k_s + k_f G\kappa)\nabla T_s]$$
$$+ (-k_s G)\nabla^2 T_f - h(T_s - T_f), \tag{3.17}$$

where k_{dis} is the thermal dispersion conductivity, $\kappa = k_s/k_f$ and G is the tortuosity parameter [89]. The following equation has been proposed for calculating the tortuosity parameter G [89]:

$$G = \frac{k_m/k_f - \varphi - (1 - \varphi)\kappa}{(\kappa - 1)^2}, \tag{3.18}$$

which always gives a negative value for G and recovers the true stagnant thermal conductivity of the medium k_m. This can be easily verified by summing up Eqs. 3.16 and 3.17 together and assuming local thermal equilibrium, which yields $k_m = \varphi k_f + (1 - \varphi)k_s + k_f(1 - \kappa)^2 G$. Therefore, by knowing the thermophysical properties of each phase and also the stagnant thermal conductivity of the medium, we can find the value of the tortuosity parameter.

A critical aspect of using both LTNE formulations lies in the determination of the appropriate value of h. In general, h is known to depend on many factors including the detailed geometry of the porous medium, the porosity, the phase conductivities and diffusivities and also the pore-scale velocity field [90, 91].

3.3   LTNE Results

We perform a linear stability analysis for both LTNE models (details are provided in Appendix A) to find the critical mode and the critical Rayleigh number at the onset of convection. Figure 3.2 presents the results for the LTNE-1 model. Panel (a) shows how the critical Rayleigh number Ra_{cr} of the horizontal wave-modes $m = 1$ and 2 changes with the dimensionless inter-phase heat transfer coefficient $\mathcal{H}$ (defined in the Appendix- Eq. A.9).

54

The critical Rayleigh number at the onset of convection for each $\mathcal{H}$ is the minimum of the corresponding values for the two modes ($m = 1, \ 2$; higher modes yield even greater Ra_{cr}, not shown here). HRL convection is a multi-stable thermal system, meaning that different convection modes may co-exist at a given Rayleigh number. One of the distinguishing features of convective patterns with different horizontal mode m is the amount of heat that is transferred through the domain. Therefore, it is crucial that continuum-scale formulations, such as LTNE-1 and LTNE-2 models, predict a consistent and correct mode.

Figure 3.2-(a) shows that for the LTNE-1 model, in the limit $\mathcal{H} \to \infty$, i.e local thermal equilibrium between solid and fluid phases, the single-cell convection mode $m = 1$ is selected at the onset of convection and Ra_{cr} is higher than $4\pi^2$, the critical Rayleigh number based on Darcy-LTE model for a horizontally infinite domain or a square box (aspect ratio 1). The inconsistency here results from the mixture effective thermal conductivity k_m to differ from the true stagnant thermal conductivity of the medium in the LTNE-1 model. On the other hand, as $\mathcal{H} \to 0$, i.e extreme local thermal disequilibrium between solid and fluid phases, Ra_{cr} is lower than $4\pi^2$, indicating that convection initiates at lower Ra than predicted by the LTE model. In both limiting cases of $\mathcal{H} \to 0$ and ∞, $m = 1$ is the critical mode at the onset of convection. However, for intermediate values of $\mathcal{H}$, Figure 3.2 shows that the second horizontal mode $m = 2$ becomes the favored mode. This explains the local peak in $Nu(\mathcal{H})$ for a fixed Ra (here 50) shown in Fig. 3.2-(b). At high values of $\mathcal{H}$, since Ra_{cr} is larger than 50, convection is absent and the Nusselt number is equal to 1 as expected.

The behavior of the LTNE-2 model is different from LTNE-1, as shown in Fig. 3.3. Panel (a) shows the dependence of Ra_{cr} on $\mathcal{H}$. First for the whole range of $\mathcal{H}$ values, the dominant horizontal mode at the onset of convection is $m = 1$. Second, we can observe that, in contrast with LTNE-1, the critical Rayleigh number recovers the correct value in the LTE regime ($\mathcal{H} \to \infty$). On the other hand, we find Ra_{cr} to be always smaller than $4\pi^2$ over the whole range of interphase heat transfer coefficient and decreases with the degree
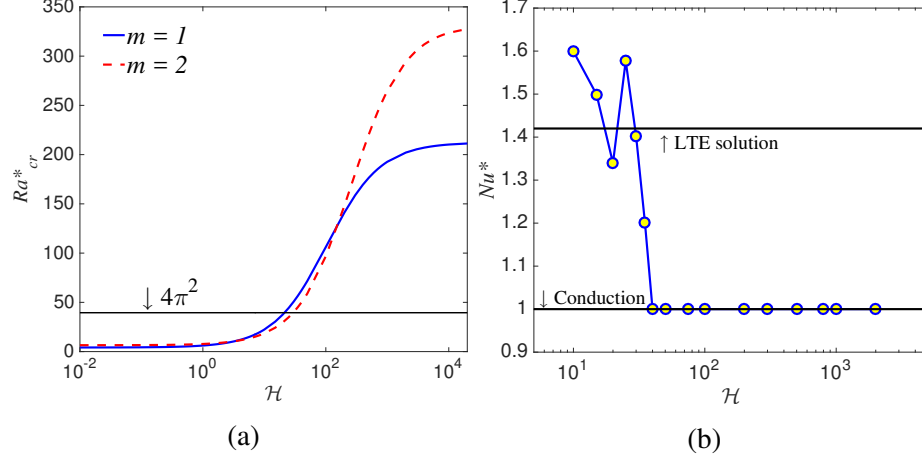
Figure 3.2: LTNE-1: (a) Variation of critical Rayleigh number Ra_{cr} for the horizontal wave modes $m = 1$ and 2 with dimensionless inter-phase heat transfer coefficient $\mathcal{H}$; (b) variation of Nusselt number *Nu* with $\mathcal{H}$ for $Ra = 50$.

of disequilibrium between phases. This suggests that, under local thermal disequilibrium conditions, the onset of convection is expected to occur at lower *Ra* with model LTNE-2 than LTE would predict, which also affects the Nusselt number (higher than expected from LTE model) as observed in Fig. 3.3-(b).

3.4 Pore-scale Results

3.4.1 Degree of local thermal disequilibrium

Figures 3.4 and 3.5 illustrate respectively the pore-scale temperature and velocity maps of 20×20 unit cells for different ratios of solid-to-fluid thermal conductivities $\kappa = k_s/k_f$ at $Ra^* = 80$. The detailed temperature and velocity maps in the pore-scale simulations of figures 3.4 and 3.5 enable us to image and study small (pore) scale flow and temperature distributions and test several average-scale assumptions including local thermal equilibrium and non-Darcian effects. We use Equations 3.9 and calculate the phase-averaged temperatures $\langle T_f \rangle^f$ and $\langle T_s \rangle^s$ over each unit-cell (shown in Figure 3.1-(d)) in the pore-scale temperature solution in Figure 3.4. This allows us to quantify the degree of local thermal disequilibrium between phase-averaged temperatures for each unit cell.
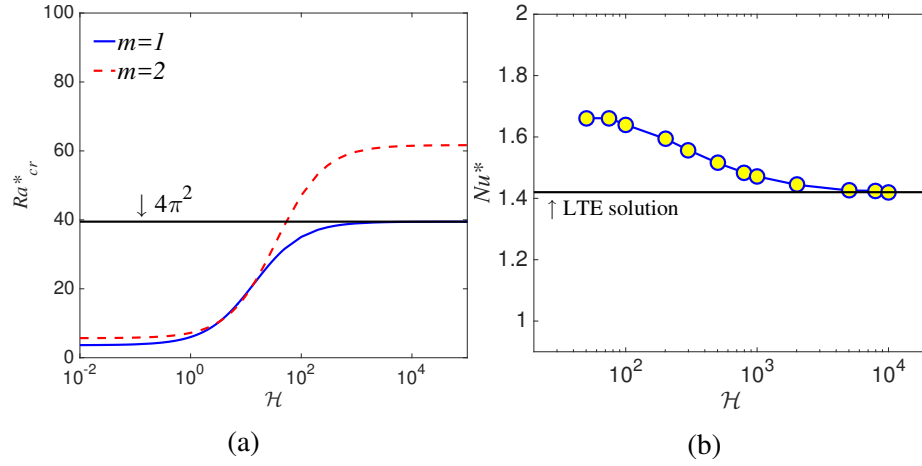
Figure 3.3: LTNE-2: (a) Variation of critical Rayleigh number Ra_{cr} for the horizontal wave modes $m = 1$ and 2 with dimensionless inter-phase heat transfer coefficient $\mathcal{H}$; (b) variation of Nusselt number Nu with $\mathcal{H}$ for $Ra = 50$.
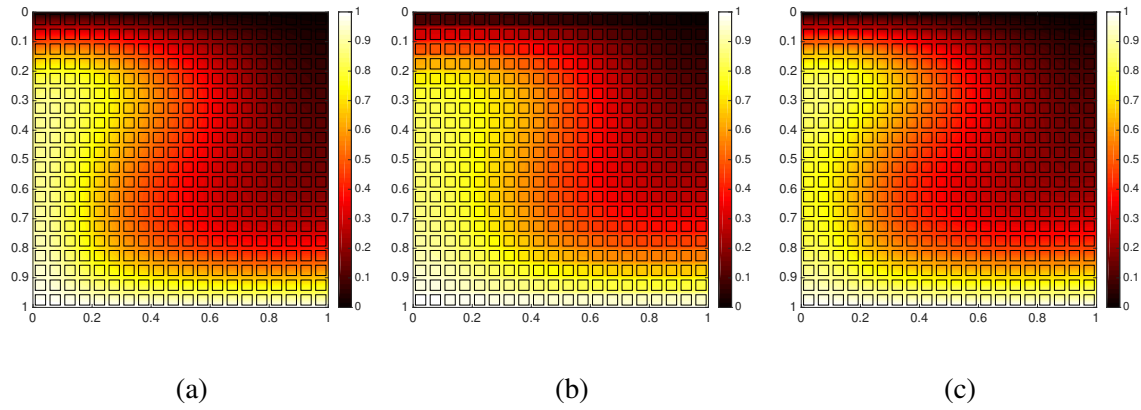
Figure 3.4: Steady temperature maps at $Ra^* = 80$ for 20×20 of unit cells; (a): $\kappa = 1$, (b): $\kappa = 50$ and (c) 1/13.

(a)   (b)   (c)
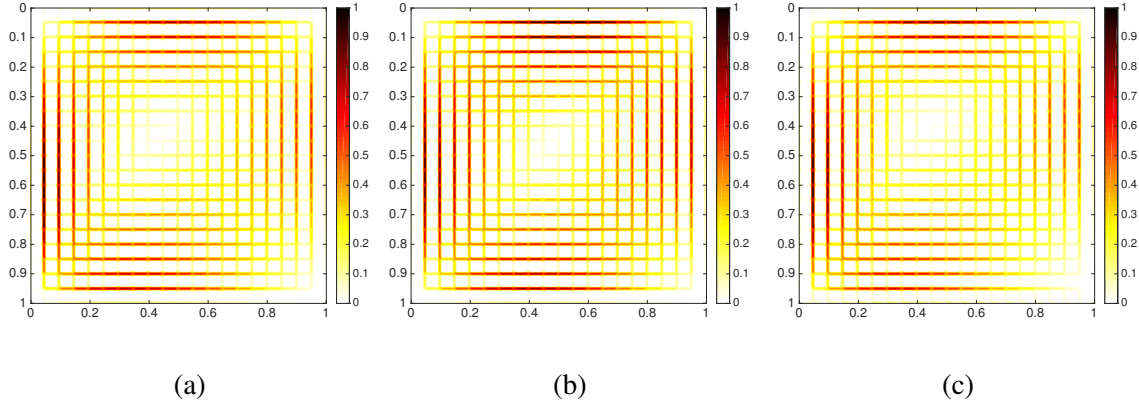
Figure 3.5: Steady velocity magnitude maps at $Ra^* = 80$ for 20×20 of unit cells; (a): $\kappa = 1$, (b): $\kappa = 50$ and (c) 1/13.

Figure 3.6 shows the maximum disequilibrium between phase-averaged temperatures observed at each Rayleigh number and for different thermal conductivity ratios. The maximum observed disequilibrium is below 2% for all κ values.

In order to quantify the significance of this level of thermal disequilibrium, we use the pore-scale data for the case where the solid matrix and fluid have the same thermal conductivity, i.e. $\kappa = 1$. Since $\kappa = 1$, the stagnant thermal conductivity of the porous medium is equal to the thermal conductivities of solid/fluid, i.e. $k_m = k_s = k_f$. In other words, the unit-cell is thermally homogeneous at the pore-scale level. We can use this case for comparing the pore-scale data with the corresponding Darcy-LTE solution to verify whether a thermal disequilibrium of $\lesssim 2\%$ leads to departure from LTE assumption or not. For comparison with the average-scale solution, the Darcy number of the porous structures in Figure 3.4 is calculated from our LBM model and is found to be $Da = 2.435 \times 10^{-5}$, $Da = 1.195 \times 10^{-5}$ and $Da = 7.594 \times 10^{-6}$ for 10×10, 15×15 and 20×20 domains, respectively. Figure 3.7 shows the comparison of the pore-scale heat transfer data with those from the average-scale formulations of [92] for a square box. The average-scale solution of Henry et al. [92] is based on a Darcian description of the momentum conservation with a single temperature energy equation, i.e. Equations 3.12 and 3.13. There is an excellent agreement between the pore-scale data for $\kappa = 1$ and the continuum-scale solution
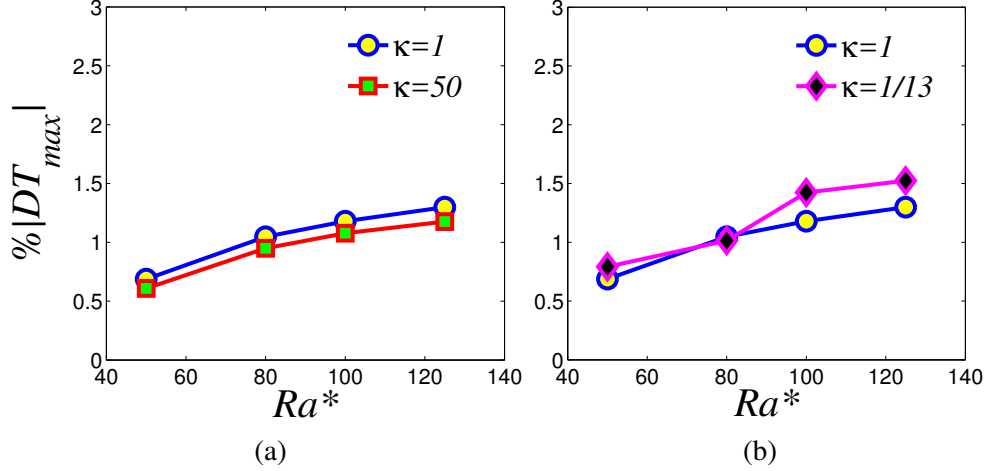
Figure 3.6: Percentage of the maximum amount of thermal disequilibrium ($|DT_{max}|$) in the DNS results for the 20×20 of unit cells; (a): $\kappa = 1$ and 50, (b): $\kappa = 1$ and 1/13.

of Henry et al. [92]. The current pore-scale results for the case of $\kappa = 1$ show that the onset of convection agrees with the theoretical value of $Ra^* = 4\pi^2$ and that the average heat transfer behavior after the onset of convection follows the one predicted by the classical Darcy-LTE formulations. This justifies that the local thermal disequilibrium of $\lesssim 2\%$ observed at the pore-scale is not significant and a single-energy model at the average-scale provides accurate description of the thermal behavior.

The excellent agreement between the pore-scale data and the LTE-Darcy solution in figure 3.7 further confirms that the calculated permeability of the medium by using LBM is accurate and that non-Darcian effects are negligible for the present porous configuration (small Darcy number). The calculated pore-scale Reynolds number is also smaller than 1, further confirming that our simulations satisfy the Darcian regime.

3.4.2 Nu*-Ra* scaling when $\kappa \neq 1$

We now turn our attention on the effect of thermal conductivity contrasts between the solid and fluid on the average heat flux in the domain. Figure 3.8 summarizes the results for the average Nusselt number for $\kappa = 50$ and $\kappa = 1/13$ over a range of Ra around the onset of convection for the case of 20×20 unit cells. Recalling that $\kappa = k_s/k_f$, the data on Fig.
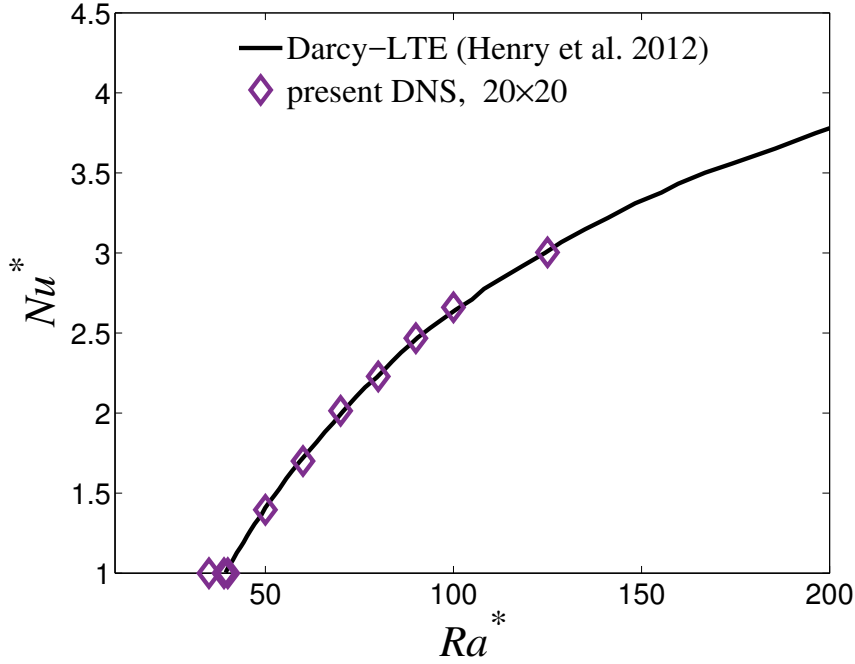
Figure 3.7: Nusselt number Nu^* versus Rayleigh number Ra^* for 20×20 of unit cells, $\kappa = 1$.

3.8 shows that when solid is more conductive than the fluid, for example in $\kappa = 50$, the average Nusselt number falls below the results for $\kappa = 1$, the values predicted by Darcy-LTE solutions. The opposite trend is observed when the fluid is more conductive than the solid, i.e. $\kappa = 1/13$. This discrepancy between LTE $Nu^* - Ra^*$ results and our pore-scale calculations is not caused by local thermal disequilibrium between phases, as the latter is found to be small and comparable to what we observed for simulations with $\kappa = 1$, which matched accurately with the LTE predictions. If we set $\mathcal{H}$ in both LTNE models to a value corresponding to about $2 - 3\%$ of thermal disequilibrium between the fluid and solid phases, we find that both LTNE models are not able to match the observed heat transfer (Nu^*) found in the pore-scale simulations (Figure 3.8).

Comparing the pore-scale data in Figure 3.8 with those from $\kappa = 1$ displayed in Figure 3.7 shows that, not only the $Nu^*(Ra^*)$ scaling for $\kappa \neq 1$ deviates from the LTE solution, but also the onset of convection departs from the classical value of $Ra^* = 4\pi^2$. We define the critical Rayleigh number as the point where a sudden change in the slope of $Nu^* - $

Ra^* curve occurs. When the solid and fluid have similar thermal conductivities, critical point defines the Rayleigh number value above which $Nu^*>1$. However, when the thermal properties of the solid and fluid are different, Nu^* is not necessarily equal to 1 below Ra^*_{cr} because of small-scale fluid motion around each cell can slightly perturb the heat transfer (uncritical convection). For $\kappa = 1/13$, convection initiates well before $4\pi^2$, while it is shifted to slightly higher values than $4\pi^2$ for $\kappa = 50$. Our pore-scale simulations show that the critical Rayleigh number for $\kappa = 1/13$, and 50 are $Ra^*_{cr} \simeq 35$ and 42, respectively.

Although we argued that we do not expect this discrepancy to arise because of a lack of local thermal equilibrium between phases, it is worthwhile to contrast our pore-scale results with LTNE models and test whether any of the two LTNE models presented here can reconcile the spread in $Nu^*(Ra^*)$ and the shift in Ra^*_{cr} observed. According to figure 3.2, explaining the early initiation of convection for $\kappa = 1/13$ ($Ra^*_{cr} \simeq 35$) based on the LTNE-1 model first, would require a significant degree of thermal disequilibrium, and second, would predict that the critical horizontal mode just at the onset of convection is $m = 2$. These two outcomes from the LTNE-1 model disagree with our pore-scale results.

Similar issues arise when trying to explain the pore-scale simulation results with the LTNE-2 model. According to figure 3.3-(a), if we select an $\mathcal{H}$ value which provides a critical Rayleigh number around 35 (similar to pore-scale observations for $\kappa = 1/13$), then the numerical solution of LTNE-2 model predicts a significant local thermal disequilibrium and would also yield Nusselt number values in excess of the LTE ($\kappa = 1$) model. In summary, neither LTNE-1 and LTNE-2 models can explain the shift in the onset of convection and the $Nu^*(Ra^*)$ dependence self-consistently.

In the absence of consistent description of the pore-scale results with LTE and LTNE models, the discussions in the next section try to provide an interpretation in terms of a new thermal dispersion phenomena in HRL convection which arises from the contrast in thermal conductivity between different phases.
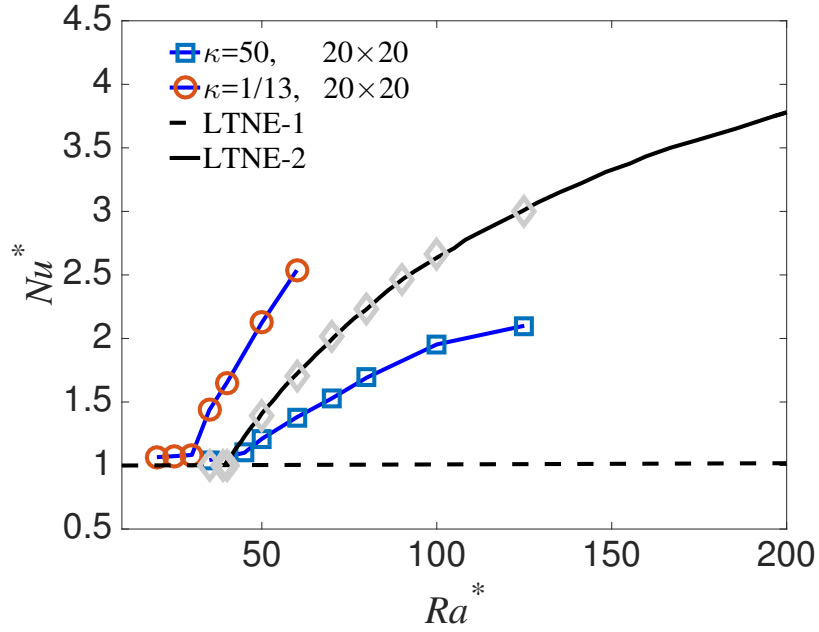
Figure 3.8: Nusselt number Nu^* versus Rayleigh number Ra^* for 20×20 unit cells, $\kappa = 50$ and 1/13; For comparison, the results for the LTE and LTNE models and $\kappa = 1$ are shown respectively in gray symbols and black lines.

3.5   Discussions and Conclusions

3.5.1   Effect of coarseness

When convection initiates, boundary layers build up at the top and bottom boundaries. As the Rayleigh number increase, these boundary layers shrink in size, resulting in larger temperature gradients and heat flux next to the top and bottom boundaries. Using the continuum-scale equations for modeling HRL convection is valid as long as the pore size of the medium is smaller than any length-scale of the flow; specially thermal boundary-layer thickness in HRL convection [93]. Therefore, it is crucial to verify whether the coarseness of the domain in our pore-scale simulation allows us to retrieve averages solution in the continuum limit and resolves the boundary layers accurately.

Figure 3.9 illustrates the horizontally averaged temperatures in the pore-scale temperature fields of various coarseness using arrays with 10×10, 15×15 and 20×20 of solid blocks (Figure 3.1). We observe that as the Rayleigh number increases, the boundary layer

becomes more localized, thus resulting in higher Nusselt numbers. It also shows that us-
ing a coarser number of solid blocks in 10×10 and 15×15 cases results in a similar
horizontally-averaged temperature profiles to 20×20 case. Therefore, different number
of solid blocks offer a similar average thermal behavior which is further illustrated in the
$Nu^*(Ra^*)$ curves of Figure 3.10.

The data in Figures 3.9 and 3.10 shows that, the observed shift in the onset of convection
and the $Nu^*(Ra^*)$ scalings for different κ and Ra^* values are robust over the range of
coarseness studied here, which suggest that the resolution and coarseness used are suitable
to compare DNS results with continuum model predictions. Figure 3.11 shows that, for
$\kappa = 1$ and $Ra^* = 100$ in the 20×20 case, the thickness of the boundary layer is at
least four times larger than the size of the unit cell, which is the true averaging volume for
the regular configuration of solid blocks in the pore-scale domain. For Rayleigh numbers
larger than the values studied here, however, finer configurations of solid blocks would be
required.

3.5.2 *Thermal dispersion*

The deviations between the pore-scale observations and Darcy-LTE predictions can origi-
nate from three factors: LTNE effects, non-Darcian effects and thermal dispersion effects.
In the previous sections, we showed that the first two factors are negligible for the range of
κ and Ra^* numbers investigated in the pore-scale study. In the present section, we try to
investigate the role of thermal dispersion on the observed shift in the onset of convection
and the $Nu^*(Ra^*)$ scalings.

In applying the volume-averaging approach for developing the continuum-scale energy
equation (LTE or LTNE models) from the exact pore-scale energy equations, the thermal
dispersion term $\nabla \cdot (-(\rho c)_f \langle T' u'_f \rangle^f)$ appears, where T' and u'_f are local temperature
and velocity fluctuation fields (for the detailed derivations, reader is refered to [23, 94]
for example). For continuum-scale energy equations such as LTE and LTNE models to
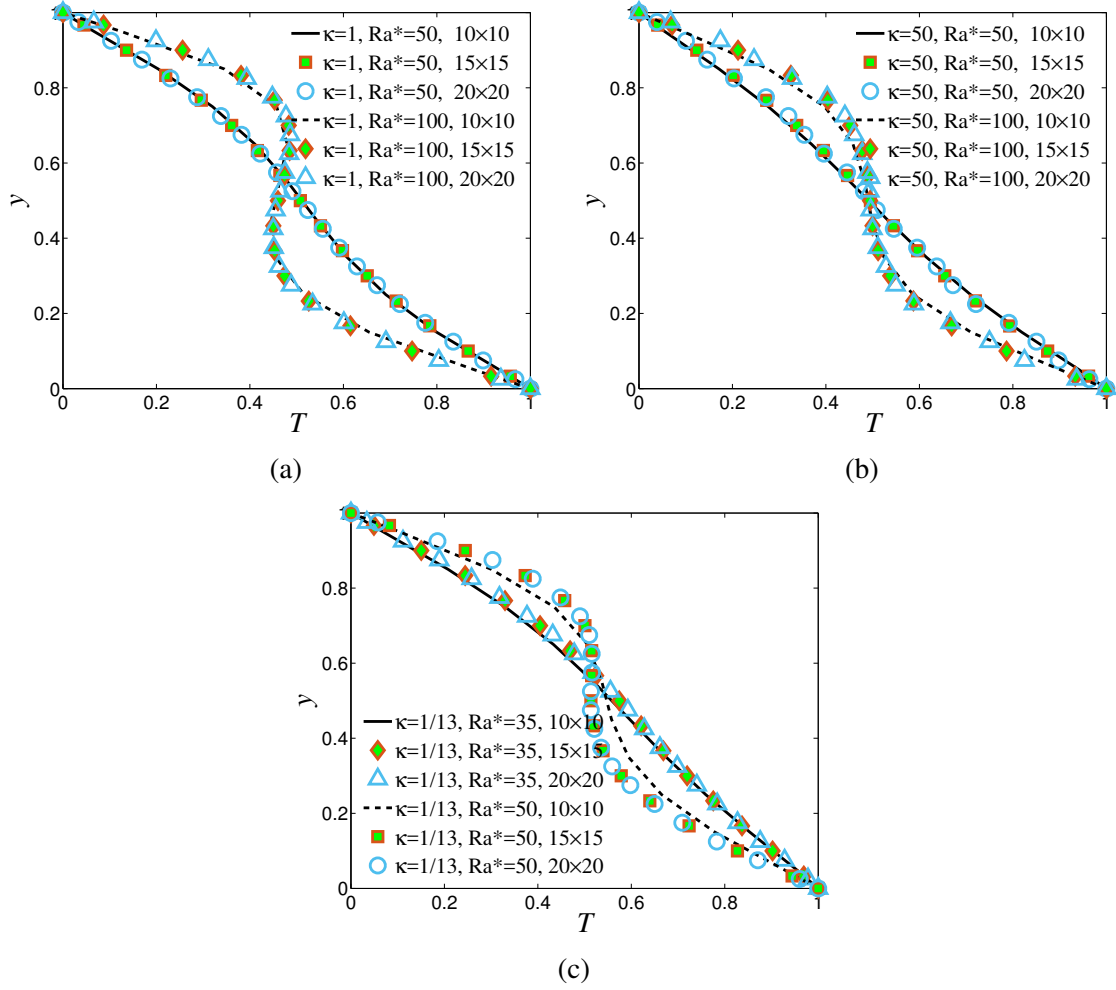
Figure 3.9: Horizontally-averaged temperatures for 20×20 unit cells; (a): $\kappa = 1$, (b): $\kappa = 50$ and (c) $\kappa = 1/13$.
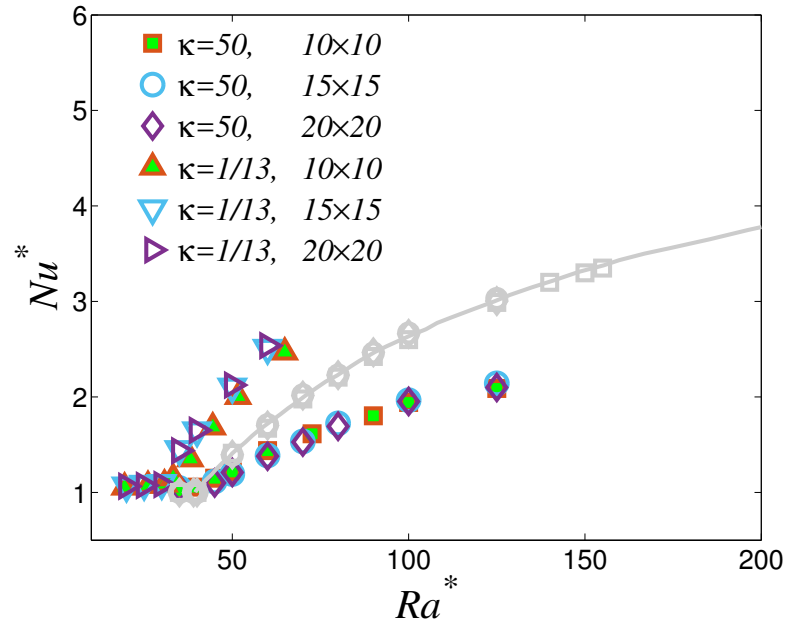
Figure 3.10: Effect of coarseness on *Nu*-Ra** scalings, the results for the LTE model and $\kappa = 1$ are shown in grey.
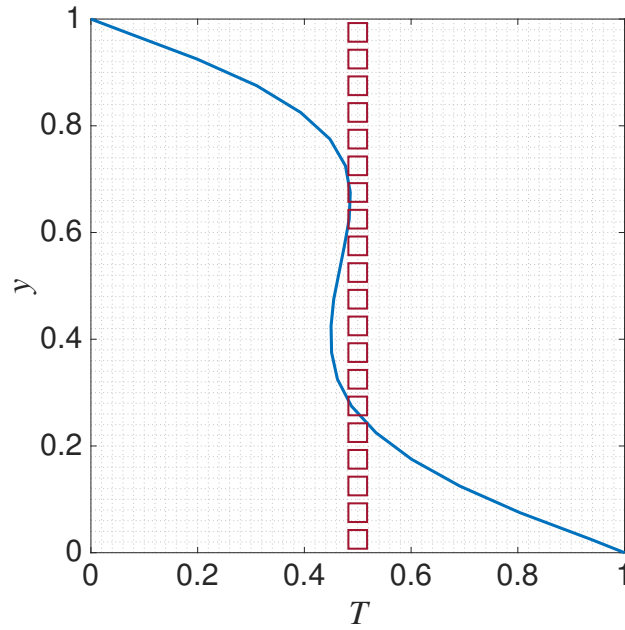
Figure 3.11: Horizontally-averaged temperature field *vs.* the height of the domain; 20×20 unit cells, $\kappa = 1$, $Ra^* = 100$.

be applicable, we need to provide a closure model for the resulting thermal dispersion contribution.

Thermal disperstion is historically modeled as a pseudo-diffusive term [95, 96, 97], i.e. $\nabla \cdot (-(\rho c)_f \langle T' u'_f \rangle^f) = \nabla \cdot (k_{disp} \nabla \langle T_f \rangle^f)$ or equivalently:

$$-(\rho c)_f \langle T' u'_f \rangle^f = k_{disp} \nabla \langle T_f \rangle^f \tag{3.19}$$

where k_{disp} is the dispersion conductivity of the porous medium.

Several studies provided models for k_{disp} in porous media based on the theoretical derivations [95, 96, 97, 98] and numerical simulations over a periodic single unit-cell [99, 100, 101]. The available models for the dispersion conductivity can be represented by the $k_{disp} = C \cdot \mathbf{q}^n$, where *C* is a constant, *n* is some exponent and $\mathbf{q}$ is the local Darcy velocity (or equivalently as $k_{disp} = f(Pe \text{ or } Re)$, where *Pe* and *Re* are the pore-scale Peclet and Reynolds number based on the local average velocity of the fluid).

The inherent pseudo-diffusive assumption for the thermal dispersion term and its dependence on the local average velocity bears important implications in HRL convection. First, thermal dispersion becomes a nonlinear term in the continuum-scale energy models, therefore it cannot influence the onset of convection [102, 30, 103]. Second, previous studies [30, 31] showed that the inclusion of thermal dispersion lowers the heat transport for lower values of Ra^* but increases Nu^* as Ra^* is increased. In summary, the available closure models for k_{disp} cannot explain the shift in the onset of convection and the consistently lower/higher $Nu^*(Ra^*)$ scalings when solid is more/less conductive than the fluid phase.

There are several experimental findings for HRL convection that qualitatively support the present pore-scale results. Cheng [2] and Kladias and Prasad [13] reported that for a porous system with solid matrix being more conductive than the fluid phase, the measured Nusselt numbers are lower than the one predicted by Darcy-LTE and Non-Darcy-LTE mod-

els. Kladias and Prasad [13] further showed that the inclusion of thermal dispersion term does not resolve the issue of a lower heat transfer than the LTE case for larger thermal conductivity ratios. The same authors then propose that local thermal disequilibrium may be the cause for the observed deviations between experimetal data and theoretical predictions. Lister [103] also observed an early initiation of convection at $Ra^* = 33$ in the HRL convection when the fluid is more conductive than the solid phase, although the author manually shifted the experimental data to start the convection at $4\pi^2$.

The present pore-scale study provides significant insights into the nature of thermal disequilibrium and dispersion in HRL convection. The detailed pore-scale temperature fields reveals that, on one hand, deviations from predicted critical Rayleigh number and amount of heat transfer can occur even in the presence of local thermal equilibrium. On the other hand, we posit that a non-traditional thermal dispersion effect is responsible for the discrepancy between pore-scale and continuum models. According to the pore-scale observations, $\nabla \cdot (-(\rho c)_f \langle T' u'_f \rangle^f)$ is directly linked to the contrast in thermal conductivities between the solid and fluid phases, and its contribution disappears when both phases share the same thermal conductivity. Also, the present results prompt a reassessment of the pseudo-diffusive model of thermal dispersion in HRL convection. This latter point relaxes the resulting nonlinear nature of the thermal dispersion which subsequently explains the shift in the onset of convection when solid and fluid phases have different conductivities.

CHAPTER 4

FRACTIONAL-ORDER THERMAL DISPERSION MODEL

In Chapter 3, we conducted direct numerical simulations of HRL convection at the pore-scale and showed that the scatter in predictions of the macroscopic models originate from the thermophysical heterogeneities, resulting in the emergence of a new type of thermal dispersion not previously taken into account. In this chapter, we use this insight from our pore-scale results and propose a new upscaled energy model for HRL convection. We extend the classical model of heat transfer in porous media by including a fractional-order advective-dispersive term to account for the role of thermophysical heterogeneities. The content of this chapter has been submitted for publication in *Physical Review E*, under the title 'Onset of fractional-order thermal convection in porous media'.

4.1 Introduction

The dynamics of transport processes in porous media is usually characterized by early/late arrivals (heavy tails) in the breakthrough curves of the advective species [104] and a nonlinear mean-squared displacement (MSD) for the growth of the spreading entities in diffusive systems [105, 106, 107]. These features of transport behaviors have been observed in natural and engineered heterogeneous systems, including the transport of passive tracers in subsurface media [108, 109], diffusion in gels [110, 111], MRI diffusion processes in biological tissues [112, 113], infiltration of moisture in porous media [114, 115, 116], and Turing pattern formation in reaction-diffusion systems [117, 118, 119]. The heterogeneous and disordered microstructure in these media creates complex transport pathways, such as low mobility zones, dead ends and preferential paths. The upscaling of these localized retardation and enhancement transport zones leads to anomalous transport behaviors that deviate from the classical advection-dispersion regimes.

Heat transfer processes in porous media, such as forced thermal convection and natural thermally-driven flows, can also exhibit anomalous behaviors. In the former, in analogy with solute transport in porous media, Continuous Time Random Walk (CTRW) models [90, 120] and fractional-order energy models [121, 122] have been developed and tested for modeling the experimentally and numerically observed heavy-tailed thermal breakthrough curves due to structural heterogeneities. In the buoyancy-driven thermal convection, also known as Horton-Rogers-Lapwood convection [15, 16] (in short HRL), the anomalous behavior, however, can occur even in a ordered homogeneous and isotropic porous matrix and it manifests itself in shifts for (1) the critical Rayleigh number at the onset of thermal instability, and (2) the average heat transfer represented by the Nusselt-Rayleigh number correlation [2, 13]. In the absence of an inclusive model that can explain these two deviations from the standard solution for HRL convection, we argued in Chapter 3 for the need to revisit the closure of the thermal dispersion term, which arises from upscaling of the velocity and temperature fluctuation fields [94, 23]. Thermal dispersion is historically modeled as a diffusive formulation (originally suggested by Taylor [95] and later extended by Aris [123], Saffman [124, 96], Poreh [97]).

In analogy with the fractional-order advection-dispersion models for anomalous solute transport regimes in porous media [108, 125, 126], one can use a fractional-order thermal advection-dispersion model for describing HRL convection. The main difference is that, in solute transport in porous media, the anomalous dispersion due to the velocity and concentration fluctuations originates from the structural disorder and heterogeneties, while in HRL convection, the thermophysical heterogeneity, i.e. contrast in thermal conductivities of the solid and fluid phases, can also be responsible for the resulting anomalous thermal behaviors. Thermophysical heterogeneities are ubiquitous in almost every multi-component and multi-phase system, and are responsible for partitioning of energy among the different constituents.

This chapter investigates how a fractional-order energy model influences the onset of

instability in HRL convection. We perform a linear stability analysis and derive an analytical expression for the critical Rayleigh number as a function of the fractional-order parameters that govern the conservation equation. We also solve numerically the original nonlinear coupled equations of motion and fractional heat transfer and verify the robustness of the linear stability results. The linear stability and numerical results show that the fractional-order energy formulation can be successfully and consistently used for modeling the scatter of the onset of instability in HRL convection observed experimentally in Cheng [2], Kladias and Prasad [13] and observed in our direct numerical simulations presented in Chapter 3.

4.2 Mathematical Formulation

We consider a two-dimensional fluid-saturated porous square domain with dimensions $0 < x < d$ and $0 < y < d$, where d is the height/length of the porous enclosure. While the linear stability analysis can be naturally exended to three-dimensions, in order to benefit from the results of an equivalent pore-scale study presented in Chapter 3, we limit our analysis to two dimensions. Assuming a Darcian regime, then the continuity and momentum equations of a Boussinesq fluid in an isotropic porous medium are described, at the continuum scale, by [1]:

$$\frac{\partial u}{\partial x} + \frac{\partial v}{\partial y} = 0, \tag{4.1}$$

$$u = -\frac{K}{\mu}\frac{\partial P}{\partial x}, \tag{4.2}$$

$$v = -\frac{K}{\mu}\frac{\partial P}{\partial y} + \frac{\rho g \beta K}{\mu}(T - T_{ref}), \tag{4.3}$$

where *u* and *v* are Darcy-scale macroscopic velocities in the *x*- and *y*-directions, respectively. *T* and T_{ref} are local average-scale temperature and reference temperatures, respectively. Also, ρ, β, *K* and *g* are the fluid density, thermal expansion coefficient, permeability of the porous medium and and acceleration of gravity; *P* is pressure and μ is the dynamic viscosity of the fluid.

Under the assumption of local thermal equilibrium between the solid and fluid phases, the average-scale energy equation for HRL convection takes the following form:

$$(\rho c)_m \frac{\partial T}{\partial t} + (\rho c)_f \mathbf{V} \cdot \nabla T + (\rho c)_f \nabla \cdot (< \mathbf{V}'T' >^f) = k_m \nabla^2 T, \qquad (4.4)$$

where $\mathbf{V}$ is the velocity vector (u, v), *c* is the specific heat, k_m is the stagnant thermal conductivity of the solid/fluid mixture. The subscripts *m* and *f* refer to the properties of the solid/fluid mixture and the fluid, respectively. The $\nabla \cdot ((\rho c)_f < \mathbf{V}'T' >^f)$ term describes the thermal dispersion term, with the primes indicating the fluctuating fields with respect to the fluid-phase averaged value of the local temperature and velocity fields (for the detailed derivations, the reader is referred to Refs. [23, 94]). Closure models for thermal dispersion often assume a pseudo-diffusive behavior [95, 124, 96, 97], i.e. $\nabla \cdot [(\rho c)_f < \mathbf{V}'T' >^f] = \nabla \cdot (-k_{dis} \nabla T)$. Here, k_{dis} is the dispersive conductivity of the porous media, which is generally a nonlinear function of the pore-scale Péclet or Reynolds number based on the local average velocity of the fluid [95, 124, 96, 97].

In the present study, in analogy with the fractional-order advective-dispersive solute transport equation, we replace Eq. 4.4 with the following energy equation with a fractional-order advective term:

$$(\rho c)_m \frac{\partial T}{\partial t} + (\rho c)_f \hat{C}_{dis} \mathbf{V} \cdot \nabla^\alpha T = k_m \nabla^2 T. \qquad (4.5)$$

$\hat{C}_{dis}$ ($[L^{\alpha-1}]$) is the dispersive coefficient and α is the fractional-derivative index based on the Riemann-Liouville definition [127]:

$$\frac{d^\alpha \Phi}{dz^\alpha} = \frac{d^n}{dz^n} \int_0^z \frac{(z-\xi)^{n-\alpha-1}}{\Gamma(n-\alpha)} \Phi d\xi, \qquad (4.6)$$

where $n-1 < \alpha < n$ and n is the integer and $\Gamma(.)$ is the Gamma function.

The rationale behind using a fractional-order advective-dispersive equation is to relax the *a priori* pseudo-diffusive assumption for the thermal dispersion term. We assume that the contribution of $\nabla \cdot ((\rho c)_f < \mathbf{V}'T' >^f)$ is to enhance or impede the overall average-scale advective thermal flux and is modeled through a fractional-order index α, which can conveniently range from advective to diffusive regimes in a flexible manner. In light of the pore-scale results presented in Chapter 3, we argue that the fractional-order parameters $\hat{C}_{dis}$ and α are functions of the degree of thermophysical heterogeneity, i.e. solid-to-fluid thermal conductivity ratio k_s/k_f, where k_s and k_f are thermal conductivities of the solid and fluid phases, respectively. Furthermore, Eq. 4.5 implies that the conductive part is consistently captured through the definition of stagnant thermal conductivity of the medium k_m. This allows Eq. 4.5 to successfully recover the exact conduction solution for Rayleigh numbers below the critical value.

We define the following dimensionless variables in order to recast the governing equations 4.1-4.5 in a dimensionless form:

$$t^* = t\frac{\alpha_m}{H^2 \sigma}, \quad (u,v)^* = (u,v)\frac{H}{\alpha_m},$$
$$(x,y)^* = (x,y)\frac{1}{H}, \qquad (4.7)$$
$$\sigma = \frac{(\rho c)_m}{(\rho c)_f}, \quad \theta = \frac{T - T_{ref}}{T_h - T_c},$$

where $\alpha_m = k_m/(\rho c)$ is the thermal diffusivity of the porous medium based on the stagnant

thermal conductivity k_m. Also, H is the characteristic height of the porous enclosure.

We use the stream function ψ and normalize lengths, velocity, time and temperature based on the dimensionless variables in Eq. 4.7 to retrieve the following dimensionless momentum and energy equations (dropping asterisk for simplicity):

$$\frac{\partial^2 \psi}{\partial x^2} + \frac{\partial^2 \psi}{\partial y^2} = Ra \frac{\partial \theta}{\partial x}, \tag{4.8}$$

$$\frac{\partial \theta}{\partial t} + C_{dis}\left(u\frac{\partial^\alpha \theta}{\partial x^\alpha} + v\frac{\partial^\alpha \theta}{\partial y^\alpha}\right) = \frac{\partial^2 \theta}{\partial x^2} + \frac{\partial^2 \theta}{\partial y^2}, \tag{4.9}$$

where

$$C_{dis} = \hat{C}_{dis}\frac{H^2}{H^{1+\alpha}}$$

$$\mathbf{V} = (u, v) = \left(-\frac{\partial \psi}{\partial y}, \frac{\partial \psi}{\partial x}\right), \tag{4.10}$$

and the Rayleigh number (Ra) is defined as:

$$Ra = \frac{\rho g \beta \Delta T K H}{\mu \alpha_m}. \tag{4.11}$$

Without losing generality, we perform the linear stability analysis of the fractional-order HRL convection for a square box. Figure 4.1 shows the schematic of the problem. The hydrodynamic and thermal boundary conditions are as follows:

$$(u, v) = 0, \quad \theta = 1, \quad \text{for} \quad y = 0, \quad \text{for all} \quad x, \tag{4.12}$$

$$(u, v) = 0, \quad \theta = 0, \quad \text{for} \quad y = 1, \quad \text{for all} \quad x, \tag{4.13}$$

73
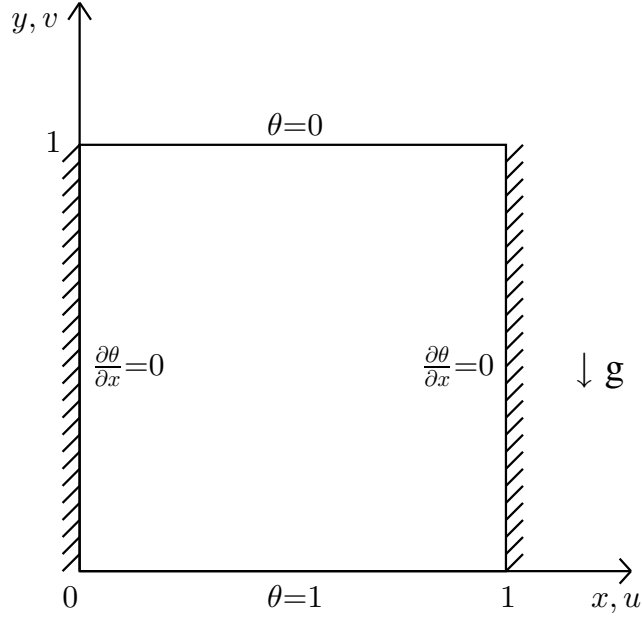
Figure 4.1: Schematic showing a saturated porous square enclosure and the choice of thermal boundary conditions. No-slip velocity i.e. $(u, v=0)$ is applied at all the walls.

$$(u, v) = 0, \quad \frac{\partial \theta}{\partial x} = 0, \quad \text{for} \quad x = 0, 1, \quad \text{for all} \quad y. \tag{4.14}$$

In addition to the linear stability analysis, we solve the dimensionless coupled nonlinear Eqs. 4.8 and 4.9 numerically to verify the linear stability analysis. For this purpose, we use the numerical approach based on a fast Fourier transform detailed in Chapter 5. For ψ, we use a central finite difference scheme on space derivatives and treat the source term in Eq. 4.8 explicitly. The same procedure is used for the temperature field by treating the advective terms in Eq. 4.9 explicitly and the diffusion term implicitly. There are several ways to discretize the fractional-order advective terms in Eq. 4.9. We employ the Grünwald-Letnikov discretized representation of the Riemann-Liouville operators in Eq. 4.9 [127]:

$$\frac{d^\alpha \Phi}{dx^\alpha} \approx \Delta x^{-\alpha} \sum_{l=0}^{N} \omega_l \Phi(x - l\Delta x), \tag{4.15}$$

where Δx is the spatial grid size, and the coefficients ω_l are calculated through the following formula [127]:

$$\omega_l = \frac{(-1)^l \Gamma(\alpha + 1)}{\Gamma(\alpha - l + 1)l!}, \quad l = 0, 1, 2, ..., N. \tag{4.16}$$

Based on the resulting steady-state temperature and velocity fields of the dimensionless equations 4.8 and 4.9 at each Rayleigh number, we calculate the average amount of heat transfer across the porous enclosure through the dimensionless Nusselt number:

$$Nu = \int_0^1 -\frac{\partial T}{\partial y}\bigg|_{wall} dx, \tag{4.17}$$

where the partial derivatives are evaluated at the horizontal bottom boundary of the porous domain.

4.3   linear stability analysis

For Rayleigh numbers below a critical value, only the conduction solution with a linear temperature profile can exist as a stable state in HRL problem (Fig. 4.2-(a)). As the Rayleigh number goes beyond the critical value, convection initiates (Fig. 4.2-(b) illustrates the 1st stable convection mode). Similar to Rayleigh-Bénard convection, HRL convection allows multiplicity of stable states; meaning that several stable convection states with different wave-modes can co-exist [128, 129, 130, 5, 92]. In the present stability study of HRL convection, we are interested in identifying the primary bifurcation point for the onset of convection from the conduction state.
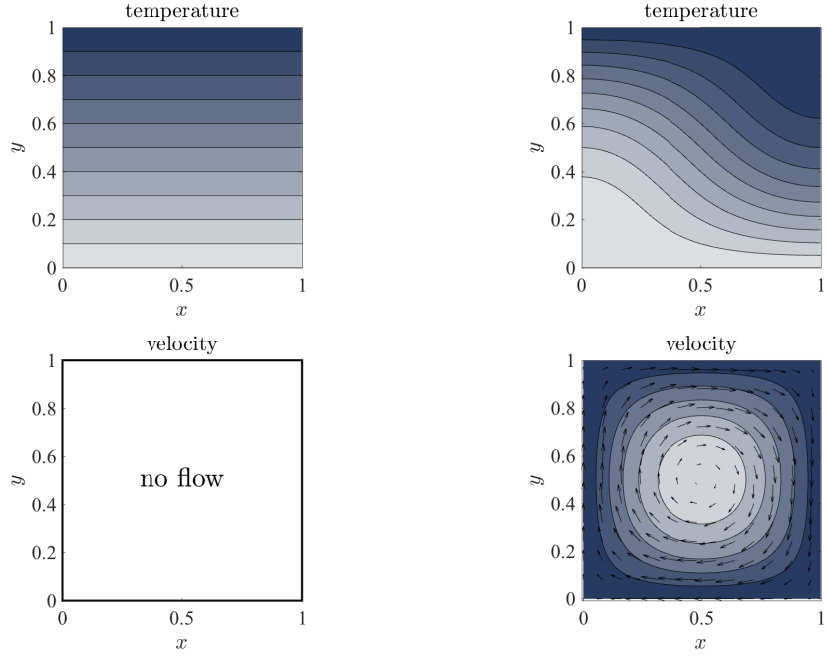
(a) conduction state: $Ra < Ra_{cr}$ (b) convection state: $Ra > Ra_{cr}$

Figure 4.2: Schematic showing the conduction (panel (a)) and convection stable states (panel (b)) for Rayleigh numbers below and above the critical value, respectively.

Linearization

In the absence of convection, Eqs. 4.8 and 4.9 admit the following basic conduction solution:

$$\psi = 0, \quad \theta = 1 - y. \tag{4.18}$$

In order to investigate the onset of convection, we consider the stability of the basic conduction solution with respect to perturbations of the form:

$$\psi = \Psi, \quad \theta = 1 - y + \Theta. \tag{4.19}$$

Inserting these perturbed velocity and temperature fields into Eqs. 4.8-4.9 and linearizing the nonlinear advective terms gives the following set of linearized equations:

$$\frac{\partial^2 \Psi}{\partial x^2} + \frac{\partial^2 \Psi}{\partial y^2} = Ra\frac{\partial \Theta}{\partial x}, \tag{4.20}$$

$$\frac{\partial \Theta}{\partial t} - C_{dis}\frac{\partial \Psi}{\partial y}\frac{\partial^\alpha (1-y)}{\partial x^\alpha} + C_{dis}\frac{\partial \Psi}{\partial x}\frac{\partial^\alpha (1-y)}{\partial y^\alpha}$$
$$= \frac{\partial^2 \Theta}{\partial x^2} + \frac{\partial^2 \Theta}{\partial y^2}. \tag{4.21}$$

Compared with the classical integer-order counterpart, introducing a Riemann-Liouville fractional-order advective term results in an additional linearized advective term in Eq. 4.21. This is due to the fact that the fractional-order derivative of a constant is not zero in the Riemann-Liouville definition [127]; in other words, $\alpha-$ order derivative of a $(1-y)$ with respect to x has nonzero values. More specifically, the analytical relations for the fractional-order derivative terms in Eq. 4.21 are [127]:

$$\frac{\partial^\alpha (1-y)}{\partial x^\alpha} = (1-y)\frac{x^{-\alpha}}{\Gamma(1-\alpha)}, \tag{4.22}$$

$$\frac{\partial^\alpha (1-y)}{\partial y^\alpha} = \frac{y^{-\alpha}}{\Gamma(1-\alpha)} - \frac{y^{-\alpha+1}}{\Gamma(2-\alpha)}. \tag{4.23}$$

Galerkin method

We find the onset of the convective instability by solving for the eigenvalue of the coupled partial differential equations 4.20 and 4.21. Because of the variable coefficients for the advective terms in Eq. 4.21, we select the Galerkin procedure to solve this eigenvalue

problem [131, 132]. We use the following trial functions for the velocity and temperature fields, which automatically satisfy the thermal and hydrodynamic boundary conditions in Eqs. 4.12-4.14:

$$
\begin{aligned}
\Psi &= \sum_{m=1}^{M} \sum_{n=1}^{N} a_{mn} \sin(m\pi x) \sin(n\pi y), \\
\Theta &= \sum_{m=1}^{M} \sum_{n=1}^{N} b_{mn} \cos(m\pi x) \sin(n\pi y).
\end{aligned}
\tag{4.24}
$$

We substitute these trial functions in the linearized perturbation Eqs. 4.20 and 4.21 to find the residuals. We then orthogonalize the residuals (in the spatial domain) with respect to each trial functions, which provides the generalized algebraic eigenvalue problem, where the lowest eigenvalue is the critical Rayleigh number.

We initially limit the analysis to the first order approximation of the Galerkin method, since it conveniently provides a closed form relation for the critical Rayleigh number. The details for the second order approximation are provided in the Appendix. In the results section, we will show that the first term approximation provides accurate values.

Considering only the lowest order values for M and N in Eq. 4.24 ($M = N = 1$), we retrieve:

$$
\begin{aligned}
\Psi &= a_{11} \sin(\pi x) \sin(\pi y), \\
\Theta &= b_{11} \cos(\pi x) \sin(\pi y).
\end{aligned}
\tag{4.25}
$$

Inserting these relations into the linearized perturbed equations and using their orthogonality property (details can be found for example in [132]), we arrive at the following generalized eigenvalue problem:

$$\begin{pmatrix} 2\pi^2 & -Ra\pi \\ C_2\pi & -2C_1\pi^2 \end{pmatrix} \begin{pmatrix} a_{11} \\ b_{11} \end{pmatrix} = \begin{pmatrix} 0 \\ 0 \end{pmatrix}, \tag{4.26}$$

where

$$C_1 = \int_0^1 \int_0^1 (\sin(\pi y)\cos(\pi x))^2 dxdy = 1/4, \tag{4.27}$$

$$C_2 = C_{dis} \left[\frac{1}{\Gamma(1-\alpha)} \int_0^1 \int_0^1 \frac{1-y}{x^\alpha} (\sin(\pi x)\cos(\pi y))(\sin(\pi y)\cos(\pi x))dxdy \right.$$
$$-\frac{1}{\Gamma(1-\alpha)} \int_0^1 \int_0^1 \frac{1}{y^\alpha} (\sin(\pi y)\cos(\pi x))^2 dxdy \tag{4.28}$$
$$\left. +\frac{1}{\Gamma(2-\alpha)} \int_0^1 \int_0^1 \frac{1}{y^{\alpha-1}} (\sin(\pi y)\cos(\pi x))^2 dxdy \right],$$

where C_2 accounts for the influence of the nonlocal advective terms. For each value of the fractional-order derivative α, C_2 can be calculated in a straight-forward way.

The critical Rayleigh number can be determined by setting the determinant of the matrix in Eq. 4.26 to zero, which yields:

$$Ra_{cr} = \frac{C_1 4\pi^2}{C_2}. \tag{4.29}$$

The closed form relation for Ra_{cr} in Eq. 4.29 allows us to measure the effect of the fractional order of the advective operator on the onset of thermal convection and compare it with $4\pi^2$, which is the Ra_{cr} in the classical HRL convection in a square box [15, 16, 133, 92].
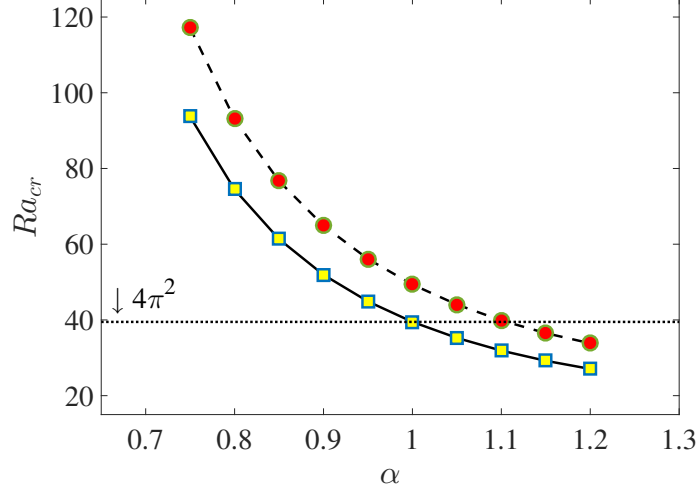
Figure 4.3: Comparison of the predicted Ra_{cr} for different values of α based on single-term (lines) and two-term approximation (symbols) in the Galerkin procedure; (——, □) for C_{dis}=1.0, and (——,○) for C_{dis}=0.8. The horizontal dotted line indicates the classical value of $4\pi^2$ based on integer-order HRL problem.

4.4   Results

In Fig. 4.3, we compare the linear stability results of HRL convection based on single- and two-term approximations in the Galerkin procedure (Eqs. B.2 and B.3). Having a maximum deviation of less than 1% confirms that the formula for the critical Rayleigh number in Eq. 4.29 based on the single-term Galerkin approximation provides accurate results. In all the cases studied here for HRL convection in a square box, the critical convection mode was always observed to be the first mode, i.e. the one shown schematically in Fig. 4.2-(b). Therefore, we focus on the single-term Galerkin solution 4.29 as the linear stability result of the fractional-order HRL problem. We notice in Fig. 4.3 that the fractional-order parameters α and C_{dis} can significantly shift the bifurcation point away from the $4\pi^2$ value of the classical HRL convection in a square box, i.e for the case of $C_{dis} = \alpha = 1$.

This is more clearly illustrated by Fig. 4.4 where we show the map of Ra_{cr} for a range of fractional-order parameters. There is a general trend of increasing Ra_{cr} as we move to lower values of α for a given C_{dis}. A similar trend occurs if α is fixed, and increasing values of C_{dis} result in shifting the critical Rayleigh number to lower values.
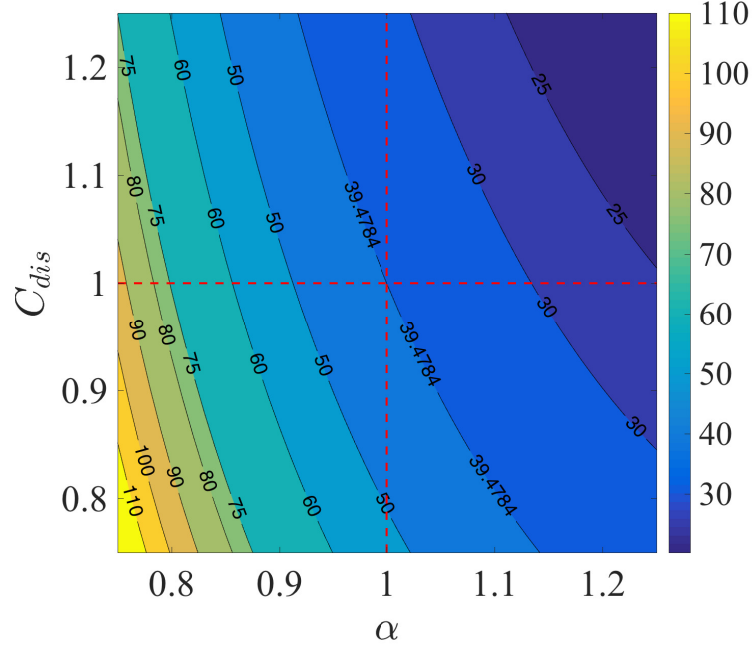
Figure 4.4: map showing the variation of Ra_{cr} for different values of α and C_{dis}

As mentioned previously, experimental studies and pore-scale numerical simulations have reported shifts in the onset of convection (Ra_{cr}) and the heat transfer predicted at a given Ra number. The pore-scale results in Chapter 3 suggest that, for HRL convection in a homogeneous and isotropic porous medium, α and C_{dis} are related to the thermal conductivity difference between the solid and fluid phases. Based on Fig. 4.4, one can get a similar Ra_{cr} at the onset of convection for different combinations of fractional model parameters α and C_{dis}. However, we can provide further insight into the valid ranges of these parameters by solving numerically the coupled nonlinear equations of motion and energy, i.e. Eqs. 4.8 and 4.9 (following the procedure outlined in Section 4.2), and comparing the resulting Nusselt number at each Ra with those from the equivalent pore-scale observations presented in Chapter 3. Figure 4.5 shows the comparison of the critical Rayleigh numbers obtained with linear stability with those retrieved numerically. The maximum relative deviation of less than 3% between the critical Rayleigh numbers from the linear stability analysis and those from the numerical solution confirms once more the accuracy of the first-term Galerkin approximation.
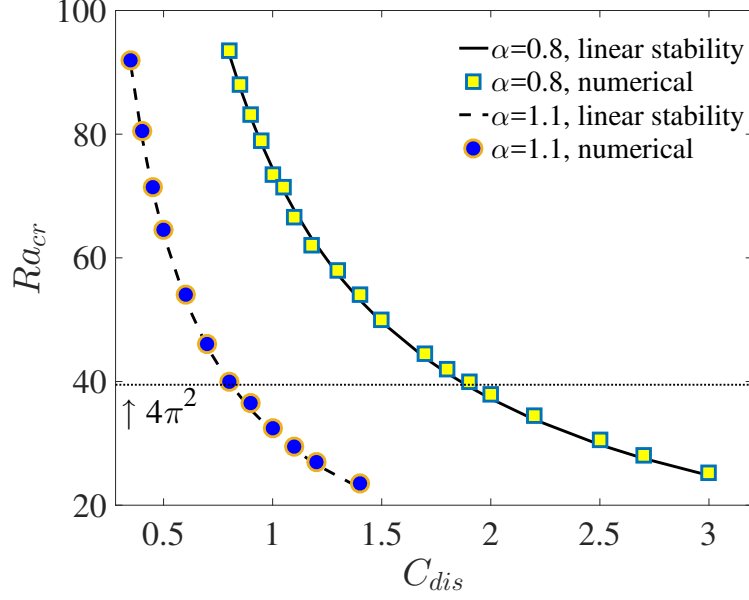
Figure 4.5: Comparison of the predicted Ra_{cr} for different dispersivity C_{dis} based on linear stability analysis (lines) and numerical solution of the nonlinear equations (symbols)

We extend our numerical analysis to Rayleigh numbers greater than Ra_{cr} and observe how the fractional model parameters α and C_{dis} influence the thermal behavior represented by the Nusselt-Rayleigh curve. In Fig. 4.6-(a), we compare the predictions from the fractional model with those from the pore-scale analysis of Chapter 3 for three different values of k_s/k_f. While the pore-scale results for $k_s/k_f = 1$ recover the classical predictions of HRL convection with $\alpha = C_{dis} = 1$, the condition $k_s/k_f > 1$ shifts the onset of convection to higher Rayleigh numbers than $4\pi^2$ and lower Nusselt numbers compared with the classical predictions. In contrast, when $k_s/k_f < 1$ results in earlier initiation of convection, i.e. Ra_{cr} smaller than $4\pi^2$ and higher Nusselt numbers compared to the classical predictions. Figure 4.6-(a) shows these two features for two sample sets of α and C_{dis}, each qualitatively agreeing with the corresponding pore-scale calculations. We observed that among different combinations of fractional model parameters, $\alpha < 1$ and $C_{dis} > 1$ leads to thermal behaviors which satisfy those observed for $k_s/k_f > 1$. On the other hand, when $\alpha > 1$ and $C_{dis} < 1$, the thermal behavior for the onset of convection and Nusselt-Rayleigh curve agrees with those cases where $k_s/k_f < 1$. We can apply these constraints to
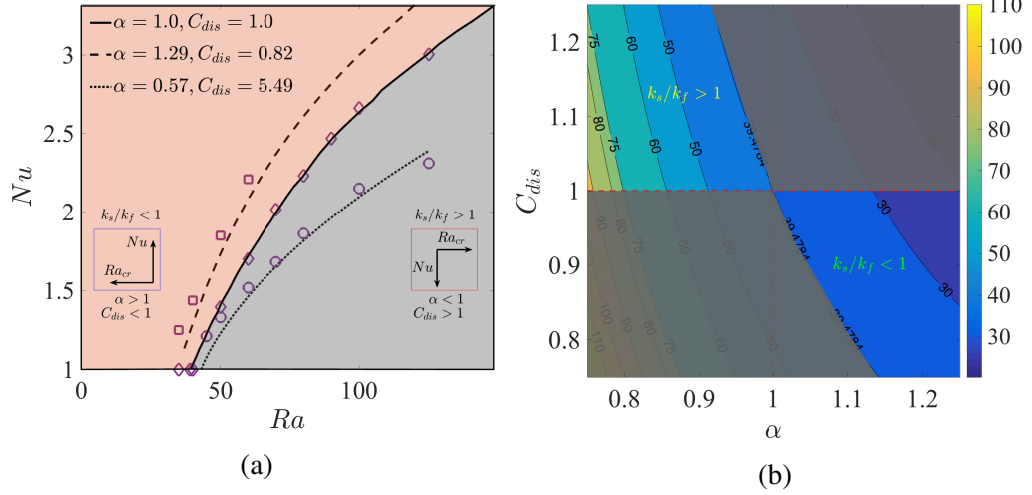
Figure 4.6: Panel (a): the dependency of the observed anomalous behaviors in Ra_{cr} and Nusselt-Rayleigh curves on the solid-to-fluid thermal conductivity ratio k_s/k_f. The solid line in Panel (a) is associated with the predictions based on the classical HRL problem with $C_{dis} = \alpha = 1.0$, agreeing with the pore-scale simulations for $k_s/k_f = 1$ ($\diamond$ symbols). The dashed and dotted curves are the predictions of the fractional-order model qualitatively agreeing with the anomalous behaviors observed in pore-scale results for $k_s/k_f < 1$ ($\square$ symbols) and $k_s/k_f > 1$ ($\circ$ symbols), respectively. Panel (b): valid ranges of C_{dis} and α for satisfying both aspects of anomalous behaviors observed in the pore-scale results for different solid-to-fluid thermal conductivity ratio k_s/k_f. The gray regions in Panel (b) indicate the values of α and C_{dis} out of the suitable ranges for $k_s/k_f < 1$ and $k_s/k_f > 1$ cases.

identify the suitable ranges of fractional model parameters α and C_{dis} for HRL convection in a homogeneous and isotropic porous medium, which is illustrated in Fig. 4.6-(b).

Based on the present linear stability and the numerical results, we can summarize the variations of α and C_{dis} with the thermal conductivity ratio in the following form:

$$\alpha \propto (k_s/k_f)^{-1},$$
$$C_{dis} \propto (k_s/k_f), \tag{4.30}$$

For $k_s/k_f = 1$, we will have $\alpha = C_{dis} = k_s/k_f = 1$ when solid and fluid phases have similar thermal conductivities. In other words, the fractional thermal model recovers the classical solution of HRL convection when the contributions from the thermal dispersion due to the thermophysical heterogeneities disappear in HRL convection.

83

4.5 Discussion

In the classical advection-diffusion formulation of convection in porous media, the thermal dispersion term $\nabla \cdot ((\rho c)_f < \mathbf{V}'T' >^f)$ in Eq. 4.4 appears as the byproduct of the upscaling and homogenization of the advective transport flux. Despite mathematically having an advective form, closure modeling of the thermal dispersion is commonly based on a nonlinear diffusive term. It can be easily shown that the contribution of a pseudo-diffusive thermal dispersion disappears in the linear stability analysis, therefore it cannot influence the onset of convection [102, 30, 103]. Also, the available closure formulations cannot model the consistently lower/higher Nusselt numbers in thermophysically heterogeneous media [30, 31].

The idea behind the fractional-order formulation in Eq. 4.5 is twofold: (1) we do not assume any *a priori* closure nature to the macroscopic behavior of thermal dispersion, i.e neither pure advective nor pure diffusive but rather a fractional-order term that models the intermediate behaviors in a flexible and consistent manner, and (2) we assume that the macroscopic contribution of thermal dispersion in HRL convection, which originates from the upscaling of the advective flux, is to enhance/retard the total advective heat flux due to the thermophysical heterogeneities; a process which cannot be otherwise modeled by the classical advection-diffusion formulation.

The present linear stability and numerical results confirm that including the contribution from the thermal dispersion into a fractional-order advective term not only enables us to model the shift in the onset of convection, but also it successfully provides correct Nusselt-Rayleigh scalings in thermophysically heterogeneous media, in agreement with the pore-scale observations.

While the present linear stability study only accounts for the role of thermophysical heterogeneities on the onset of HRL convection, subsurface systems also include structural and geometrical heterogeneities such as fracture networks. The combined effect of

thermophysical and structural heterogeneities will add complexity to the nature of thermal dispersion in HRL convection. It is therefore important to perform theoretical studies and direct numerical simulations for cases where both permeability and thermophysical properties are varying over space, and to investigate how this coupled spatial variation influences the dynamics of HRL convection.

4.6   Conclusion

This study introduces a fractional-order energy model for studying heat transfer in a density-driven convection in an isotropic and homogeneous porous medium. The fractional-order closure model characterizes the intermediate behaviors between advective and diffusive regimes and accounts for the complex macroscopic realization of transport processes by the thermal dispersion term. We conduct a linear stability analysis to show that the fractional-order generalization of HRL convection is suitable for modeling the shift on the onset of convection due to the thermophysical heterogeneities in a porous medium; a feature that cannot be captured by the classical formulation of the energy equation. The numerical solution of the complete nonlinear governing flow and temperature equations confirm the validity of the critical Rayleigh numbers found through the linear stability study. To the best of our knowledge, the present thermal fractional-order model is the first of its kind that (1) introduces a new formulation for the macroscopic characterization of thermal dispersion in HRL convection and (2) provides consistent predictions for both the critical Rayleigh number and also Nusselt-Rayleigh scalings in a thermophysically heterogeneous porous medium.

CHAPTER 5

TRANSITIONAL BEHAVIOR OF CONVECTIVE PATTERNS

In this chapter, we use a combination of theoretical and experimental approaches to provide a new insight into the cause of the commonly observed kink in the Nusselt-Rayleigh curve in HRL convection. We use a dynamical system theory and show that the observed kink is due to a transitional behavior of stable convective patterns in HRL convection; a dynamical feature of HRL convection which has not been previously taken into account in the classical bifurcation analysis of HRL convection. The material contained in this chapter has been published in the *Journal of Fluid Mechanics*, under the title 'Transitional behaviour of convective patterns in free convection in porous media' [134].

5.1 Introduction

The emergence of flow patterns is omnipresent in nature and is observed in numerous hydrodynamical systems such as thermal convection, convection in binary mixtures, surface waves, rotating fluids and Taylor-Couette flow [4]. The problem of free convection in a fluid-saturated porous medium subjected to an adverse temperature gradient, which is known as HortonRogersLapwood (HRL) convection, is an example of a dynamical system showing multiplicity of flow patterns [129, 135, 128, 130, 5, 136, 92]. HRL convection was first studied by Horton and Rogers [15] and Lapwood [16], who performed linear stability analysis aimed at identifying the critical conditions for the onset of convection in a horizontally infinite porous layer. Beck [133] extended the linear stability analysis of these pioneering studies to confined porous enclosures. Several numerical studies later confirmed the multiplicity of convection solutions [129, 135, 128] at supercritical Rayleigh number values. The results showed that, depending on the initial perturbation, different convection patterns can occur and remain stable at a given Rayleigh number. A significant research

activity has followed to identify these multiple convection solutions in HRL convection [130, 5, 136, 92]. The bifurcation analysis of Riley and Winters [5] is one of the first systematic studies that characterized the different convection modes in a 2D saturated porous cavity using methods developed for dynamical system theory. Recently, Henry et al. [92] extended this work using a continuation technique for tracking the first four stable convection modes from the steady bifurcation point up to the corresponding oscillatory (Hopf) bifurcation point of each mode.

The standard bifurcation analysis of HRL convection using linear stability analysis and continuation techniques, is based on the assumption that the system is subjected to infinitesimal perturbations. These techniques enable the detection of bifurcation points and smoothly track each stable convection mode over a range of Rayleigh number. The main drawback, however, is that they only provide local information about the (range of) existence, and any possible co-existence of different convection modes. It is now well understood that multi-stable dynamical systems exhibit complex interactions, such as transition and switching between the dominant states. Therefore, knowing the local information about their existence only provides a partial understanding of the overall behavior of a multi-stable system [137, 138].

The main idea of this chapter is to apply a new approach for HRL Convection, which not only provides the local information about the (co-)existence of different patterns, but also, determines their relative stability as well as how the basin stability of these modes contract or expands as the Rayleigh number varies. The strategy we are adopting here is first to provide new experimental evidences on the transition from a single-cell to double-cell convection mode in a 2D HRL problem. The transition happens at a Rayleigh number at which both modes can co-exist as stable patterns, according to bifurcation analysis. In order to explain the observed modal transtion, we perform a basin stability analysis [139] on a 2D HRL convection. Menck et al. [139] showed how, in a multi-stable dynamical system, the volume of an attractor's basin, provides a universal measure for quantifying the degree

of stability of a state to random perturbations. Thus, in addition to identifying the range of existence of each mode, the resulting basin stability diagram carries information about how the likelihood of finding each mode varies with the Rayleigh number; a dynamical characteristic of HRL convection that cannot be inferred from bifurcation diagrams.

The chapter is organized as follows: the mathematical formulation of the HRL problem is introduced in section 5.2. Details on the experimental setup and the corresponding experimental results bearing on the transition between modes are presented in Section 5.3. We develop a basin stability analysis for HRL convection in Section 5.4.

5.2 Mathematical formulation

For an isotropic porous medium subjected to a uniform cold temperature T_C from the top boundary and hot temperature T_H from the bottom surface, we choose H, α_m/H, H^2/α_m and $\theta = (T - T_C)/(T_H - T_C)$ as the dimensionless variables for lengths, velocity, time and temperature, respectively, where H is the height of the porous layer, and $\alpha_m = k_m/(\rho c)_f$ is the effective diffusivity of the medium based on the stagnant thermal conductivity k_m and fluid heat capacitance $(\rho c)_f$. The momentum and energy conservation equations take the following dimensionless form in terms of the stream function ψ [1]:

$$\nabla^2 \psi = Ra \cdot \frac{\partial \theta}{\partial x}, \tag{5.1}$$

$$\frac{\partial \theta}{\partial t} + \mathbf{V} \cdot \nabla \theta = \nabla^2 \theta, \tag{5.2}$$

where $\mathbf{V} = (u, v) = (-\partial \psi/\partial y, \partial \psi/\partial x)$ and Ra is the Rayleigh number defined as:

$$Ra = \frac{g\beta(T_H - T_C)KH}{\alpha_m \nu_f}, \tag{5.3}$$

where K is the isotropic permeability of the medium, ν_f is the kinematic viscosity of the fluid, β is the thermal expansion coefficient, g is the gravitational acceleration. The appropriate boundary conditions are constant temperature and zero flux for the horizontal and vertical surfaces, respectively, while a no slip condition is applied at the surface of the solid:

$$\psi = 0, \quad \theta = 1, \quad \text{for} \quad y = 0, \quad \text{for all} \quad x, \tag{5.4}$$

$$\psi = 0, \quad \theta = 0, \quad \text{for} \quad y = 1, \quad \text{for all} \quad x, \tag{5.5}$$

$$\psi = 0, \quad \frac{\partial \theta}{\partial x} = 0, \quad \text{for} \quad x = 0, 1, \quad \text{for all} \quad y. \tag{5.6}$$

In this chapter, we use the average-scale equations 5.1 and 5.2 for the basin stability analysis of HRL convection in a square enclosure. For this purpose, a fast computational algorithm is necessary for performing the Monte-Carlo simulations over a large number of runs subjected to random initial conditions.

We rewrite the temperature equation based on the departure from the conduction state, i.e. $\theta_{new} = \theta - (1 - y)$. This converts the non-homogeneous boundary condition at the bottom surface to a homogeneous one. The dimensionless energy equation then becomes (dropping the subscript for convenience):

$$\frac{\partial \theta}{\partial t} + u \frac{\partial \theta}{\partial x} + v(\frac{\partial \theta}{\partial y} - 1) = \nabla^2 \theta, \tag{5.7}$$

where θ is now the deviation from the conduction state. This change of variable makes the governing equations suitable for using a fast Poisson solver based on discrete Fourier transforms. For the ψ field, we use a central finite difference scheme on space derivatives

and treat the source term in 5.1 explicitly. The same procedure is used for the temperature field by treating the advective terms in 5.7 explicitly and the diffusion term implicitly.

5.3 Experimental study

5.3.1 Experimental design

For the experimental study, we designed a pseudo-two dimensional experimental setup using a non-invasive visualization technique based on the Infrared (IR) thermography. A schematic of the setup is shown in Figure 5.1. We perform the visualization of the temperature field with a FLIR long-range IR (LWIR) thermal camera within a spectral range of 7.5 and 13 μm. The experimental domain consists of a 10×10 array of acrylic rods and it is filled with 20 cSt silicone oil. The thermal conductivity of the silicone oil and acrylic are 0.142 and 0.19 (W/m.K), respectively. The porosity is 0.5 and the size of the cell is $45 \times 45 \times 10 \ mm^3$. The domain is heated from below with power resistors and cooled from the top with a thermoelectric module. Using copper plates with very high thermal conductivity compared to acrylic and silicon oil at the bottom and top boundaries allows us to assume a constant temperature boundary condition, which was tested continuously with a set of K-type thermocouples attached to both copper plates. Additionally, a PID-based temperature controller is used to control the temperature on the two horizontal plates.

The choice of 10×10 array is based on a detailed pore-scale numerical simulations over a 2-dimensional domain (presented in Chapter 3) similar to the one shown in Figure 5.1. The pore-scale simulations show that, the average thermal behavior of a 10×10 pore-scale domain is analogous to a Darcian homogeneous porous medium and satisfies the local thermal equilibrium assumption between the solid and fluid phases over the range of Rayleigh number values considered here. Figure 5.2-(a) shows that the average Nusselt number computed from the pore-scale 10×10 simulations, agrees with the average-scale solution for both single and double cell convection modes. Panel (b) in Figure 5.2 also shows that, increasing the resolution from 10×10 to 20×20 does not affect the simulated

temperature profiles over the domain. We used the same lattice Boltzmann model and calculated the Darcy number of the porous enclosure to be $Da = K/H^2 = 2.435 \times 10^{-5}$.

In the present pseudo-two-dimensional setup, we used thick insulating materials at the side walls of the porous enclosure. The visulatization from the front side requires an IR-transparent window while limiting the amount of heat loss from this side. For this purpose, we use an amorphous material transmitting infrared radiation optic, also commercially known as AMTIR, which has a low thermal conductivity of about 0.25 (W/mK). The window is treated with Anti-Reflective (AR) coatings on both sides. In order to further minimize the heat loss from the front side, two of these AMTIR optics of 2*mm* thickness have been assembled to form a double-pane IR window (Figure 5.1 part (b)). The IR camera reads the temperature field of the outermost layer of the convection cell which is in contact with the IR optic. This comprises both the fluid phase and the solid blocks. The contact between the square blocks with the IR optic was made with a thin (submilimeter) layer of a thermally conductive paste.

Since the ratio of the convection cell depth to its height and width is 4.5 times smaller than the frontal aspect ratio, i.e. 1, we can assume that, for the range of Rayleigh numbers studied experimentally, the effects of the third dimension is relatively negligible. Therefore, we can assume that the flow patterns are mostly 2-dimensional. The heat transfer readings presented in the next section confirm this assumption. The amount of heat transfer characterized by the average Nusselt number is calculated from the net electrical power input:

$$Nu = \frac{[\text{net power input}]}{A \cdot k_m (T_H - T_C)/H},$$
(5.8)

where *A* is the surface area of the bottom hot surface.

(a) sketch of the cell

(b) side view
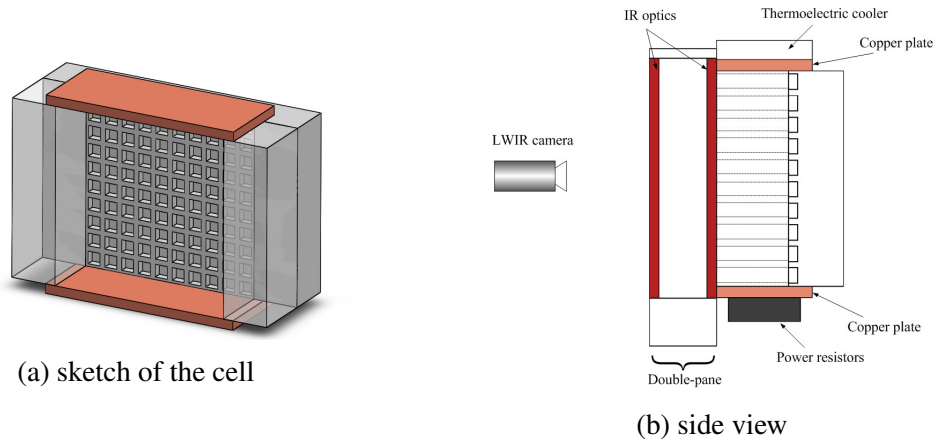
Figure 5.1: schematic of the experimental convection cell (not to scale); part (a) shows only the fluid-filled area without the solid square rods for clarity.

(a)

(b)
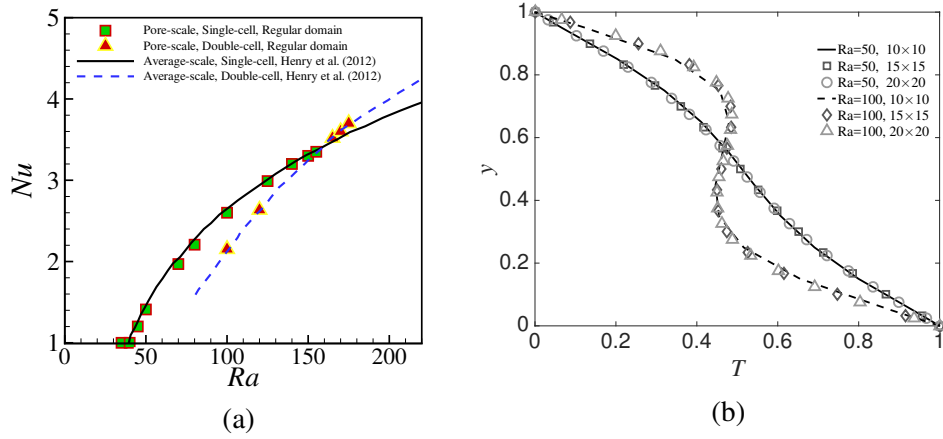
Figure 5.2: (a) comparison of heat transfer data between pore-scale simulations of 10×10 solid blocks and average-scale solution of Henry et al. [92] for single- and double-cell patterns, (b) horizontally-averaged temperatures of the pore-scale simulations for 10×10, 15×15 and 20×20 solid blocks.

5.3.2 Experimental results

We conduct a series of experiments where we ramp up *Ra* by sequentially increasing the temperature difference between the hot and cold plates and letting the system relax to reach a steady-state at each step. At steady state, we record the average heat flux (*Nu*) and flow patterns for each experiment. In other words, for each convection case, the initial conditions are always the steady flow reached at the previous Rayleigh number. Figure 5.3 illustrates the observed steady patterns for several Rayleigh numbers shown as black and white fringes. At *Ra*=32, which is under the critical value of $4\pi^2$, Figure 5.3-(a) shows that heat conduction prevails, i.e. the isotherms are horizontal. The curvature in the lower left part of the isotherms in Figure 5.3-(a) is due to a very small gap between the lower left square acrylic rod and the IR optic, resulting in the imperfect horizontal isotherms in that region. The maximum Rayleigh number explored is *Ra*=221, higher values have been avoided due to the high bottom boundary temperature.

Taking a closer look at the steady-state patterns in Figure 5.3 reveals that the stable mode is a single-cell pattern with a counter clockwise rotation for *Ra*=46-108. Then the stable mode switches naturally from single-cell at *Ra*=108 to double-cell at *Ra*=119 which remains the dominant mode for the rest of the Rayleigh numbers explored. The same behavior has been observed when the Rayleigh number has been decreased from *Ra*=221 to *Ra*=46 with the transition point happening exactly at the same point and no signs of hysteresis or triple-cell pattern were found.

In order to identify the point of transition more accurately, we applied a smaller heating step at *Ra*=108 and recovered a single-cell mode at *Ra*=115. Further increase from *Ra*=115 to *Ra*=119 resulted in the transition from single-cell to double-cell convection. Figure 5.4 shows the snapshots of the reorganization of the convection cells from single- to double-cell during the transition from *Ra*=115 to *Ra*=119. The step's magnitude of $\Delta Ra = 4$ was the minimum that could be reached in the current experimental setup and any effort to recover the single-cell mode beyond *Ra*=115 led to the transition to double-cell pattern.

We complemented this series of experiments with a different heating scenario. The goal of this new set of experiments is to verify whether the point of transition is sensitive to the magnitude of the applied thermal loading ΔRa. Figure 5.5 presents the summary of the results for both large and small heating size ΔRa and reveals that, using a large ΔRa and starting off from the steady state pattern at *Ra*=52, leads to a single-cell convection mode at *Ra*=108 and 115. The transition to double-cell mode occurs again at *Ra*=119, similar to the case with small ΔRa (see Figure 5.5(b)). The only observed difference in the transition under small and large thermal loading ΔRa is that, the former happens in a significantly shorter time compared to the latter; i.e. about 3 hours compared to about 9 hours, respectively.

Figure 5.6 shows the comparison between the correlation of heat transfer data *Nu* and the thermal forcing *Ra* in the experiments with those from the numerical solution offered by Henry et al. [92] for HRL convection in a 2-D square container. The *Ra* at which the change in modality of convection is experimentally observed to occur is marked by an arrow. A good agreement is observed between the data points and the average-scale solution of Henry et al. [92]. The main discrepancy occurs at higher *Ra* values where the increase in the heat loss from the front-side of the setup with the double-pane window becomes significant.

At the experimentally found transition point, the bifurcation analysis of HRL convection tells us that both single and double-cell patterns can co-exist [92]. However, natural transition from single-cell to double-cell mode under different heating scenarios shows that, although both modes are stable, they possess different extent of stability in the face of random perturbations which is responsible for hopping from one stable pattern to another. Therefore, the multiplicity of HRL convection calls for a new metric which characterizes the *relative stability* of different stable patterns. The basin stability analysis of HRL convection provides the details of this characteristic in the next section.

(a) *Ra*=32 (b) *Ra*=46 (c) *Ra*=52 (d) *Ra*=68

(e) *Ra*=88 (f) *Ra*=98 (g) *Ra*=108 (h) *Ra*=119

(i) *Ra*=132 (j) *Ra*=144 (k) *Ra*=156 (l) *Ra*=168

(m) *Ra*=182 (n) *Ra*=190 (o) *Ra*=206 (p) *Ra*=221
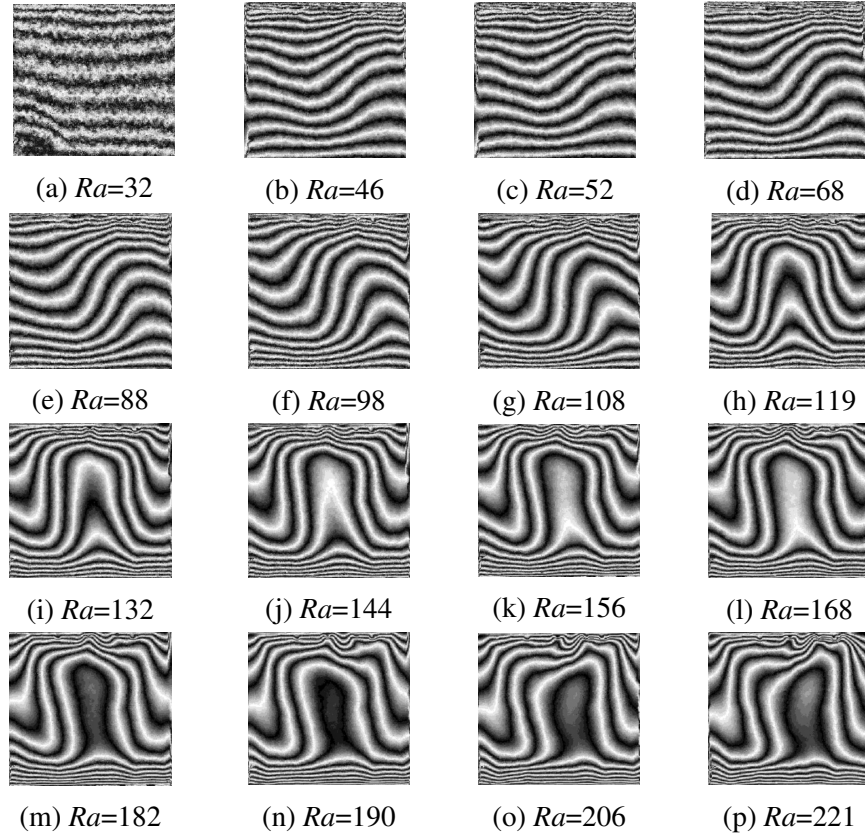
Figure 5.3: steady-state patterns at different *Ra*.
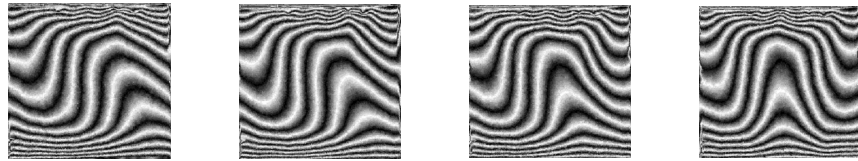
Figure 5.4: Experimental snapshots (IR images) of transition from single-cell mode at $Ra = 115$ (leftmost pattern) to double-cell mode at $Ra = 119$ (rightmost pattern).
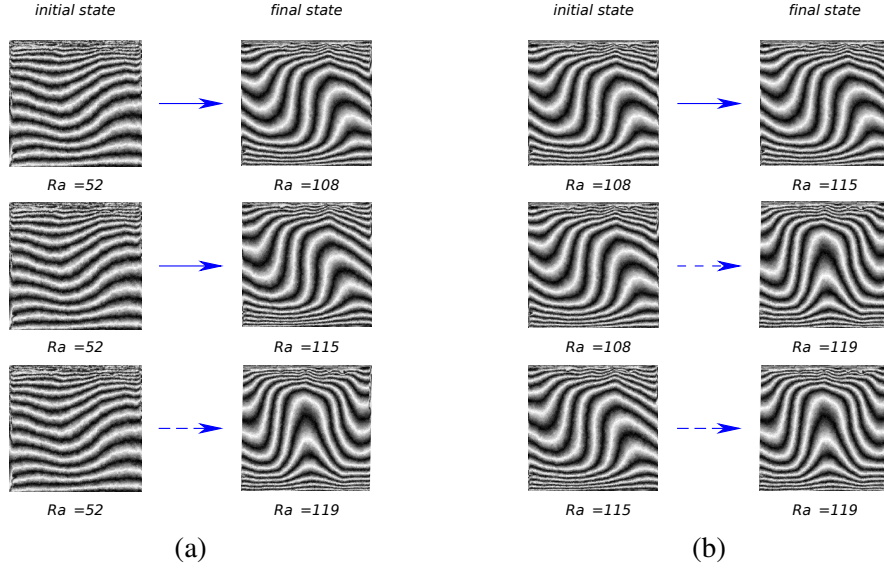
Figure 5.5: summary of transitional behavior from single-cell to double-cell in our experiments; (a): large ΔRa, (b) small ΔRa.
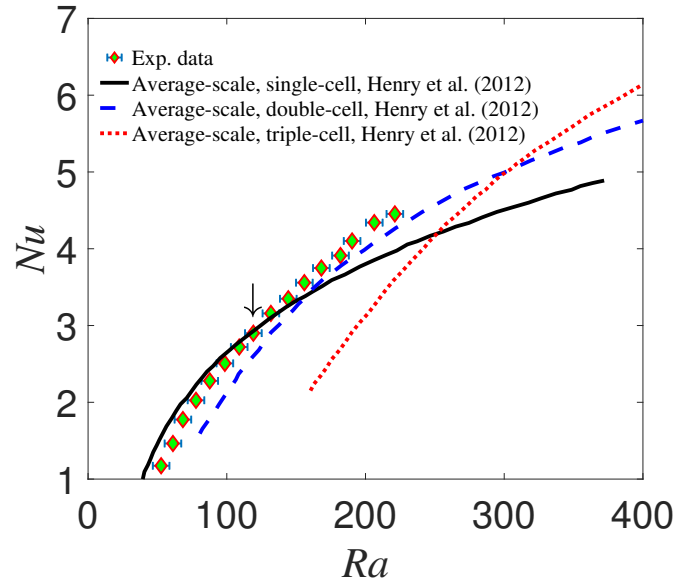
Figure 5.6: *Nu* measured experimentally for single- and double-cell modes; lines: average scale solution based on Darcy-single temperature models of [92], symbols: experimental data; The arrow shows the transition point between single-cell to double-cell pattern observed experimentally.

5.4 Basin stability analysis of HRL convection

We use a basin stability analysis [139] for finding the relative stability of different convective modes when the system is subjected to random perturbations. Basin stability analysis links the volume of the basin of attraction in a multi-stable system to the likelihood of finding the system under a certain steady-state [139].

The detailed continuum-scale bifurcation analysis of Henry et al. [92] shows that the first four modes in HRL convection are stable below Ra=382.93. In this section, we extend the results of Henry et al. [92] by not only providing the information about the range of existence, but also showing how the basin of attraction of each mode varies with the Rayleigh number, and how this results in different probabilities of occurence.

To perform the basin stability analysis for HRL convection, it is necessary to calculate the basin of attraction for each stable convective mode. A basin of attraction is the set of all the points in the phase space, chosen as random initial conditions, which return the system to a specific attractor. In realistic porous media, the factors influencing the final asymptotic stable convective modes may originate from different sources, such as imperfect boundaries, uncertainties in thermo-physical properties, uncertainties in the initial conditions and uncontrolled noises from the environment. In the present study, we focus on the contribution of random initial conditions on the selection of stable modes. As pointed out in Venturi et al. [140], the complete formulation of initial perturbations in real physical systems involves the incorporation of an infinite number of wave-modes, which makes the problem computationally prohibitive. Here, since Equation 5.1 is a boundary value problem and that fluid inertia is negligible, we assume that the initial perturbation applies only to the conduction solution of the temperature field and involves only a finite number n of wave-modes, in the following form:

$$\theta_{pert}(x, y, t = 0) = \sum_{k=1}^{n} a_k \cos(k\pi x) \sin(\pi y), \tag{5.9}$$

where $a_k \in [-1, 1]$ is a random variable based on a uniform probability distribution. We consider multiple values for the number of wave-modes n to investigate how different modes in the initial perturbation contribute to the asymptotic final stable state within the range of Ra studied here.

The basin stability at a given Rayleigh number is computed using the continuum-scale Equations (5.1) and (5.7) with homogeneous boundary conditions and subjected to random initial perturbations defined as in Equation 5.9. We determine the basin stability (or equivalently the probability of occurrence) of each mode by counting their relative proportion of realizations that led to a given cell pattern under steady conditions.

Figures 5.7-5.9 show the basin of attraction of different convective modes. In these Figures, a_1 to a_4 are the prefactors of the first four wave-modes indicating the relative contribution of each in the initial perturbation field in Equation 5.9. The basins of attraction at Ra=100 shown in Figure 5.7 clearly illustrate that, although single- and double-cell modes coexist at this Rayleigh number, the first convective mode possesses a larger basin of attraction. However, Figure 5.8 shows how the basin of attraction of the first mode shrinks considerably in size, as the Rayleigh number increases from 100 to 150. We observe that for Rayleigh number values 100 and 150, only the first and second convectives modes are stable, which is consistent with the bifurcation analysis of Henry et al. [92]. Also, the basin of attractions in Figures 5.7 and 5.8 show a strong dependency of the stable convection mode on the prefactors a_1 and a_2, and a weak dependency on a_3 and a_4. This behavior, however, changes for $Ra = 250$, where the triple cell mode emerges, as shown in Figure 5.9, and a_3 impacts the mode selection process.

Figures 5.7-5.9 illustrate that the coexistence of the single-, double-, and triple-cell

modes is accompanied by a large difference in the size of the corresponding basin of attraction, and that the relative size of the basins of attraction is a strong function of the Rayleigh number. We compare the relative size (volume) of the basins of attraction of each mode to the total size of the basin, which provides a measure for the likelihood of finding a convective mode at a certain Rayleigh number [139].

Figure 5.10(a) shows the probability of formation of the first and second convection modes based on the number of wave-modes $n=2$ and 4 in Equation 5.9. There is only a slight difference between considering $n=2$ and 4 in the initial perturbation. In order to show the role of higher-order wave-modes, the probability of each mode is shown in Figure 5.10(b) for a wide range of Rayleigh numbers. The figure shows that increasing the number of wave-modes from $n=4$ to 10 has an insignificant effect on the probability trends. In other words, higher order wave-modes have smaller contribution on the steady-state stable convection mode over this range of Rayleigh numbers. The overall number of realizations conducted at each Rayleigh number is chosen so as to provide statistically robust results (at least 50000 realizations, see Figure 5.11).

The steady bifurcation points for the first four stable convective modes in the basin stability diagram of Figure 5.10(b) agree well with the bifurcation analysis (Table 3 in Henry et al. [92]). However, according to the basin stability diagram of Figure 5.10(b), the domains of co-existence of multiple modes are strongly influenced by their respective basin stability. For example, the probability of finding the first convection mode drops suddenly as the double-cell mode emerges and in fact, it falls below 10% for $Ra \gtrsim 200$. At the same time, the formation of double convection becomes more likely and at $Ra \sim 112$, it overtakes the single-cell mode and remains stochastically the most probable mode for a wide range of Rayleigh number starting from $Ra \simeq 120$. Regarding the triple-cell mode, we observe from Figure 5.10(b) that, the probability of finding the triple-cell mode is less than 10% for $Ra \lesssim 210$, beyond which, it increases considerably up to $Ra \simeq 315$. On the other hand, Figure 5.10(b) informs us that the probability of occurence of the four-cell
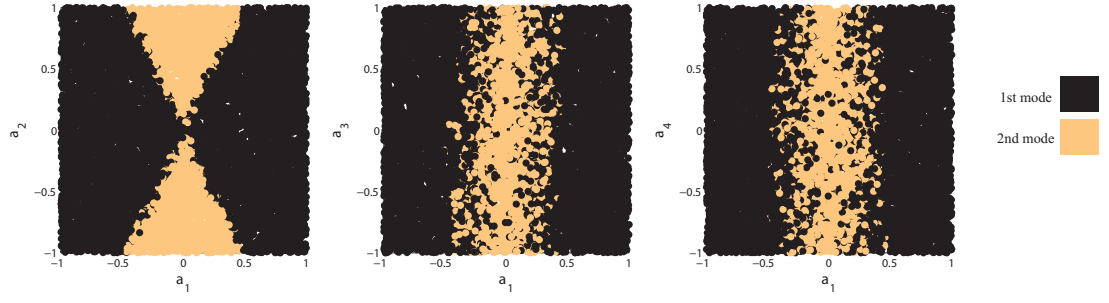
Figure 5.7: Basins of attraction for 1st and 2nd convective modes based on superposition of 4-modes in initial perturbation, $Ra = 100$.
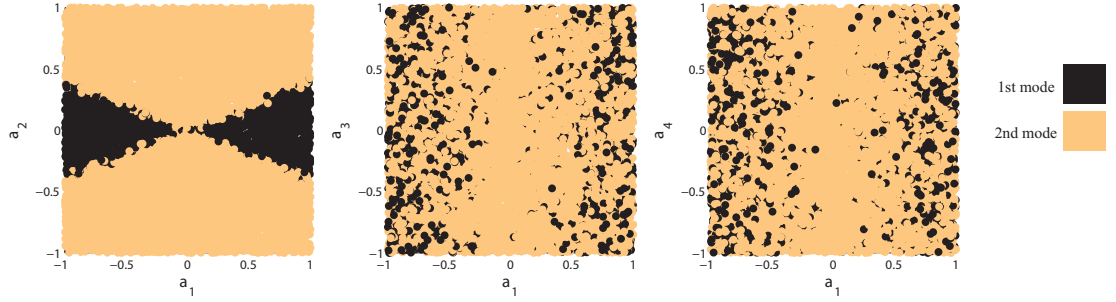
Figure 5.8: Basins of attraction for 1st and 2nd convective modes based on superposition of 4-modes in the initial perturbation, $Ra = 150$.

mode remains below 1% from it's steady bifurcation point at $Ra \simeq 263.7$ (consistent with the bifurcation analysis of Henry et al. [92]) up to the maximum Rayleigh number studied here. Therefore, the present bifurcation diagram clearly shows that the sole knowledge of the range of (co)-existence of different modes in the multi-stable HRL convection only provides a partial understanding about the complex dynamics of the system.

The star symbols in Figure 5.10(b) show the Rayleigh number where we experimentally observed the transition from single-cell mode to double-cell pattern. The transition point inferred experimentally agrees well with the point where the double-cell mode becomes stochastically preferred over the single-cell mode. For Rayleigh numbers beyond the transition point, we observed experimentally that the double-cell pattern remains the dominant mode, which is consistent with the basin stability diagram.
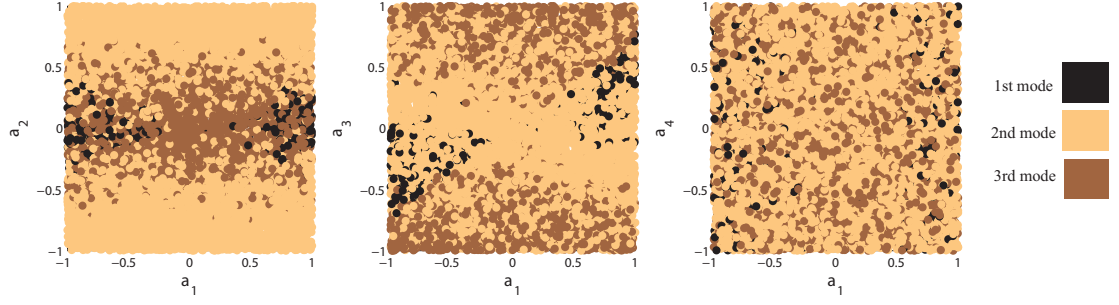
Figure 5.9: Basins of attraction for 1st, 2nd and 3rd convective modes based on superposition of 4-modes in the initial perturbation, $Ra = 250$.

(a)   (b)
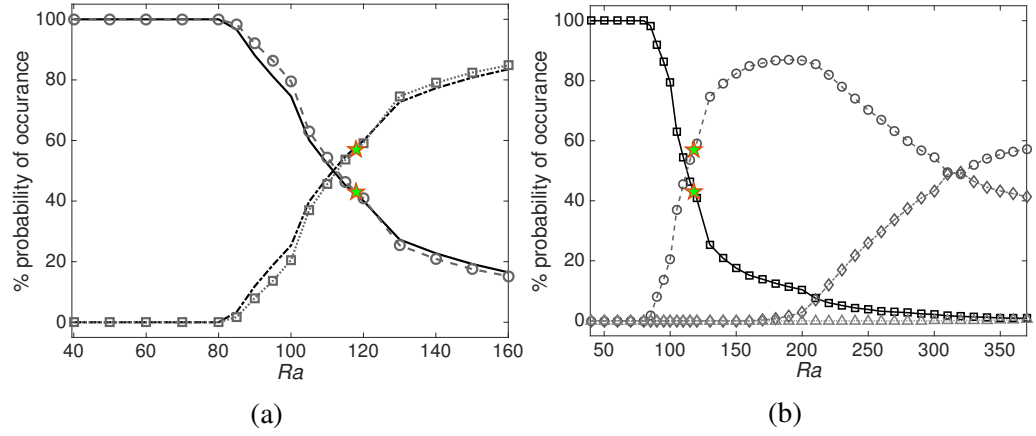
Figure 5.10: Basin stability diagrams: (a): effect of the first 2 wave-modes (lines) and 4 wave-modes (line-symbols) on the probability of formation; 1st mode: (—, $- \circ -$), 2nd mode: ($\cdot -$,$\cdots \square$), (b) effect of the first 4 wave-modes (lines) and 10 wave-modes (symbols) on the probability of formation; 1st mode: (—,$\square$), 2nd mode: ($- -$,$\circ$), 3rd mode: ($\cdot -$,$\diamond$), 4th mode: ($\cdots$,$\triangle$); The stars show the experimentally observed transition point from single-cell to double-cell pattern.

(a) Ra=100   (b) Ra=150   (c) Ra=250
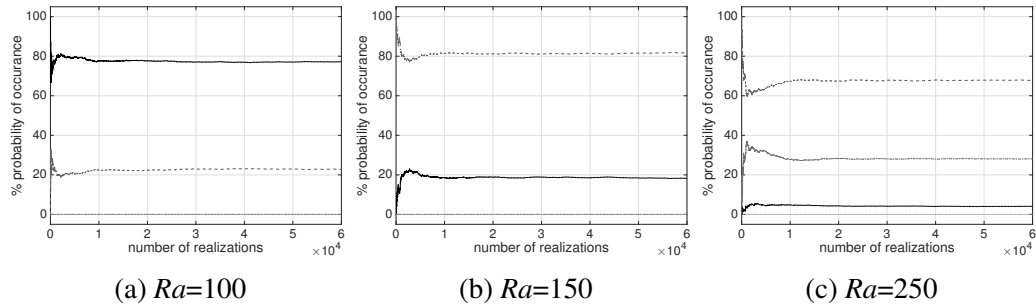
Figure 5.11: Variation of probability of occurrence with the number of realizations; 1st mode: (—), 2nd mode: ($- -$), 3rd mode: ($\cdot -$), 4th mode: ($\cdots$).

101

5.5 Summary

The present study investigates the basin stability analysis of Horton-Rogers-Lapwood convection in porous media. The resulting basin stability diagram provides information on the relative stability of different steady convection modes. The results show that, although different modes co-exist over a given range of Rayleigh number, their probability of occurrence varies with Rayleigh number as the relative size of their basin of attraction grows or decreases. Experiments confirm that the transition from single to double cell convection patterns occurs when the size of the respective stability basins crossover. The numerical study of Schubert and Straus [129] confirmed that the prefered convective pattern does not necessarily maximize the heat transfer. The present study further suggests that, under random perturbations/noise, the most likely patterns to emerge are the ones that have the greater basin at that Rayleigh number. Figure 5.12 compares the transtion points from the present basin stability analysis and experimental observations with the patterns that would maximize the heat transfer (refer to Figure caption for details). This comparison confirms that, while the transition point predicted by the basin stability analysis agrees well with the one observed experimentally, the transition point based on the maximization of heat transfer occurs at a higher Rayleigh number.
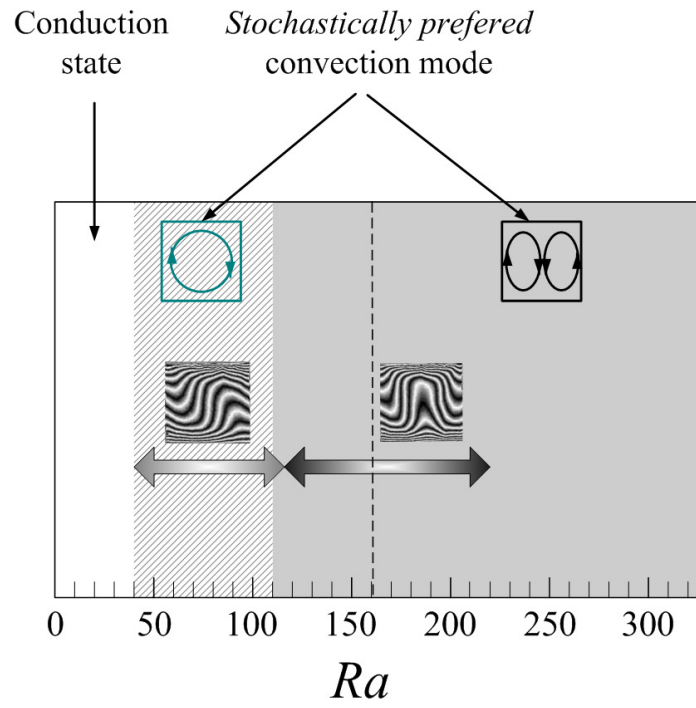
Figure 5.12: Transition points from single-cell to double cell mode; horizontal arrows showing the experimentally observed patterns; colored regions indicate the stochastically prefered patterns; the vertical dashed line shows the transition point based on the maximization of heat transfer.

CHAPTER 6

CONCLUSIONS AND OUTLOOK

6.1 Conclusions

In the present thesis, several issues relevant to buoyancy-driven thermal convection in porous media were addressed. We developed theoretical, numerical and experimental methods to study the Horton-Rogers-Lapwood convection. In contrast to previous studies, our approach was based on a pore-scale perspective. We establieshed a multi-scale framework, which benefits from the insights gained from our pore-scale analysis for developing a consistent upscaled model for HRL convection.

The work contained in Chapters 2 and 3 was concerned primarily with the numerical aspect of our multi-scale framework. In Chapter 2, we developed the computational tool required for our pore-scale analysis. The inherent thermophysically heterogeneous nature of a porous medium required a new computational model, which can handle the interfacial interactions between the solid and fluid phases correctly. For this purpose, we developed a new thermal lattice Boltzmann (LB) model for studying heat transfer in heterogeneous media. In contrast to previously available thermal LB models, our approach was based on retrieving the correct conservative form of the energy equation. This offered a huge computational advantage for pore-scale modeling of HRL convection, since it does not require any specific boundary treatment at the interface of the solid and fluid phases. We validated the reliablity of our LB model with several heat transfer problems under both steady-state and transient conditions.

In Chapter 3, we performed a pore-scale analysis of HRL convection over 2-dimensional porous domains. The goal was to evaluate the underlying assumptions behind the available upscaled thermal models for HRL convection by comparing their predictions with the re-

sults from our pore-scale analysis. For the first time, we quantified the level of thermal disequilibrium between the solid and fluid phases and assessed the role of thermophysical heterogeneties on the thermal behavior of HRL convection. Our pore-scale results revealed that, as opposed to the arguments reported in previous studies, the observed deviations for lower Nusselt values and shift in the onset of convection are not due to the lack of thermal equilibrium between the solid and fluid phases. We showed that these deviations originate from the thermophysical heterogeneities in HRL convection, resulting in the emergence of a new type of thermal dispersion not previously taken into account.

We used this insight from our pore-scale results and proposed a new upscaled energy model for HRL convection in Chapter 4. The proposed model is based on a fractional-order advective term, which models the influence of thermal heterogeneities in a flexible and consistent way. We performed a linear stability analysis and showed that the proposed fractional-order energy model successfully models the shift in the onset of convection caused by the thermophysical heterogeneities. We provided a closed-form analytical formula for the critical Rayleigh number of the fractional-order model and verified the predicted values with numerical solutions of the complete coupled nonlinear governing equations. We further investigated the thermal beahvior of our fractional-order model for Rayleigh numbers beyond the onset of convection. We calculated the corresponding Nusselt number for different values of the model parameters, and showed that the different Nusselt-Rayleigh scalings that we observed in pore-scale calculations can be consistently modeled by the proposed frcational-order model.

In Chapter 5, we used a combination of theoretical and experimental approaches to provide a new insight into the cause of the commonly observed kink in the Nusselt-Rayleigh curve. We calculated a new metric, namely basin stability, for quantifying the respective stability of coexisting convection modes and transition in convection patterns. The transition predicted by the basin stability analysis agrees well with the experiments from our IR thermography visualization setup. For the first time, we provided a *basin stability diagram*

for HRL convection, which not only informs us about the (co)existence of stable patterns, but also provides a quantitative measure about the relative probability of formation of different stable modes in HRL convection.

6.2   Recommendations for Future Directions

In different parts of this research, we have arrived at results that deserve further investigation.

In Chapter 2, the method we propose for treating conjugate boundary conditions with the lattice Boltzmann method is based on a finite-difference approximation. One important future direction would be to extend this approach and propose a thermal lattice Boltzmann model which benefits from recovering the conservative form of the energy equation through the derivation of a new equilibrium distribution function. A great computational advantage would then come from the fully local nature of the resulting lattice Boltzmann model, compared with the present finite-difference based approximation.

In Chapter 3, our pore-scale analysis of HRL convection was focused on the role of thermophysical heterogeneities on the thermal behavior of HRL convection at Rayleigh numbers around the critical value at the onset of convection (with stationary convective modes). Since the present research is one of the first studies to systematically investigate HRL convection from the pore-scale perspective, several important future directions can be defined.

- HRL convection in engineering and natural systems often takes place at higher values of Rayleigh number, mainly in the (non-stationary) periodic and chaotic regimes. How can the thermophysical heterogeneities influence the thermal behavior of HRL convection at those higher Rayleigh values? More specifically, how will the Nusselt-Rayleigh scaling change as we move toward higher Rayleigh values?

- We only considered three thermal conductivity ratios in the present thesis. Perform-

ing a similar pore-scale analysis for several other values of thermal conductivity ratios would provide a more complete set of pore-scale data points, which could be used for verification purposes of any new upscaled models of HRL convection.

- The effect of the microstructure of the unit cell will be a challenging extension of the present study. We only considered a uniform array of solid square blocks. How the geometry of the solid blocks and their arrangements in the domain influence the resulting thermal behavior? How sensitive is the dimensionless Nusselt-Rayleigh scaling on the microstructure of the porous domain?

In Chapter 4, we showed that our proposed fractional-order upscaled energy equation reproduces successfully the results obtained from the pore-scale simulations. We used an inverse approach and found the numerical values of model parameters C_{dis} and α for the three thermal conductivity ratios by using a least squares parameter estimation technique. However, the direct relation between fractional transport parameters and pore scale dynamics remains elusive.

- Can we design a pore-scale strategy for calculating C_{dis} and α for any given unit cell or averaging volume, without resorting to perform curve-fitting over a large number of pore-scale data points?

The novel experimental and theoretical approaches adopted in Chapter 5 offer the following important future directions:

- The pattern visualization experiments were limited to Rayleigh number below $Ra \simeq 220$, where all the stable modes are stationary. Since our basin stability diagram offers interesting features regarding the relative probability of different stable modes at Rayleigh numbers higher than 220, it would be important to investigate how different stable patterns compete in a real experiment. This would require a novel design of the pattern visualization convection cell, with a proper combination of solid and fluid

phases which would work up to higher temperature differences between the hot and cold plate.

- Our basin stability diagram provides only the relative probability between the stable stationary modes. Since in practical applications, periodic (non-stationary) modes emerge at higher Rayleigh numbers, it would be important to extend the basin stability analysis to higher Rayleigh numbers and see how the co-existence of multiple stationary and periodic modes influence the stochastic dynamics of HRL convection under random initial perturbations.

- The basin stability analysis was limited to solid-to-fluid thermal conductivity ratio 1, where the classical formulation of HRL convection applies. A natural question would be: How will the presence of thermophysical heterogeneities influence the relative probability of formation of different stable modes? In other words, what would the basin stability diagram of the proposed fractional-order energy equation look like?

Appendices

APPENDIX A

LINEAR STABILITY ANALYSIS OF LTNE MODELS

In this section, we provide a comprehensive linear stability analysis of LTNE-1 and LTNE-2 models. Banu and Rees [141] were the first to investigate the effect of local thermal disequilibrium on the onset of convection with the LTNE-1 model (Eqs. 3.14 and 3.15). They showed that for finite values of h, the onset of convection deviates significantly from the classical value of $4\pi^2$. As $h \rightarrow \infty$, LTNE recovers LTE and satisfies the classical value $4\pi^2$. However, the definition of the critical Rayleigh number used in their study (Eq. (11) and Figure (3) in Banu and Rees [141]) is based on a volumetric average for the effective thermal conductivity $k_{m,max} = \varphi k_f + (1 - \varphi)k_s$. As discussed earlier, the stagnant thermal conductivity is generally significantly lower than this value. The original derivation of the critical Rayleigh number $4\pi^2$ is based on the true stagnant thermal conductivity of the medium and so is the common *Nu*-Ra** correlation. For these reasons, we decided to conduct the linear stability analysis on model LTNE-2 (Eqs. 3.16 and 3.17), and we will find that LTNE-1 model corresponds to a special case of that more general analysis. In order to have a consistent set of formulations for the stability analysis, we rewrite LTNE-1 and LTNE-2 models in the following general form (assuming that k_{dis} at the onset of convection can be considered uniform):

$$\varphi(\rho c)_f \frac{\partial T_f}{\partial t} + (\rho c)_f \mathbf{q} \cdot \nabla T_f = k_{ff}\nabla^2 T_f + k_{fs}\nabla^2 T_s + h(T_s - T_f) \qquad \text{(A.1)}$$

$$(1 - \varphi)(\rho c)_s \frac{\partial T_s}{\partial t} = k_{ss}\nabla^2 T_s + k_{sf}\nabla^2 T_f - h(T_s - T_f) \qquad \text{(A.2)}$$

For the LTNE-1 model, the thermal conductivities are defined as:

$$k_{ff} = \varphi k_f$$

$$k_{fs} = k_{sf} = 0 \tag{A.3}$$

$$k_{ss} = (1 - \varphi)k_s$$

while for the LTNE-2 model, they are defined as:

$$k_{ff} = \varphi k_f + G k_f + k_{dis}$$

$$k_{fs} = k_{sf} = -G k_s \tag{A.4}$$

$$k_{ss} = (1 - \varphi)k_s + G k_s \kappa$$

We define the following dimensionless variables:

$$t^* = t\frac{\alpha_m}{H^2\varphi}, \quad (u, v)^* = (q_x, q_y)^* \frac{H}{\alpha_m}$$

$$(x, y)^* = (x, y)\frac{1}{H}, \tag{A.5}$$

$$\theta_s = \frac{T_s - T_c}{T_h - T_c}, \quad \theta_f = \frac{T_f - T_c}{T_h - T_c}$$

We can recast equations 3.12, A.1 and A.2 with the stream function ψ and normalize lengths, velocity, time and temperature based on the dimensionless variables in Eq. A.5 to retrieve the following dimensionless governing equations:

$$\nabla^2 \psi = Ra^* \cdot \frac{\partial \theta_f}{\partial x} \tag{A.6}$$

$$\frac{\partial \theta_f}{\partial t} + \mathbf{V} \cdot \nabla \theta_f = \gamma \nabla^2 \theta_f + \sigma \nabla^2 \theta_s + \mathcal{H}(\theta_s - \theta_f) \tag{A.7}$$

$$\frac{\partial \theta_s}{\partial t} = \eta \lambda \nabla^2 \theta_s + \sigma \lambda \nabla^2 \theta_s - \mathcal{H}(\theta_s - \theta_f) \tag{A.8}$$

where

$$\gamma = \frac{k_{ff}}{k_m}, \quad \eta = \frac{k_{ss}}{k_m}, \quad \sigma = \frac{k_{sf}}{k_m} = \frac{k_{fs}}{k_m}$$

$$\mathcal{H} = \frac{Hh^2}{k_m} \quad \lambda = \frac{\varphi}{1 - \varphi} \frac{(\rho c)_f}{(\rho c)_s} \tag{A.9}$$

$$\mathbf{V} = (u, v) = (-\frac{\partial \psi}{\partial y}, \frac{\partial \psi}{\partial x})$$

and *Ra** is defined as:

$$Ra^* = \frac{\rho g \beta \Delta T K H}{\nu_f \alpha_m} \tag{A.10}$$

which is now based on true α_m, as opposed to the modified Rayleigh number based on $k_{m,max} = \varphi k_f + (1 - \varphi)k_s$. We follow the same procedure as Banu and Rees [141] for the linear stability analysis. The basic solution (conductive state) has the following form:

$$\psi = 0, \quad \theta_f = \theta_s = 1 - y \tag{A.11}$$

which is perturbed and becomes:

$$\psi = \Psi, \quad \theta_f = 1 - y + \Theta_f, \quad \theta_s = 1 - y + \Theta_s \tag{A.12}$$

Inserting this expression into Eqs. A.6-A.8 and linearizing the nonlinear advective terms gives the following set of linearized equations:

$$\nabla^2 \Psi = Ra^* \cdot \frac{\partial \Theta_f}{\partial x} \tag{A.13}$$

$$\frac{\partial \Theta_f}{\partial t} = \gamma \nabla^2 \Theta_f + \sigma \nabla^2 \Theta_s - \frac{\partial \Psi}{\partial x} + \mathcal{H}(\Theta_s - \Theta_f) \tag{A.14}$$

$$\frac{\partial \Theta_s}{\partial t} = \eta \lambda \nabla^2 \Theta_s + \sigma \lambda \nabla^2 \Theta_s - \mathcal{H}(\Theta_s - \Theta_f) \tag{A.15}$$

We can assume the following solution form for the velocity and temperature fields:

$$\Psi = A_1 \sin n\pi y \sin m\pi x,$$

$$\Theta_f = A_2 \sin n\pi y \cos m\pi x, \tag{A.16}$$

$$\Theta_s = A_3 \sin n\pi y \cos m\pi x$$

where m and n are the horizontal and vertical cell numbers, respectively. Inserting these expressions in the linearized governing equations yields:

$$\begin{pmatrix} m^2\pi^2 + n^2\pi^2 & Ra^* m\pi & 0 \\ m\pi & \gamma(m^2\pi^2 + n^2\pi^2) + \mathcal{H} & \sigma(m^2\pi^2 + n^2\pi^2) - \mathcal{H} \\ 0 & \sigma\lambda(m^2\pi^2 + n^2\pi^2) - \mathcal{H}\lambda & \eta\lambda(m^2\pi^2 + n^2\pi^2) + \mathcal{H}\lambda \end{pmatrix} \times \begin{pmatrix} A_1 \\ A_2 \\ A_3 \end{pmatrix} = \begin{pmatrix} 0 \\ 0 \\ 0 \end{pmatrix}$$

The critical Rayleigh number Ra^* can then be found by setting the determinant of the matrix to zero:

$$Ra^* = \frac{\pi^2(m^2 + n^2)^2}{m^2} \frac{[(m^2\pi^2 + n^2\pi^2)(\gamma\eta - \sigma^2) + \mathcal{H}(\gamma + \eta + 2\sigma)]}{[\eta(m^2\pi^2 + n^2\pi^2) + \mathcal{H}]} \tag{A.17}$$

Equation A.17 can now be used for analyzing both LTNE models at the onset of convection. By setting $\sigma = 0$, equation A.17 recovers the stability behavior of LTNE-1 model. First, by temporarily setting k_m to be equal to the upper limit value namely $k_{m,max} = \varphi k_f + (1 - \varphi)k_s$, our analysis should recover the results from Banu and Rees [141]. This is shown in Fig. A.1 where we observe that the critical Rayleigh number for the onset of convection is always lower than the classical $4\pi^2$ value for the whole range of normalized inter-phase heat transfer coefficient $\mathcal{H}$. The true stagnant thermal conductivity of
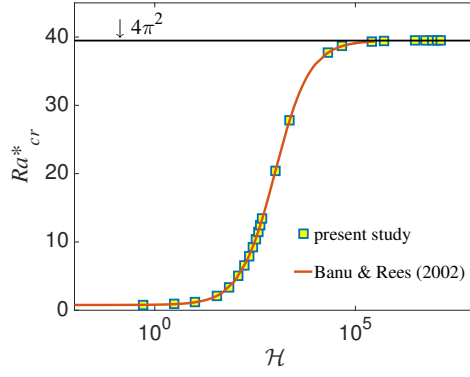
Figure A.1: Recovering the results of Banu and Rees [141] for $k_m = \phi k_f + (1 - \phi)k_s$ in LTNE-1 model

the porous medium takes values lower than this upper limit, whose effect is to raise the critical Rayleigh number at the LTE limit, which has been shown in Fig. 3.2-(a). Comparing Figures A.1 and 3.2-(a) shows the fact that correcting the value of the stagnant thermal conductivity from the upper limit value of $k_{m,max}$ to the correct value k_m significantly changes the value of the critical Rayleigh number.

APPENDIX B

SECOND APPROXIMATION GALERKIN SOLUTION

For the second order approximation, the trial functions take the following form:

$$\Psi = a_{11}\sin(\pi x)\sin(\pi y) + a_{21}\sin(2\pi x)\sin(\pi y) + a_{12}\sin(\pi x)\sin(2\pi y) + a_{22}\sin(2\pi x)\sin(2\pi y),$$

$$\Theta = b_{11}\cos(\pi x)\sin(\pi y) + b_{21}\cos(2\pi x)\sin(\pi y) + b_{12}\cos(\pi x)\sin(2\pi y) + b_{22}\cos(2\pi x)\sin(2\pi y).$$

$$(B.1)$$

We first insert the trial functions B.1 in the linearized perturbed equations 4.20 and 4.21 to develop the residual equations. We then orthogonalize the residual equations to solve the associated 8×8 generalized eigenvalue problem. The first four equations from the velocity equation are as follows:

$$(m^2 + n^2)\pi^2 a_{mn} = m\pi Ra\, b_{mn}, \quad m, n = 1, 2. \tag{B.2}$$

And the resulting four equations from the energy equation become:

$$-b_{k,l}\frac{(k^2 + l^2)\pi^2}{4} + \frac{C_{dis}}{\Gamma(1-\alpha)}\sum_{m=1}^{2}\sum_{n=1}^{2}n\pi a_{mn}\int_0^1\int_0^1 (1-y)x^{-\alpha}(\sin(m\pi x)\cos(n\pi y))(\cos(k\pi x)\sin(l\pi y))dxdy$$

$$-\frac{C_{dis}}{\Gamma(1-\alpha)}a_{kl}\frac{k\pi}{2}\int_0^1 y^{-\alpha}\sin(l\pi y)^2 dy + \frac{C_{dis}}{\Gamma(2-\alpha)}a_{kl}\frac{k\pi}{2}\int_0^1 y^{-\alpha+1}\sin(l\pi y)^2 dy = 0, \quad k, l = 1, 2.$$

$$(B.3)$$

The set of equations in B.2 and B.3 results in an 8×8 generalized eigenvalue problem. We use a global search minimization algorithm which identifies the smallest eigenvalue corresponding to the critical Rayleigh number for any set of parameters C_{dis} and α.

APPENDIX C

NOTATION LIST FOR CHAPTER 3

A cross-sectional area of the porous domain

c specific heat

d square solid block dimension

Da dimensionless Darcy number

$\mathbf{g}$ gravitational acceleration ($9.8\ m^2/s$)

G tortuosity parameter used in calculating k_m

h interface heat transfer coefficient in LTNE models

H height of the porous domain

$\mathcal{H}$ dimensionless interface heat transfer coefficient in LTNE models

k_{disp} dispersive thermal conductivity

k_f thermal conductivity of fluid phase

k_m stagnant thermal conductivity of porous domain

k_s thermal conductivity of solid phase

K permeability of porous domain

m horizontal convective wave-mode in linear stability analysis

n exponent in k_{disp}

$\mathbf{n}$ normal to solid-fluid interface

Nu^* average Nusselt number for porous domain

P pressure

$\mathbf{q}$ seepage velocity (Darcy flux)

Ra^* porous Rayleigh number

Ra_{cr}^* critical porous Rayleigh number

T	temperature
T_f	average fluid temperature
T_C	cold surface temperature
T_H	hot surface temperature
T_s	average solid temperature
$\mathbf{u}$	pore-scale velocity
V	volume of the unit cell
W	width of the porous domain
α	thermal diffusivity
β	thermal expansivity
ρ	density
κ	k_s/k_f
φ	porosity
μ	dynamic viscosity
ν	kinematic viscosity (μ/ρ)
Γ	porous domain aspect ratio (H/W)
ΔT	temperature difference across the porous domain $(T_H - T_C)$
$<.>$	average values over unit cell

APPENDIX D

NOTATION LIST FOR CHAPTER 4

c	specific heat
C_{dis}	dimensionless dispersive coefficient
$\hat{C}_{dis}$	dispersive coefficient
d	size of porous enclosure
$\mathbf{g}$	gravitational acceleration ($9.8\ m^2/s$)
H	characteristic height of the porous enclosure
k_{dis}	dispersive thermal conductivity
k_m	stagnant thermal conductivity of porous domain
K	permeability of porous domain
Nu	average Nusselt number for porous domain
P	pressure
Ra	porous Rayleigh number
Ra_{cr}	critical porous Rayleigh number
T	temperature
T_h	temperature of hot boundary
T_c	temperature of cold boundary
T_{ref}	reference temperature used in Boussinesq approximation
u	Darcy-scale velocity in $x-$direction
v	Darcy-scale velocity in $y-$direction
V	velocity vector (u, v)
α	fractional-derivative order
α_m	thermal diffusivity of porous domain

β thermal expansivity

ρ density

μ dynamic viscosity

ν kinematic viscosity (μ/ρ)

ψ stream function

θ dimensionless temperature

Θ perturbation in temperature field θ

Ψ perturbation in ψ field

Γ Gamma function

ΔT temperature difference between hot and cold boundaries ($T_h - T_c$)

Δx spatial grid size

ω coefficients in Grünwald-Letnikov definition

APPENDIX E

NOTATION LIST FOR CHAPTER 5

A surface area of hot surface

c specific heat

Da Darcy number (K/H^2)

$\mathbf{g}$ gravitational acceleration ($9.8\ m^2/s$)

H characteristic height of the porous enclosure

k_m stagnant thermal conductivity of porous domain

K permeability of porous domain

Nu average Nusselt number for porous domain

P pressure

Ra porous Rayleigh number

Ra_{cr} critical porous Rayleigh number

T temperature

T_H temperature of hot boundary

T_C temperature of cold boundary

T_{ref} reference temperature used in Boussinesq approximation

u Darcy$-$scale velocity in $x-$direction

v Darcy$-$scale velocity in $y-$direction

V velocity vector (u, v)

α_m thermal diffusivity of porous domain

β thermal expansivity

ρ density

μ dynamic viscosity

ν kinematic viscosity (μ/ρ)

ψ stream function

θ dimensionless temperature

ΔT temperature difference between hot and cold boundaries $(T_H - T_C)$

REFERENCES

[1] D. A. Nield and A. Bejan, *Convection in Porous Media*. Springer-Verlag New York, 2013.

[2] P. Cheng, "Heat transfer in geothermal systems," *Advances in Heat Transfer*, vol. 14, pp. 1 –105, 1979.

[3] C. Zhao, B. E. Hobbs, and A. Ord, *Convective and Advective Heat Transfer in Geological Systems*. Springer-Verlag Berlin Heidelberg, 2008.

[4] M. C. Cross and P. C. Hohenberg, "Pattern formation outside of equilibrium," *Rev. Mod. Phys.*, vol. 65, pp. 851–1112, 3 1993.

[5] D. S. Riley and K. H. Winters, "Modal exchange mechanisms in lapwood convection," *Journal of Fluid Mechanics*, vol. 204, pp. 325–358, Jul. 1989.

[6] A. Toth and E. Bobok, *Flow and Heat Transfer in Geothermal Systems: Basic Equations for Describing and Modelling Geothermal Phenomena and Technologies*. Elsevier Oxford, 2017.

[7] D. W. Brown, "A hot dry rock geothermal energy concept utilizing supercritical CO_2 instead of water," in *Proceedings of the twenty-fifth workshop on geothermal reservoir engineering, Stanford University*, 2000, pp. 233–238.

[8] J. B. Randolph and M. O. Saar, "Combining geothermal energy capture with geologic carbon dioxide sequestration," *Geophysical Research Letters*, vol. 38, no. 10, 2011, L10401.

[9] H. Salimi and K.-H. Wolf, "Integration of heat-energy recovery and carbon sequestration," *International Journal of Greenhouse Gas Control*, vol. 6, no. Supplement C, pp. 56 –68, 2012.

[10] R. Xu, L. Zhang, F. Zhang, and P. Jiang, "A review on heat transfer and energy conversion in the enhanced geothermal systems with water/CO_2 as working fluid," *International Journal of Energy Research*, vol. 39, no. 13, pp. 1722–1741, 2015, ER-14-5239.R2.

[11] B. M. Adams, T. H. Kuehn, J. M. Bielicki, J. B. Randolph, and M. O. Saar, "A comparison of electric power output of CO_2 plume geothermal (CPG) and brine geothermal systems for varying reservoir conditions," *Applied Energy*, vol. 140, pp. 365 –377, 2015.

[12] B. M. Adams, T. H. Kuehn, J. M. Bielicki, J. B. Randolph, and M. O. Saar, "On the importance of the thermosiphon effect in CPG (CO_2 plume geothermal) power systems," *Energy*, vol. 69, no. Supplement C, pp. 409 –418, 2014.

[13] N. Kladias and V. Prasad, "Experimental verification of darcy-brinkman-forchheimer flow model for natural convection in porous media," *Journal of Thermophysics and Heat Transfer*, vol. 5, pp. 560–576, Apr. 1991.

[14] L. E. Howle, R. P. Behringer, and J. G. Georgiadis, "Convection and flow in porous media. part 2. visualization by shadowgraph," *Journal of Fluid Mechanics*, vol. 332, pp. 247–262, Feb. 1997.

[15] C. W. Horton and F. T. Rogers, "Convection currents in a porous medium," *Journal of Applied Physics*, vol. 16, no. 6, 1945.

[16] E. R. Lapwood, "Convection of a fluid in a porous medium," *Mathematical Proceedings of the Cambridge Philosophical Society*, vol. 44, pp. 508–521, 04 Oct. 1948.

[17] M. Kaviany, *Principles of Heat Transfer in Porous Media*. Springer New York, 1995.

[18] M. Quintard and S. Whitaker, "Two-phase flow in heterogeneous porous media: the method of large-scale averaging," *Transport in Porous Media*, vol. 3, no. 4, pp. 357–413, 1988.

[19] M. Quintard, M. Kaviany, and S. Whitaker, "Two-medium treatment of heat transfer in porous media: numerical results for effective properties," *Advances in Water Resources*, vol. 20, no. 2, pp. 77 –94, 1997.

[20] J. H. Cushman, L. S. Bennethum, and B. X. Hu, "A primer on upscaling tools for porous media," *Advances in Water Resources*, vol. 25, no. 8, pp. 1043 –1067, 2002.

[21] C. C. Frippiat and A. E. Holeyman, "A comparative review of upscaling methods for solute transport in heterogeneous porous media," *Journal of Hydrology*, vol. 362, no. 1, pp. 150 –176, 2008.

[22] Y. Davit, C. G. Bell, H. M. Byrne, L. A. Chapman, L. S. Kimpton, G. E. Lang, K. H. Leonard, J. M. Oliver, N. C. Pearson, R. J. Shipley, S. L. Waters, J. P. Whiteley, B. D. Wood, and M. Quintard, "Homogenization via formal multiscale asymptotics and volume averaging: how do the two techniques compare?," *Advances in Water Resources*, vol. 62, pp. 178 –206, 2013, A tribute to Stephen Whitaker.

[23] J. Levec and R. G. Carbonell, "Longitudinal and lateral thermal dispersion in packed beds. part i: theory," *AIChE Journal*, vol. 31, no. 4, pp. 581–590, 1985.

[24] M. Quintard and S. Whitaker, "One- and two-equation models for transient diffusion processes in two-phase systems," in, J. P. Hartnett and T. F. Irvine, Eds., vol. 23, ser. Advances in Heat Transfer, Elsevier, 1993, pp. 369 –464.

[25] D. A. S. Rees and I. Pop, "Local thermal non-equilibrium in porous medium convection," in *Transport Phenomena in Porous Media {III}*, D. Ingham, and I. Pop, Eds., Oxford: Pergamon, 2005, pp. 147 –173.

[26] M. Combarnous, "Convection naturelle et convection mixte en milieu poreux," Thèse, Université de Paris, 1970.

[27] D. Close, J. Symons, and R. White, "Convective heat transfer in shallow, gas-filled porous media: experimental investigation," *International Journal of Heat and Mass Transfer*, vol. 28, no. 12, pp. 2371 –2378, 1985.

[28] M. D. Shattuck, R. P. Behringer, G. A. Johnson, and J. G. Georgiadis, "Convection and flow in porous media. part 1. visualization by magnetic resonance imaging," *Journal of Fluid Mechanics*, vol. 332, pp. 215–245, Feb. 1997.

[29] Y. Xie, C. T. Simmons, A. D. Werner, and H.-J. G. Diersch, "Prediction and uncertainty of free convection phenomena in porous media," *Water Resources Research*, vol. 48, no. 2, 2012, W02535.

[30] O. Kvernvold and P. A. Tyvand, "Dispersion effects on thermal convection in porous media," *Journal of Fluid Mechanics*, vol. 99, no. 4, 673686, 1980.

[31] J. G. Georgiadis and I. Catton, "Dispersion in cellular thermal convection in porous layers," *International Journal of Heat and Mass Transfer*, vol. 31, no. 5, pp. 1081 –1091, 1988.

[32] H. Karani and C. Huber, "Lattice Boltzmann formulation for conjugate heat transfer in heterogeneous media," *Phys. Rev. E*, vol. 91, p. 023 304, 2 2015.

[33] "Front matter," in *Transport Phenomena in Multiphase Systems*, A. Faghri and Y. Zhang, Eds., Boston: Academic Press, 2006, pp. iii –, ISBN: 978-0-12-370610-2.

[34] M. Wang and N. Pan, "Predictions of effective physical properties of complex multiphase materials," *Materials Science and Engineering: R: Reports*, vol. 63, no. 1, pp. 1 –30, 2008.

[35] S. Chen and G. D. Doolen, "Lattice Boltzmann method for fluid flows," *Annual Review of Fluid Mechanics*, vol. 30, no. 1, pp. 329–364, 1998.

[36] C. K. Aidun and J. R. Clausen, "Lattice-Boltzmann method for complex flows," *Annual Review of Fluid Mechanics*, vol. 42, no. 1, pp. 439–472, 2010.

[37] C. Huber, W. S. Cassata, and P. R. Renne, "A lattice Boltzmann model for noble gas diffusion in solids: the importance of domain shape and diffusive anisotropy and implications for thermochronometry," *Geochimica et Cosmochimica Acta*, vol. 75, no. 8, pp. 2170 –2186, 2011.

[38] L. Li, C. Chen, R. Mei, and J. F. Klausner, "Conjugate heat and mass transfer in the lattice Boltzmann equation method," *Phys. Rev. E*, vol. 89, p. 043 308, 4 2014.

[39] J. Wang, M. Wang, and Z. Li, "A lattice Boltzmann algorithm for fluid-solid conjugate heat transfer," *International Journal of Thermal Sciences*, vol. 46, no. 3, pp. 228 –234, 2007.

[40] A. Tarokh, A. A. Mohamad, and L. Jiang, "Simulation of conjugate heat transfer using the lattice Boltzmann method," *Numerical Heat Transfer, Part A: Applications*, vol. 63, no. 3, pp. 159–178, 2013.

[41] X. Chen and P. Han, "A note on the solution of conjugate heat transfer problems using simple-like algorithms," *International Journal of Heat and Fluid Flow*, vol. 21, no. 4, pp. 463 –467, 2000.

[42] F. Meng, M. Wang, and Z. Li, "Lattice Boltzmann simulations of conjugate heat transfer in high-frequency oscillating flows," *International Journal of Heat and Fluid Flow*, vol. 29, no. 4, pp. 1203 –1210, 2008.

[43] G. Imani, M. Maerefat, K. Hooman, and M. Seddiq, "Lattice Boltzmann method for simulating conjugate heat transfer from an obstacle mounted in a parallel-plate channel with the use of three different heat input methods," *Heat Transfer Research*, vol. 43, no. 6, pp. 545–572, 2012.

[44] M. Seddiq, M. Maerefat, and M. Mirzaei, "Modeling of heat transfer at the fluid-solid interface by lattice Boltzmann method," *International Journal of Thermal Sciences*, vol. 75, pp. 28 –35, 2014.

[45] L. Li, R. Mei, and J. F. Klausner, "Boundary conditions for thermal lattice Boltzmann equation method," *Journal of Computational Physics*, vol. 237, pp. 366 –395, 2013.

[46] P. L. Bhatnagar, E. P. Gross, and M. Krook, "A model for collision processes in gases. i. small amplitude processes in charged and neutral one-component systems," *Phys. Rev.*, vol. 94, pp. 511–525, 3 1954.

[47] C. Huber, A. Parmigiani, B. Chopard, M. Manga, and O. Bachmann, "Lattice Boltzmann model for melting with natural convection," *International Journal of Heat and Fluid Flow*, vol. 29, no. 5, pp. 1469 –1480, 2008.

[48] C. Huber, B. Chopard, and M. Manga, "A lattice Boltzmann model for coupled diffusion," *Journal of Computational Physics*, vol. 229, no. 20, pp. 7956 –7976, 2010.

[49] A. A. Mohamad, *Lattice* Boltzmann Method: Fundamentals and Engineering Applications with Computer Codes. Springer-Verlag London, 2011.

[50] I. Ginzburg, "Lattice Boltzmann modeling with discontinuous collision components: hydrodynamic and advection-diffusion equations," *Journal of Statistical Physics*, vol. 126, no. 1, pp. 157–206, 2007.

[51] Z. Chai and T. S. Zhao, "Lattice Boltzmann model for the convection-diffusion equation," *Phys. Rev. E*, vol. 87, p. 063 309, 6 2013.

[52] S. Chen, J. Tölke, S. Geller, and M. Krafczyk, "Lattice Boltzmann model for incompressible axisymmetric flows," *Phys. Rev. E*, vol. 78, p. 046 703, 4 2008.

[53] S. Chen, J. Tölke, and M. Krafczyk, "Simple lattice Boltzmann subgrid-scale model for convectional flows with high Rayleigh numbers within an enclosed circular annular cavity," *Phys. Rev. E*, vol. 80, p. 026 702, 2 2009.

[54] S. Chen, J. Tölke, and M. Krafczyk, "Simulation of buoyancy-driven flows in a vertical cylinder using a simple lattice Boltzmann model," *Phys. Rev. E*, vol. 79, p. 016 704, 1 2009.

[55] A. A. Mohamad, "Lattice Boltzmann method for heat diffusion in axis-symmetric geometries," *Prog. Comput. Fluid Dyn.*, vol. 9, no. 8, pp. 490 –494, 2009.

[56] W.-S. Jiaung, J.-R. Ho, and C.-P. Kuo, "Lattice Boltzmann method for the heat conduction problem with phase change," *Numerical Heat Transfer, Part B: Fundamentals*, vol. 39, no. 2, pp. 167–187, 2001.

[57] Y. Sun and I. S. Wichman, "On transient heat conduction in a one-dimensional composite slab," *International Journal of Heat and Mass Transfer*, vol. 47, no. 6, pp. 1555 –1559, 2004.

[58] C. L. Y. Yeong and S. Torquato, "Reconstructing random media," *Phys. Rev. E*, vol. 57, pp. 495–506, 1 1998.

[59] Y. Jiao, F. H. Stillinger, and S. Torquato, "Modeling heterogeneous materials via two-point correlation functions: basic principles," *Phys. Rev. E*, vol. 76, p. 031 110, 3 2007.

[60] A. Mohamad and A. Kuzmin, "A critical evaluation of force term in lattice Boltzmann method, natural convection problem," *International Journal of Heat and Mass Transfer*, vol. 53, no. 5, pp. 990 –996, 2010.

[61] A. A. Merrikh and J. L. Lage, "Natural convection in an enclosure with disconnected and conducting solid blocks," *International Journal of Heat and Mass Transfer*, vol. 48, no. 7, pp. 1361 –1372, 2005.

[62] A. Raji, M. Hasnaoui, M. Nami, K. Slimani, and M. Ouazzani, "Effect of the subdivision of an obstacle on the natural convection heat transfer in a square cavity," *Computers & Fluids*, vol. 68, no. Supplement C, pp. 1 –15, 2012.

[63] D. Lagrava, O. Malaspinas, J. Latt, and B. Chopard, "Advances in multi-domain lattice Boltzmann grid refinement," *Journal of Computational Physics*, vol. 231, no. 14, pp. 4808 –4822, 2012.

[64] A. Fakhari and T. Lee, "Finite-difference lattice Boltzmann method with a block-structured adaptive-mesh-refinement technique," *Phys. Rev. E*, vol. 89, p. 033 310, 3 2014.

[65] R. Huang and H. Wu, "Multiblock approach for the passive scalar thermal lattice Boltzmann method," *Phys. Rev. E*, vol. 89, p. 043 303, 4 2014.

[66] O. R. Mohammadipoor, H. Niazmand, and S. A. Mirbozorgi, "Alternative curved-boundary treatment for the lattice Boltzmann method and its application in simulation of flow and potential fields," *Phys. Rev. E*, vol. 89, p. 013 309, 1 2014.

[67] I. Ginzburg, "Equilibrium-type and link-type lattice Boltzmann models for generic advection and anisotropic-dispersion equation," *Advances in Water Resources*, vol. 28, no. 11, pp. 1171 –1195, 2005.

[68] M. Stiebler, J. Tlke, and M. Krafczyk, "Advectiondiffusion lattice Boltzmann scheme for hierarchical grids," *Computers & Mathematics with Applications*, vol. 55, no. 7, pp. 1576 –1584, 2008, Mesoscopic Methods in Engineering and Science.

[69] I. Ginzburg, D. d'Humières, and A. Kuzmin, "Optimal stability of advection-diffusion lattice Boltzmann models with two relaxation times forpositive/negative equilibrium," *Journal of Statistical Physics*, vol. 139, no. 6, pp. 1090–1143, 2010.

[70] H. Karani and C. Huber, "Role of thermal disequilibrium on natural convection in porous media: insights from pore-scale study," *Phys. Rev. E*, vol. 95, p. 033 123, 3 2017.

[71] C. I. Jonsson T, "Prandtl number dependence of natural convection in porous media," *ASME. J. Heat Transfer*, vol. 109, pp. 371–377, Feb. 1987.

[72] F. Kuwahara, M. Shirota, and A. Nakayama, "A numerical study of interfacial convective heat transfer coefficient in two-energy equation model for convection in porous media," *International Journal of Heat and Mass Transfer*, vol. 44, no. 6, pp. 1153 –1159, 2001.

[73] J. G. Fourie and J. P. Du Plessis, "A two-equation model for heat conduction in porous media (ii: application)," *Transport in Porous Media*, vol. 53, no. 2, pp. 163–174, 2003.

[74] Y. H. Qian, D. D'Humires, and P. Lallemand, "Lattice bgk models for navier-stokes equation," *EPL (Europhysics Letters)*, vol. 17, no. 6, p. 479, 1992.

[75] H. Yoshida, T. Kobayashi, H. Hayashi, T. Kinjo, H. Washizu, and K. Fukuzawa, "Boundary condition at a two-phase interface in the lattice Boltzmann method for the convection-diffusion equation," *Phys. Rev. E*, vol. 90, p. 013 303, 1 2014.

[76] R. Huang and H. Wu, "Phase interface effects in the total enthalpy-based lattice Boltzmann model for solidliquid phase change," *Journal of Computational Physics*, vol. 294, pp. 346 –362, 2015.

[77] S. Chen, B. Yang, and C. Zheng, "A lattice Boltzmann model for heat transfer in heterogeneous media," *International Journal of Heat and Mass Transfer*, vol. 102, pp. 637 –644, 2016.

[78] S. Chen, Y. Yan, and W. Gong, "A simple lattice Boltzmann model for conjugate heat transfer research," *International Journal of Heat and Mass Transfer*, vol. 107, pp. 862 –870, 2017.

[79] G. Pareschi, N. Frapolli, S. S. Chikatamarla, and I. V. Karlin, "Conjugate heat transfer with the entropic lattice Boltzmann method," *Phys. Rev. E*, vol. 94, p. 013 305, 1 2016.

[80] Y. Hu, D. Li, S. Shu, and X. Niu, "Full eulerian lattice Boltzmann model for conjugate heat transfer," *Phys. Rev. E*, vol. 92, p. 063 305, 6 2015.

[81] Z. Hu, J. Huang, and W.-A. Yong, "Lattice Boltzmann method for convection-diffusion equations with general interfacial conditions," *Phys. Rev. E*, vol. 93, p. 043 320, 4 2016.

[82] D. Gao, Z. Chen, L. Chen, and D. Zhang, "A modified lattice Boltzmann model for conjugate heat transfer in porous media," *International Journal of Heat and Mass Transfer*, vol. 105, pp. 673 –683, 2017.

[83] T Inamuro, M Yoshino, and F Ogino, "A nonslip boundary condition for lattice Boltzmann simulations," *Physics of Fluids*, vol. 7, no. 12, pp. 2928–2930, 1995.

[84] Q. Zou and X. He, "On pressure and velocity boundary conditions for the lattice Boltzmann bgk model," *Physics of Fluids*, vol. 9, no. 6, 1997.

[85] A. D'Orazio and S. Succi, "Boundary conditions for thermal lattice Boltzmann simulations," in *Computational Science ICCS 2003*, P. M. Sloot, D. Abramson, A. Bogdanov, J. J. Dongarra, A. Y. Zomaya, and Y. E. Gorbachev, Eds., vol. 2657, ser. Lecture Notes in Computer Science, Springer Berlin Heidelberg, 2003, pp. 977–986.

[86] A. D'Orazio, M. Corcione, and G. P. Celata, "Application to natural convection enclosed flows of a lattice Boltzmann {bgk} model coupled with a general purpose thermal boundary condition," *International Journal of Thermal Sciences*, vol. 43, no. 6, pp. 575 –586, 2004.

[87] S. Torquato, *Random Heterogeneous Materials: Microstructure and Macroscopic Properties*, ser. Interdisciplinary Applied Mathematics. Springer New York, 2005, ISBN: 9780387951676.

[88] A. Nakayama, F. Kuwahara, M. Sugiyama, and G. Xu, "A two-energy equation model for conduction and convection in porous media," *International Journal of Heat and Mass Transfer*, vol. 44, no. 22, pp. 4375 –4379, 2001.

[89] C. T. Hsu, "A closure model for transient heat conduction in porous media," *ASME. J. Heat Transfer*, vol. 121, no. 3, 1999.

[90] S. Emmanuel and B. Berkowitz, "Continuous time random walks and heat transfer in porous media," *Transport in Porous Media*, vol. 67, no. 3, pp. 413 –430, 2007.

[91] D. A. S. Rees, A. P. Bassom, and P. G. Siddheshwar, "Local thermal non-equilibrium effects arising from the injection of a hot fluid into a porous medium," *Journal of Fluid Mechanics*, vol. 594, pp. 379–398, Jan. 2008.

[92] D. Henry, R. Touihri, R. Bouhlila, and H. Ben Hadid, "Multiple flow solutions in buoyancy induced convection in a porous square box," *Water Resources Research*, vol. 48, no. 10, n/a–n/a, 2012, W10538.

[93] J. M. Straus, "Large amplitude convection in porous media," *Journal of Fluid Mechanics*, vol. 64, 5163, 1974.

[94] C. Hsu and P. Cheng, "Thermal dispersion in a porous medium," *International Journal of Heat and Mass Transfer*, vol. 33, no. 8, pp. 1587 –1597, 1990.

[95] G. Taylor, "Dispersion of soluble matter in solvent flowing slowly through a tube," *Proceedings of the Royal Society of London A: Mathematical, Physical and Engineering Sciences*, vol. 219, no. 1137, pp. 186–203, 1953.

[96] P. G. Saffman, "Dispersion due to molecular diffusion and macroscopic mixing in flow through a network of capillaries," *Journal of Fluid Mechanics*, vol. 7, no. 2, 194208, 1960.

[97] M. Poreh, "The dispersivity tensor in isotropic and axisymmetric mediums," *Journal of Geophysical Research*, vol. 70, no. 16, pp. 3909–3913, 1965.

[98] J. G. Georgiadis and I. Catton, "Stochastic modeling of unidirectional fluid transport in uniform and random packed beds," *The Physics of Fluids*, vol. 30, no. 4, pp. 1017–1022, 1987.

[99] F. F. Kuwahara, A. A. Nakayama, and H. H. Koyama, "A numerical study of thermal dispersion in porous media," *ASME. J. Heat Transfer*, vol. 118, no. 3, pp. 756–761, 1996.

[100] M. H. Pedras and M. J. de Lemos, "Thermal dispersion in porous media as a function of the solidfluid conductivity ratio," *International Journal of Heat and Mass Transfer*, vol. 51, no. 2122, pp. 5359 –5367, 2008.

[101] N. Jeong and D. H. Choi, "Estimation of the thermal dispersion in a porous medium of complex structures using a lattice Boltzmann method," *International Journal of Heat and Mass Transfer*, vol. 54, no. 1920, pp. 4389 –4399, 2011.

[102] H. Neischloss and G. Dagan, "Convective currents in a porous layer heated from below: the influence of hydrodynamic dispersion," *The Physics of Fluids*, vol. 18, no. 7, pp. 757–761, 1975.

[103] C. R. B. Lister, "An explanation for the multivalued heat transport found experimentally for convection in a porous medium," *Journal of Fluid Mechanics*, vol. 214, 287320, 1990.

[104] Y. Zhang, D. A. Benson, and D. M. Reeves, "Time and space nonlocalities underlying fractional-derivative models: distinction and literature review of field applications," *Advances in Water Resources*, vol. 32, no. 4, pp. 561 –581, 2009.

[105] R. Metzler and J. Klafter, "The random walk's guide to anomalous diffusion: a fractional dynamics approach," *Physics Reports*, vol. 339, no. 1, pp. 1 –77, 2000.

[106] J. Klafter and I. M. Sokolov, "Anomalous diffusion spreads its wings," *Physics World*, vol. 18, no. 8, p. 29, 2005.

[107] R. Klages, G. Radons, and I. M. Sokolov, Eds., *Anomalous Transport: Foundations and Applications*. Weinheim: Wiley-VCH Verlag GmbH & Co. KGaA, 2008.

[108] D. A. Benson, S. W. Wheatcraft, and M. M. Meerschaert, "Application of a fractional advection-dispersion equation," *Water Resources Research*, vol. 36, no. 6, pp. 1403–1412, 2000.

[109] M. Levy and B. Berkowitz, "Measurement and analysis of non-fickian dispersion in heterogeneous porous media," *Journal of Contaminant Hydrology*, vol. 64, no. 3, pp. 203 –226, 2003.

[110] T. Kosztołowicz, K. Dworecki, and S. Mrówczyński, "How to measure subdiffusion parameters," *Phys. Rev. Lett.*, vol. 94, p. 170 602, 17 2005.

[111] T Kosztołowicz, K Dworecki, and S. Mrówczyński, "Measuring subdiffusion parameters," *Phys. Rev. E*, vol. 71, p. 041 105, 4 2005.

[112] R. L. Magin, O. Abdullah, D. Baleanu, and X. J. Zhou, "Anomalous diffusion expressed through fractional order differential operators in the blochtorrey equation," *Journal of Magnetic Resonance*, vol. 190, no. 2, pp. 255 –270, 2008.

[113] R. L. Magin, C. Ingo, L. Colon-Perez, W. Triplett, and T. H. Mareci, "Characterization of anomalous diffusion in porous biological tissues using fractional order derivatives and entropy," *Microporous and Mesoporous Materials*, vol. 178, pp. 39 –43, 2013, Proceedings of the 11th Internatioanl Bologna Conference on Magnetic Resonance in Porous Media (MRPM11).

[114] M. Küntz and P. Lavallée, "Experimental evidence and theoretical analysis of anomalous diffusion during water infiltration in porous building materials," *Journal of Physics D: Applied Physics*, vol. 34, no. 16, p. 2547, 2001.

[115] A. E.-G. E. Abd and J. J. Milczarek, "Neutron radiography study of water absorption in porous building materials: anomalous diffusion analysis," *Journal of Physics D: Applied Physics*, vol. 37, no. 16, p. 2305, 2004.

[116] N. Filipovitch, K. M. Hill, A. Longjas, and V. R. Voller, "Infiltration experiments demonstrate an explicit connection between heterogeneity and anomalous diffusion behavior," *Water Resources Research*, vol. 52, no. 7, pp. 5167–5178, 2016.

[117] B. I. Henry, T. A. M. Langlands, and S. L. Wearne, "Turing pattern formation in fractional activator-inhibitor systems," *Phys. Rev. E*, vol. 72, p. 026 101, 2 2005.

[118] L. Zhang and C. Tian, "Turing pattern dynamics in an activator-inhibitor system with superdiffusion," *Phys. Rev. E*, vol. 90, p. 062 915, 6 2014.

[119] R. Torabi and Z. Rezaei, "Instability in reaction-superdiffusion systems," *Phys. Rev. E*, vol. 94, p. 052 202, 5 2016.

[120] S. Geiger and S. Emmanuel, "Non-fourier thermal transport in fractured geological media," *Water Resources Research*, vol. 46, no. 7, 2010.

[121] Y. Luchko and A. Punzi, "Modeling anomalous heat transport in geothermal reservoirs via fractional diffusion equations," *GEM - International Journal on Geomathematics*, vol. 1, no. 2, pp. 257–276, 2011.

[122] A. Suzuki, S. A. Fomin, V. A. Chugunov, Y. Niibori, and T. Hashida, "Fractional diffusion modeling of heat transfer in porous and fractured media," *International Journal of Heat and Mass Transfer*, vol. 103, pp. 611–618, 2016.

[123] R. Aris, "On the dispersion of a solute in a fluid flowing through a tube," *Proceedings of the Royal Society of London A: Mathematical, Physical and Engineering Sciences*, vol. 235, no. 1200, pp. 67–77, 1956.

[124] P. G. Saffman, "A theory of dispersion in a porous medium," *Journal of Fluid Mechanics*, vol. 6, no. 3, 321349, 1959.

[125] M. M. Meerschaert and A. Sikorskii, *Stochastic Models for Fractional Calculus*. Walter de Gruyter GmbH and Co. KG, 2012, ISBN: 3110258692.

[126] D. A. Benson, M. M. Meerschaert, and J. Revielle, "Fractional calculus in hydrologic modeling: a numerical perspective," *Advances in Water Resources*, vol. 51, pp. 479 –497, 2013.

[127] I. Podlubny, *Fractional Differential Equations*. Academic Press, 1999.

[128] R. N. Horne, "Three-dimensional natural convection in a confined porous medium heated from below," *Journal of Fluid Mechanics*, vol. 92, pp. 751–766, 04 Jun. 1979.

[129] G. Schubert and J. M. Straus, "Three-dimensional and multicellular steady and unsteady convection in fluid-saturated porous media at high Rayleigh numbers," *Journal of Fluid Mechanics*, vol. 94, pp. 25–38, 01 Sep. 1979.

[130] P. H. Steen, "Pattern selection for finite-amplitude convection states in boxes of porous media," *Journal of Fluid Mechanics*, vol. 136, pp. 219–241, Nov. 1983.

[131] B. A. Finlayson, "The galerkin method applied to convective instability problems," *Journal of Fluid Mechanics*, vol. 33, no. 1, 201208, 1968.

[132] "Convective instability problems," in *The Method of Weighted Residuals and Variational Principles*, C. Finlayson, Ed. 1972, ch. 6, pp. 150–207.

[133] J. L. Beck, "Convection in a box of porous material saturated with fluid," *Physics of Fluids*, vol. 15, no. 8, pp. 1377–1383, 1972.

[134] H. Karani and C. Huber, "Transitional behaviour of convective patterns in free convection in porous media," *Journal of Fluid Mechanics*, vol. 818, 2017.

[135] J. M. Straus and G. Schubert, "Three-dimensional convection in a cubic box of fluid-saturated porous material," *Journal of Fluid Mechanics*, vol. 91, pp. 155–165, 01 Mar. 1979.

[136] I. Sezai, "Flow patterns in a fluid-saturated porous cube heated from below," *Journal of Fluid Mechanics*, vol. 523, pp. 393–410, Jan. 2005.

[137] U. Feudel, "Complex dynamics in multistable systems," *International Journal of Bifurcation and Chaos*, vol. 18, no. 06, pp. 1607–1626, 2008.

[138] J. X. Zhou, M. D. S. Aliyu, E. Aurell, and S. Huang, "Quasi-potential landscape in complex multi-stable systems," *Journal of The Royal Society Interface*, 2012.

[139] P. J. Menck, J. Heitzig, N. Marwan, and J. Kurths, "How basin stability complements the linear-stability paradigm," *Nat. Phys.*, vol. 9, pp. 89–92, 2013.

[140] D. Venturi, X. Wan, and G. E. Karniadakis, "Stochastic bifurcation analysis of Rayleigh-Bénard convection," *Journal of Fluid Mechanics*, vol. 650, pp. 391–413, May 2010.

[141] N. Banu and D. Rees, "Onset of Darcy-Bénard convection using a thermal non-equilibrium model," *International Journal of Heat and Mass Transfer*, vol. 45, no. 11, pp. 2221 –2228, 2002.